Development of New Building Blocks for Constructing Novel Polymer Semiconductors for Organic Thin Film Transistors

by

Zhuangqing Yan

A thesis
presented to the University of Waterloo
in fulfillment of the
thesis requirement for the degree of
Master of Applied Science
in
Chemical Engineering

Waterloo, Ontario, Canada, 2013

AUTHOR'S DECLARATION

I hereby declare that I am the sole author of this thesis. This is a true copy of the thesis, including any required final revisions, as accepted by my examiners. I understand that my thesis may be made electronically available to the public.

Abstract

Organic semiconductors are envisioned to have widespread applications in flexible displays, radio-frequency identification (RFID) tags, bio- and chem-sensors, as well as organic solar cells. Polymer semiconductors are particularly suitable for the low-cost manufacture of organic electronics using printing techniques due to their excellent solution processability and mechanical properties. This work focuses on the development of two novel building blocks, IBDF and DTA, which can be used for the construction of high performance organic thin film transistors (OTFTs) and organic photovoltaics (OPVs). Two copolymers, **P6-IBDF-T** and **P5-IBDF-T**, and a homopolymer **P6-IBDF** were prepared using the IBDF building block. Copolymer **P6-IBDF-T** has been prepared via the Stille-coupling polymerization. This polymer exhibits a small band gap of 1.36 eV with HOMO/LUMO energy level of -5.69 eV/-4.43 eV. **P6-IBDF-T** showed stable electron transport performance in encapsulated thin film transistors and ambipolar transport performance in non-encapsulated TFTs. Balanced hole/electron mobilities of up to $8.2 \times 10^{-3}/1.0 \times 10^{-2}$ $cm^2V^{-1}s^{-1}$ was achieved in bottom-contact, bottom-gate organic thin film transistors. In addition, the broad absorption of the polymer over the UV-Vis range suggested that this polymer is suitable for applications in solar cells. The effect of conjugation on mobility and UV-vis spectra of the polymer was studied by comparing **P5-IBDF-T** with **P6-IBDF-T**. The ideal of indirect electron transition was proposed to explain the difference between UV-Vis light absorption spectra for these two polymers.

DTA building block was used to construct four D-A copolymers, namely **PDTA-T**, **PDTA-BT**, **PDAT-BTV**, and **PDTA-TT**. These polymers were characterized by UV-Vis, CV, DSC, TGA, AFM and XRD. Device performance was also investigated on OTFTs. The device performance of DTA based polymer increased as the area of electron donor increase from T in **PDTA-T** to BTV in **PDTA-BTV**. **PDTA-BTV** exhibits hole mobility of 1.3×10^{-3} cm^2 V^{-1} s^{-1} with I_{on}/I_{off} value of $\sim10^{3-4}$ in bottom-contact, bottom-gate organic thin film transistors. All DTA based copolymers exhibited small optical bandgaps (1.18 – 1.27 eV)

and required none or moderate thermal treatment during fabrication process. These make them promising candidates for cost-effective OPV applications.

Acknowledgements

I would like to thank my supervisors, Dr. Yuning Li for giving me the opportunity to work in his groups and his patient guidance and valuable advices through my master's study. Thanks also go to my review committee, Dr. Ting Tsui and Dr. Neil McManus.

Special thanks go to Bin Sun and Chang Guo for testing the OTFT device performance presented in this thesis.

I would also like to thank other members in Li's group, Wei Hong, Shaoyun Chen, Mylene Le Borgne, Leanne Murphy, Amani Alsam, and Yinghui He. Without their help this study would not be successful.

I also thank Jon Hollinger and Prof. Dwight Seferos of University of Toronto for HT-GPC measurements, Dr. Jianfu Ding, Toufic Aridi and Prof. Mario Gauthier for the GPC measurements, and Angstrom Engineering Inc. for providing the thermal deposition system for the fabrication of OTFT devices.

Finally, I would like to thank my family and friends for their constant support.

The work reported herein was financially supported by Natural Sciences and Engineering Research Council (NSERC) of Canada (Discovery Grants).

Table of Contents

List of Figures

List of Schemes

List of Tables

List of Abbreviations, Symbols and Nomenclature

AFM:	Atomic force microscopy
Ag:	Silver
AgCl:	Silver chloride
B3LYP:	Becke 3 term with Lee, Yang, Parr exchange
CV:	Cyclic voltammetry
D-A:	Donor-acceptor
DFT:	Density functional theory
DMSO:	Dimethyl sulfoxide
DPP:	Diketopyrrolopyrrole
DSC:	Differential scanning calorimetry
DTA:	(*E*)-1,2-di(thiazol-2-yl)diazene
DTS:	Dodecyltrichlorosilane
e^-:	Electron
FET:	Field-effect transistor
HOMO:	Highest occupied molecular orbital
HT-GPC:	High-temperature gel permeation chromatography
IBDF:	(3*E*,7*E*)-3,7-bis(2-oxoindolin-3-ylidene)benzo[1,2-*b*:4,5-*b*']difuran-2,6(3*H*,7*H*)-dione
IID:	Isoindigo
I_{DS}:	Drain-source current
$I_{on/off}$:	Current on-and-off ratio
LUMO:	Lowest unoccupied molecular orbital
M_n:	Number average molecular weight
M_w:	Weight average molecular weight
NIR:	Near infrared
NMR:	Nuclear magnetic resonance
OLED:	Organic light emitting diode
OPV:	Organic photovoltaic
OTFT:	Organic thin film transistor
TCE:	1,1,2,2-tetrachloroethane
TGA:	Thermal gravimetric analysis
THF:	Tetrahydrofuran

UV-Vis:	Ultraviolet-Visible spectrometry
V_{DS}:	Drain-source voltage
V_{GS}:	Gate voltage
V_T:	Threshold voltage
XRD:	X-ray diffraction
λ_{max}:	Maximum absorption (nm)
μ:	Mobility ($cm^2V^{-1}s^{-1}$)
μ_e:	Electron mobility ($cm^2V^{-1}s^{-1}$)
μ_h:	Hole mobility ($cm^2V^{-1}s^{-1}$)

Chaptor 1

Introduction

1.1 Printed Organic Electronics

Imagine walking out from a grocery store directly to your car without scanning each item in your shopping cart one by one at check out. Imagine a roll-and-go display that can change its content as requested. Or imagine dresses and coats that can charge mobile devices with solar cells fabricated on clothes. All these applications are based on printed organic electronic devices in which circuits made of organic materials are developed with printing techniques. Owing to the synthesis of new organic semiconducting materials and the improvement of the properties of existing materials, organic electronics have made its way into not only a mature research field but also a fast-growing industry. Organic semiconductors are different from inorganic materials in that they can provide attractive features such as solution processability, light weight, low cost and mechanical robustness. Displays based on organic light-emitting diode (OLED) and electronic paper (e-paper) are two applications of organic electronic that has been commercialized.

The driving force behind the research in organic electronics in both industry and academia is the idea of low-cost manufacturing of large area circuits by printing techniques.[1] By applying the existing printing techniques such as gravure and lithography in the development of circuits, electronics can be printed as newspapers at a fast rate and large quantities. This opens up opportunities for cost-effective production of item-level, disposable identification tags and large area sensor arrays. In addition, the low processing temperature (below 200 ^{o}C) of organic materials allows for developing circuits on a variety of flexible substrates such as plastic, clothes and paper for applications like roll-up displays.

There are shortcomings with printed electronics. The limitation of printed organic electronics lies in their low device performance compared to traditional inorganic materials such as silicon and germanium. In particular, single crystal silicon exhibit mobilities of 250 to 600 $cm^2V^{-1}s^{-1}$, while the highest mobilities reported for organic semiconductors so far are 1 to 10 $cm^2V^{-1}s^{-1}$. For this reason, it is not the aim of organic electronics to compete with traditional ones in the production of high-end products, but rather to capture the low cost feature of organic materials and explore new applications that are not accessible with traditional materials.

Today's research in printed electronics focus on three building blocks: organic light-emitting diodes (OLEDs), organic photovoltaics (OPVs) and organic thin film transistors (OTFTs). This study is devoted to preparing novel organic semiconductors for applications in OTFTs, but these materials are also potentially useful in OPVs.

1.2 Organic Thin Film Transistors (OTFTs)

The idea of field effect transistor (FET) was first proposed by J. E. Lilienfeld in 1930.[2] He described it as a method to control the flow of an electric current in an electrically conducting medium between two electrodes by controlling the electric field applied to a third electrode. A thin film transistor (TFT) is a special kind of FET, in which the components of the device are deposited as thin films on substrates. The term "organic thin film transistor" refers to a TFT in which the semiconductor layer is composed of an organic-based material, while the other components are not limited to organic materials. Organic thin film transistors (OTFTs) are fundamental elements of printed electronics and have been considered as competitive candidates in applications such as radio frequency identification tags (RFID), sensors, and smart cards where light weight, cost effectiveness and flexibility are required.[3,4] The printability of organic semiconductors has also opened up the application of OTFTs as active matrices in large-area display,[5] and the low processing temperature allows for the development of integrated circuits on plastic substrates.[3,6] Other than all the potential applications of OTFTs mentioned above, OTFT itself is a useful tool for extracting charge transport parameters of organic semiconductors.

An OTFT is composed of source, drain and gate electrodes, a dielectric (insulating) layer, and a semiconducting layer. Bottom-contact, bottom-gate and top-contact bottom-gate are two device configurations most commonly used in OTFTs (Figure 1). The semiconductor layer was developed on top of the source and drain contacts in the bottom-contact configuration, while in a top-contact OTFT the source and drain contacts are at the top of the organic semiconductor. In both device configurations, the gate electrode was at the bottom of dielectric insulating layer. Top-contact configuration is known to provide superior device performance than bottom-contact configuration due to the morphological defects at the semiconductor-source/drain contact interlayer in bottom-contact devices, which in turn lead to the formation of charge carrier traps and lowering of charge carrier mobility.[6] However, top-contact devices require source and drain contacts to be deposited though a shadow mask onto the organic semiconductor, and it is this process that limited their feasibility during manufacturing. Depending on the dominant charge carrier in the semiconductors, they are defined as p-type, n-type or ambipolar. P-type semiconductor transport hole (positive charges), while n-type transport electrons (negative charges). Ambipolar semiconductor can transport both holes and electrons.

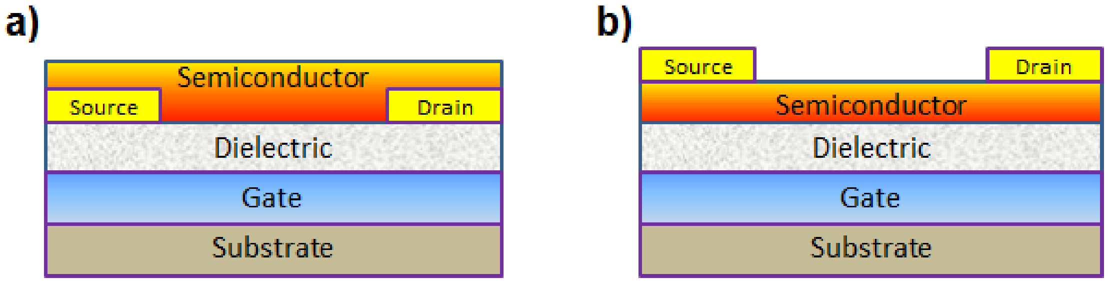

Figure 1. OTFT device configurations: a) Bottom-contact, bottom-gate device, with the organic semiconductor deposited on top of dielectric and the pre-patterned source and drain electrodes. b) Top-contact, bottom-gate device, with the source and drain electrodes deposited on top of organic semiconductor through a mask.

When evaluating an OTFT, three key performance parameters are charge carrier mobility (μ), threshold voltage (V_T) and current on-and-off ratio ($I_{on/off}$). The charge carrier mobility (μ) measures charge-carrier drift velocity per unit electric field applied, and the threshold voltage measures the voltage required to turn an OTFT to its "on" state. The current on-and-off ratio is the ratio of the current when an OTFT is in the accumulation mode (the "on" state) over the current when the OTFT is in the depletion mode (the "off" state). For an optimized OTFT to operate as an effective switch in display applications, it is expected to exhibit mobility comparable or even higher than that of amorphous silicon (~0.1 – 1 $cm^2V^{-1}s^{-1}$).[6] A current on-and-off ratio of ~10^6 or higher is needed to ensure low current in the off state for energy saving purposes. In addition, the OTFT should not exhibit a threshold voltage larger than 15 V.

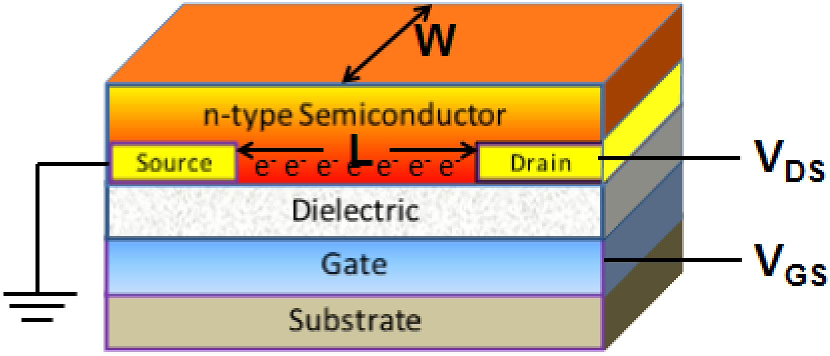

Figure 2. Schematic diagram of a bottom-contact, bottom-gate OTFT with n-type semiconducting channel.

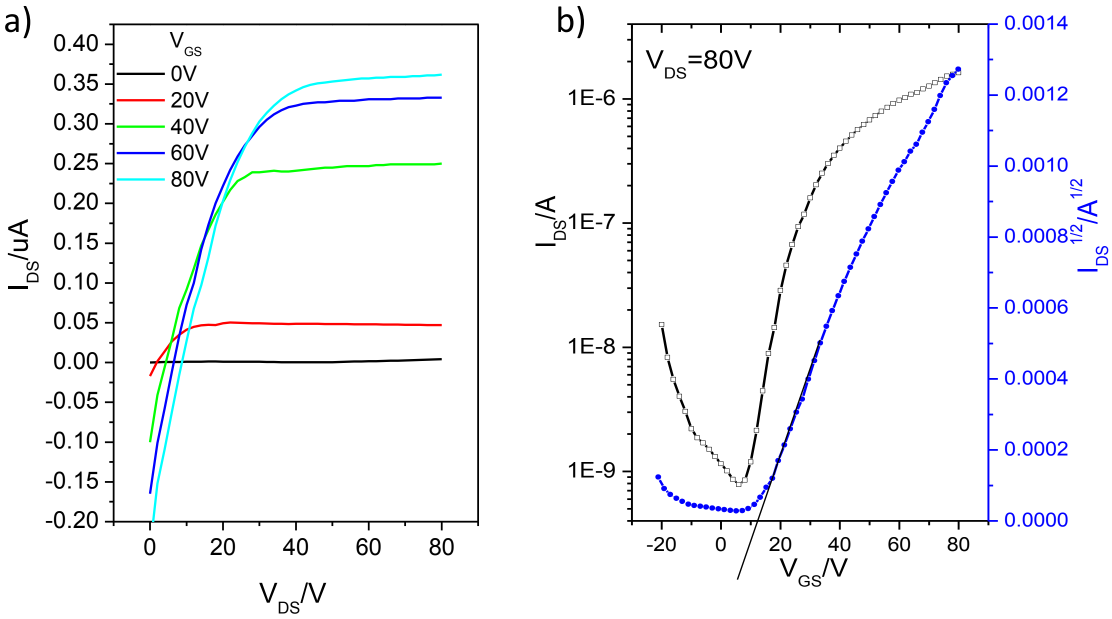

Figure 3. (a) Output characteristics (drain-source current, I_{DS}, vs. drain voltage, V_{DS}) and (b) transfer characteristics (I_{DS} vs. gate voltage, V_{GS}) from a bottom-contact, bottom-gate PMMA-encapsulated OTFT device fabricated with an n-type semiconductor thin film. Device dimensions: channel length $L = 30$ μm; channel width $W = 1000$ μm.

The working principle and the extraction of charge transport parameter can be explained using the bottom-contact, bottom gate OTFT device with an n-type semiconductor channel shown in

Figure 2. An OTFT acts an electronic switch, where the current flow between the source and drain electrodes is controlled by the magnitude of the electric field applied at the gate. When a positive gate bias (V_{GS}) is applied between the gate and source electrodes, the OTFT is turned "on" and electrons accumulate due to capacitive effect within the first few organic layers at the semiconductor-dielectric interface. This electron accumulation layer, also called a channel, allows charge carriers to flow from the source to the drain when a bias (V_{DS}) is applied between the two electrodes. When a negative gate voltage or a voltage smaller than V_T is applied, the OTFT is turned "off", and operates in depletion mode. In the case of p-type semiconductor, a negative gate bias should be applied to induce accumulation of holes and turn the device "on", and a positive gate voltage would turn the OTFT "off".

An output curve plots drain-source current, I_{DS}, versus drain voltage V_{DS} at various gate voltage, V_{GS}, as shown in Figure 3a. I_{DS} increases linearly as V_{DS} increases in the linear regime (low V_{DS}), and can be estimated from the following equation[7]:

$$\boldsymbol{I_{DS} = \frac{WC_i\mu}{L}\left(V_{GS} - V_T - \frac{V_{DS}}{2}\right)V_{DS}} \qquad (1)$$

where W is the channel width, L is the channel length, C_i is the capacitance per unit area of the dielectric, μ is the mobility, and V_T is the threshold voltage. In the saturation regime where $V_{DS} > (V_{GS} - V_T)$, I_{DS} tend to saturate and reaches plateau in the output curve.[8,9] I_{DS} then can be described by the equation:

$$\boldsymbol{I_{DSsat} = \frac{WC_i\mu}{2L}(V_{GS} - V_T)^2}. \qquad (2)$$

In the transfer curve (Figure 3b), I_{DS} is plotted versus V_{GS} at a constant V_{DS} within the saturated regime. By rewriting equation (2) as:

$$\boldsymbol{\sqrt{I_{DSsat}} = \sqrt{\frac{WC_i\mu}{2L}}(V_{GS} - V_T)} \ , \qquad (3)$$

one can predict a linear relationship between $\sqrt{I_{DSsat}}$ and V_{GS}. By plotting $\sqrt{I_{DSsat}}$ versus V_{GS} the mobility can be obtained from the slope of the straight line, and the threshold voltage can be extracted from the extrapolation of the line to zero current.

1.3 Polymer Semiconductors

The electrical charge carrier transport in polymers was discovered in the late 1980 by the Nobel Prize winners in chemistry in 2000, Alan J. Heeger, Alan, G. MacDiarmid and Hideki Shirakawa.[10–12] Since then, semiconducting polymers have attracted increasing research interest. Semiconducting polymers, together with conjugated small molecules are important functional materials for the realisation of OTFTs, and the mechanism of charge transport in polymeric materials has been studied.[13–17] Charge transport along the polymer chain is governed by delocalization of the charge carrier over the conjugated blocks, which is similar to charge transport in graphite, and can be as fast as 10^4 $cm^2V^{-1}s^{-1}$. On the other hand, charge transport between polymer chains is enabled by intermolecular electron hopping through π-π stacking. This requires the distance between two adjacent polymer chains to be smaller than 4 Å, thus placing a limit for charge carrier mobility in polymer semiconductors.

The weak intermolecular interaction between the neighboring molecules has been considered as the main reason for the low charge carrier mobility in polymer semiconductors. In order to decrease the π-π distance and improve the mobility in the polymer, one needs to either increase the area of π-π stacking or to increase the intermolecular interaction. Arranging electron donating and electron accepting building blocks alternatively in the main backbone of the polymer has been proven to be one of the most promising strategies to increase the intermolecular interaction. The donor-acceptor interaction is believed to induce self-assembly of the polymer main chain, thus increasing molecular ordering and decrease π-π distance. In addition to increasing intermolecular interaction, combining electron-donating and electron-withdrawing moieties in the polymer backbone can also tune the energy levels of the resulting polymer semiconductor. The strong electron-withdrawing groups in acceptor will lower the lowest unoccupied molecular orbital (LUMO) of polymer, and the electron-donating groups in donor will raise the highest occupied molecular orbital (HOMO) of the polymer. It has been experimentally found that a HOMO level higher than -5.5 eV but lower than -5.0 eV was essential for hole injection from metal electrodes and at the same time for air-stability against oxidation of the semiconductor.[18–20] For stable electron transport under ambient condition, a LUMO level lower than -4.0 eV with respect to vacuum level is required.[21–23] Hybridization of LUMO of acceptor and HOMO of donor also provides smaller bandgap, which is beneficial for light harvesting in OPVs.

A number of donor-acceptor (D-A) polymer semiconductors exhibiting high charge carrier mobility close to or greater than 1 $cm^2V^{-1}s^{-1}$ have been reported. Diketopyrrolopyrrole (DPP) based polymers have attracted extensive research interest in the past few years, and a large number of high performance organic semiconductors bearing DPP moieties have been constructed.[18] Some representative examples are shown in Scheme 1. The simplest DPP based D-A polymer combines a DPP and a thiophene in its repeating unit, DBT.[24] The very strong donor-acceptor interaction between the polymer chains requires long branched alkyl side chains to be introduced to achieve moderate to good solubility. Due to the strong electron withdrawing effect of DPP unit, **PDBTs** have low HOMO/LUMO energy levels of -5.4/-4.2 eV. **PDBT-HD** was reported to show balanced hole/electron mobilities up to 0.024/0.056 $cm^2V^{-1}s^{-1}$ in bottom-gate, top contact OTFT. Kanimozhi *et al.* copolymerized two DBT monomers with different side chains via Suzuki coupling, and the highest unipolar electron mobility observed for **N-CS2DPP-OD-TEG** exceeded 3 $cm^2V^{-1}s^{-1}$ on top-gate, bottom contact OTFTs with polymer thin film annealed at 100 ^oC and aluminum as the source and drain electrodes.[25] Bijleveld *et al.* introduced one more thiophene ring into the D-A copolymer backbone and prepared **PDPP3T-HD**.[26] Recently the influence of the solubilizing side chains on the OTFT performance was studied by Lee *et al.*, and they achieved high hole mobility of 1.57 $cm^2V^{-1}s^{-1}$ with electron mobility of 0.18 $cm^2V^{-1}s^{-1}$ for **PDPP3T-OD** polymer thin films annealed at 150 ^oC.[27] They also concluded from the AFM and XRD results that longer branched alkyl side chains in the polymer improved the crystalline structure, which in turn help to improve the charge transport. Li *et al.* developed copolymer **PDQT**, comprising a *N*-substituted DPP and four non-substituted thiophene in one repeating unit, via Stille-coupling of dibrominated DBT with 5,5'-bis(trimethylstannyl)bithiophene.[28] Non-annealed thin films of **PDQT** exhibited high hole mobilities up to 0.89 $cm^2V^{-1}s^{-1}$ on bottom-gate, top-contact OTFT devices using gold as the source and drain electrodes. Chen *et al.* copolymerized dibromo functionalized DBT with distannyl bithiophenyl-vinylene to prepare **PDVT-8** and **PDVT-10**, which exhibited dramatically high hole mobilities of 2.0-4.5 $cm^2V^{-1}s^{-1}$ and 4.0-8.2 $cm^2V^{-1}s^{-1}$, respectively.[29] They demonstrated that polymer **PDVT-10** with a longer side chain than **PDVT-8** was easier to reorganize during thermal annealing to more ordered structure with shorter π-π stacking distance, resulting in higher mobility. This is in agreement with the observation for **PDPP3T-HD** and **PDPP3T-OD**.

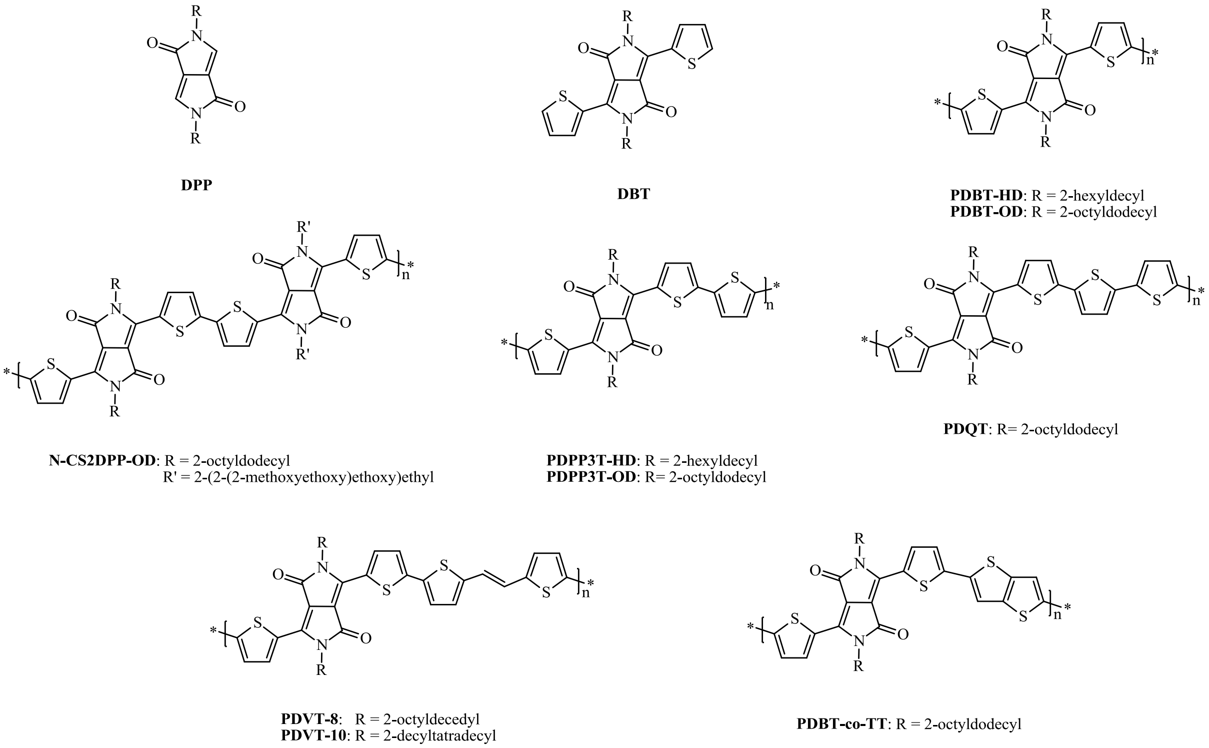

Scheme 1. Structure of DPP, DBT and DPP based donor-acceptor copolymers.

Li *et al.* also incorporated fused thiophene rings into the backbone of DPP based copolymer and prepared **PDBT-co-TT**, a copolymer of DBT with a thieno[3,2-b]thiophene, and they reported a high hole mobility of 0.94 $cm^2V^{-1}s^{-1}$ for films annealed at 200 ^oC.[30] Recently, a record-high hole mobility in polymer semiconductor of 10.5 $cm^2V^{-1}s^{-1}$ was achieved for **PDBT-co-TT** by Li *et al.* in their study in the effect of reaction conditions on molecular weight and device performance of the polymer.[31] Their polymer was measured to have a number average molecular weight of ~110 kDa with a strong tendency to form aggregation in solvents. The high molecular weight together with the optimized device fabrication process might account for the extremely high hole mobilities observed. In addition to thiophene-containing building blocks, other five-membered heterocyclic structures such as furan[32,33] and selenophene[34–36] have also been incorporated into the backbone of DPP based polymers, some of which showed high mobilities than 1 cm^{2}V^{-1}s^{-1}.

Amide is a strong electron-withdrawing functional group that has been widely introduced to D-A copolymers, of which DPP is a representative example. Another building block containing amide functional group that is being studied extensively recently is isoindigo (IID) (Scheme 2). The first set of isoindigo based donor-acceptor was reported by Stalder et al as a promising candidate for photovoltaic applications.[37] Lei *et al.* then conducted systematic research on isoindigo based polymer semiconductors for OTFTs.[38–42] They copolymerized IID with a variety of electron donors including biselenophene (**IID-Se**), bithiophene (**IIDDT**), benzodithiophene (**IID-BDT**), and other thiophene-containing units.[39] Among all the reported IID-based donor-acceptor copolymers, **IIDDT** showed the best performance on bottom-gate, top-contact OTFTs with a highest hole mobility of 1.06 cm^2 V^{-1} s^{-1} ($I_{on/off}$ = 10^6 – 10^7) and an average hole mobility of 0.66 cm^2 V^{-1} s^{-1} recorded under ambient condition. **IID-Se** and **IID-BDT** also showed high hole mobilities of 0.46 and 0.37 cm^2 V^{-1} s^{-1}, respectively. Later, Lei *et al.* studied the effect of halogenation of IID on the energy level and charge transport of the resulting polymers.[40,42] They prepared fluorinated and chlorinated IID monomers and copolymerized them with bithiophene. Their study on **PFII2T** demonstrated that introducing the strong electron-withdrawing fluorine substituent into the IID core effectively lowered the LUMO of the polymer and facilitated ambipolar charge transport with hole/electron mobilities up to 1.85/0.43 cm^2 V^{-1} s^{-1}.[40] The chlorinated isoindigo monomer was copolymerized with not only bithiophene but also biselenophene to afford **PCII2T** and **PCII2Se**.[42] **PCII2T** exhibited balanced hole/electron mobilities of 0.38/0.47 cm^2 V^{-1} s^{-1} in a glovebox and 0.51/0.42 cm^2 V^{-1} s^{-1} under ambient condition. Incorporation of chlorinated IID in **PCII2Se** increased not only the hole mobility to 0.74 cm^2 V^{-1} s^{-1} but also the electron mobility to 0.58 cm^2 V^{-1} s^{-1} when the OTFT devices were tested in air. Chlorination of IID was proven to have similar influence on HOMO/LUMO energy levels as fluorination through their study. Mei *et al.* introduced siloxane-terminated solubilizing side chains to **IIDDT** and prepared **PII2T-Si**, which exhibited hole mobilities higher than 2 cm^2 V^{-1} s^{-1}.[43] Sonar *et al.* copolymerized IID acceptor with naphthalene and anthracene electron donors.[44] **PISD-ANT** showed a highest hole mobility of 0.013 cm^2 V^{-1} s^{-1} on top-contact, bottom-gate OTFTs.

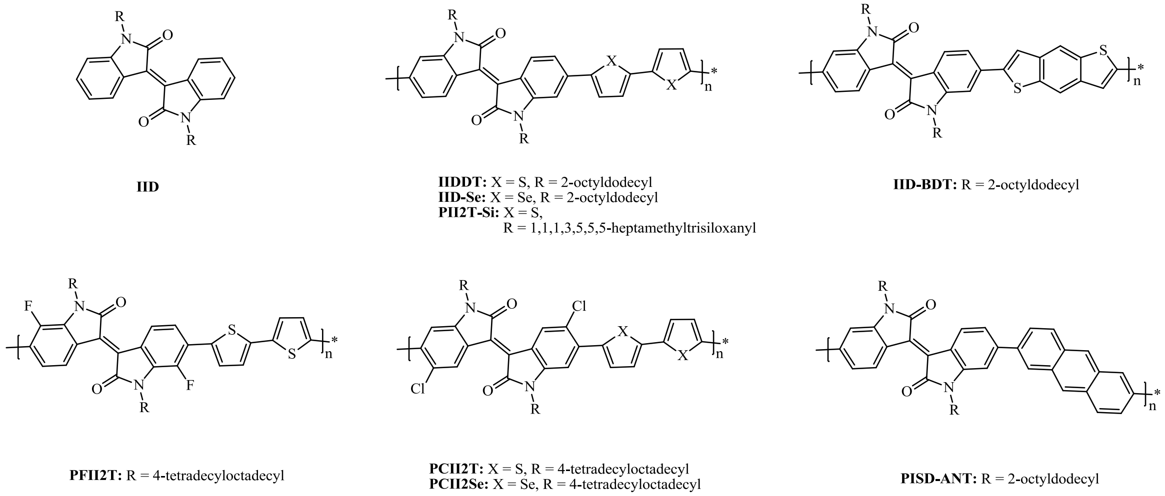

IID

IIDDT: X = S, R = 2-octyldodecyl
IID-Se: X = Se, R = 2-octyldodecyl
PII2T-Si: X = S,
R = 1,1,1,3,5,5,5-heptamethyltrisiloxanyl

IID-BDT: R = 2-octyldodecyl

PFII2T: R = 4-tetradecyloctadecyl

PCII2T: X = S, R = 4-tetradecyloctadecyl
PCII2Se: X = Se, R = 4-tetradecyloctadecyl

PISD-ANT: R = 2-octyldodecyl

Scheme 2. Structure of IID and IID based donor-acceptor copolymers.

Another building block widely used in organic semiconductors is thiazole (Scheme 3). Thiazole is a heterocyclic structure commonly used in organic semiconductors, and the introduction of thiazole-based moieties into organic semiconductors dates back to the 1990s.[45] Since then many small molecules or conjugated polymers based on thiazole have been reported to exhibit high mobilities in OTFTs. Small molecule organic semiconductor based on bithiazole has been reported to show mobility as high as 1.83 cm^2 V^{-1} s^{-1} by Ando *et al.*[46] Paek *et al.* prepared **PQT2T** and **PTZ2T** to study the influence of the electron-deficient thiazole moiety on the properties of polythiophene.[47] The thiazole-containing copolymer **PTZ2T** showed a higher degree of ordering as induced by donor-acceptor interaction. The replacement of bithiophene by bithiazole also led to a smaller bandgap and lower HOMO/LUMO energy levels in **PTZ2T** due to the electron-withdrawing thiazole rings. As a result, **PTZ2T** showed a hole mobility of 1.1×10^{-3} cm^2 V^{-1} s^{-1} on OTFTs, which is 18 times higher than the mobility observed for **PQT2T**. Liu *et al.* reported an air stable copolymer of *N*-alkyldithienopyrrole and bithiazole, **PBTzDTP-C12**, which exhibited hole mobility up to 0.14 cm^2 V^{-1} s^{-1} with current on-and-off ratio of 10^6 in OTFTs fabricated with non-annealed polymer thin films.[48]

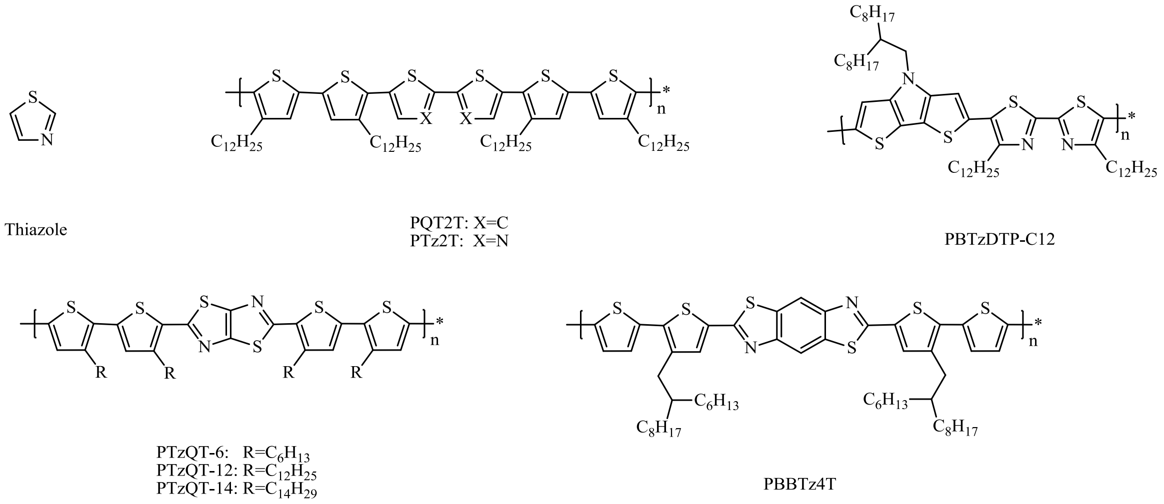

Scheme 3. Structures of thiazole and thiazole based donor-acceptor copolymers.

Fused thiazole rings were also incorporated into the backbone of poly(alkylthiophenes) by Osaka *et al.*[49] They prepared air-stable **PTzQTs** with different side chains (hexyl, dodecyl and tetradecyl), of which **PTzQT-14** with the longest tetradecyl solubilizing side chain showed the best device performance on bottom-contact OTFTs with hole mobilities as high as 0.3 cm^2 V^{-1} s^{-1} ($I_{on/off} = 10^5 – 10^7$) observed.[50] Benzobisthiazole based copolymers were also studied. **PBBTz4T** with a branched alkyl chain showed hole mobilities up to 0.26 cm^2 V^{-1} s^{-1} with on to off current ratio of ~ 10^7. [51]

1.4 Project Scope and Objectives

As we can find from examples listed above most organic semiconductor with high performance reported so far are hole transporting (p-type), whereas n-type, electron transport polymer semiconductors have been falling behind their p-type counterparts and there are very few stable n-type polymer semiconductors reported so far.[52–54] This is due to the relatively large electron injection energy barrier between the work function of metal contacts and the LUMO energy level of the organic semiconductor. Another obstacle needed to be overcome when constructing electron transporting organic semiconductors is the instability of organic anions in the presence of water and oxygen.[55] In order to lower the LUMO energy level of a polymer semiconductor to facilitate easier electron injection, a strong electron-deficient acceptor is needed to bring down the LUMO of the polymer. Acceptors with strong electron-withdrawing groups will also increase electron affinity of the polymer, thus improving the air/moisture stability. The library of electron donors for D-A copolymers is far richer than that of electron acceptors with much more attention paid to electron donating building blocks. The objective of this project is to develop novel electron acceptor building blocks, which will then be used to construct D-A copolymers with existing electron donors.

Chaptor 2

IBDF Based Donor-Acceptor Copolymers for OTFTs

2.1 Novel (3*E*,7*E*)-3,7-bis(2-oxoindolin-3-ylidene)benzo[1,2-*b*:4,5-*b'*]difuran-2,6(3*H*,7*H*)-dione (IBDF) Monomer for Constructing Donor-Acceptor Copolymers

2.1.1 Molecular Design

In this study, we report the use of a strong electron accepting building block, (3*E*,7*E*)-3,7-bis(2-oxoindolin-3-ylidene)benzo[1,2-*b*:4,5-*b*']difuran-2,6(3*H*,7*H*)-dione (IBDF) for the synthesis of new D-A polymers. IBDF compounds were first prepared as colourants and pigments.[56,57] A benzodifurandione was incorporated into isoindigo (IID) between two isatin moieties to afford a large fused aromatic ring structure with extended conjugation, which would increase the π-π overlap and intermolecular interaction of its polymers. The electron-withdrawing lactone units in the central core coupled with the lactam units on the outer oxoindoline moieties make the IBDF unit highly electron deficient.

We started off our study on IBDF-based polymers by first conducting a computer simulation on a simple IBDF molecule, IBDF-Me, which has methyl groups at the nitrogen atoms, to elucidate the coplanarity, electron distribution, and energy levels of the IBDF building block (Figure 4). The modelling results clearly showed that the IBDF unit takes a highly coplanar geometry due to the rigid C=C bond connections between the benzodifurandione core and the oxoindoline units. The electrons in the highest occupied molecular orbital (HOMO) are quite evenly distributed, while in the lowest unoccupied molecular orbital (LUMO), the electrons are more localized around the benzodifurandione core. The HOMO and LUMO energy levels of IDBF-Me are calculated to be -5.97 eV and -3.59 eV, respectively. As comparative examples, methyl-substituted DPP and IID molecules, 2,5-dihydro-2,5-dimethyl-3,6-di-2-thienyl-pyrrolo[3,4-*c*]pyrrole-1,4-dione (DBT-Me) and (*E*)-3-(1,2-dihydro-1-methyl-2-oxo-3*H*-indol-3-ylidene)-1,3-dihydro-1-methyl-2*H*-indol-2-one (IID-Me), were also simulated (Figure 5). The HOMO/LUMO levels are -5.16 eV/-2.75 eV for DBT-Me and -5.70 eV/-2.76 eV for IID-Me, respectively. These results suggested that the IBDF building block is significantly more electron deficient than the DPP and IID moieties and is potentially useful for constructing stable n-type semiconductors.

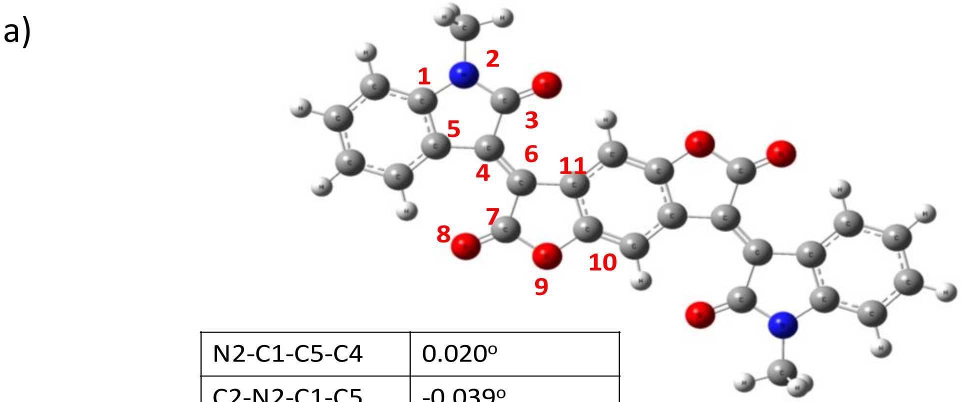

N2-C1-C5-C4	0.020°
C2-N2-C1-C5	-0.039°
C5-C4-C6-C7	0.112°
C6-C11-C10-O9	0.011°
C7-C6-C11-C10	0.003°
C5-C4-C6-C11	179.907°

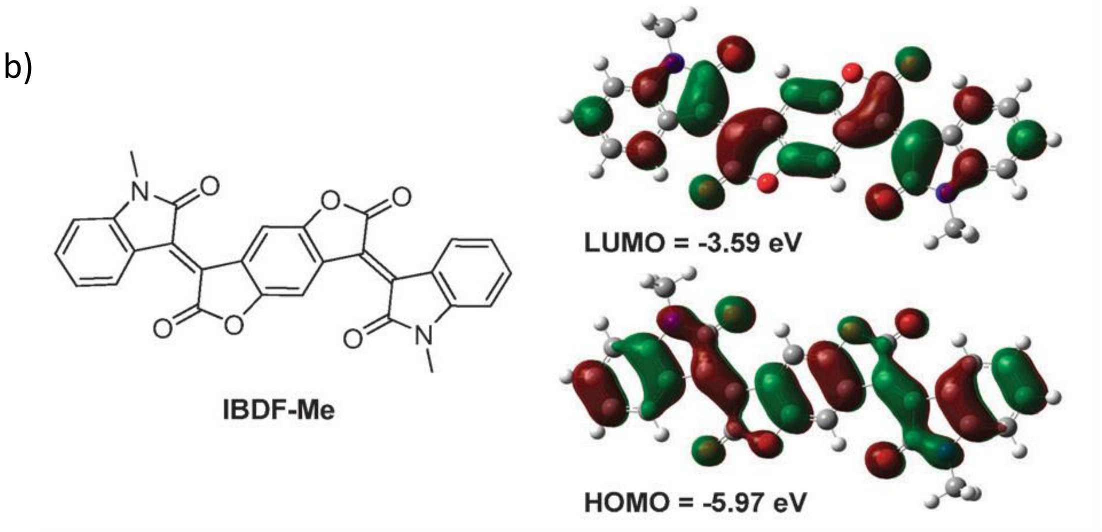

Figure 4. (a) Some dihedral angle values obtained by computer simulation for IBDF-Me, indicating that this molecule is highly coplanar; (b) The structure of (3*E*,7*E*)-3,7-bis(1-methyl-2-oxoindolin-3-ylidene)benzo[1,2-*b*:4,5-*b*']difuran-2,6(3*H*,7*H*)-dione (IBDF-Me) and its optimized HUMO/LUMO electron distribution diagrams obtained by computer simulation. – Reproduced by permission of The Royal Society of Chemistry

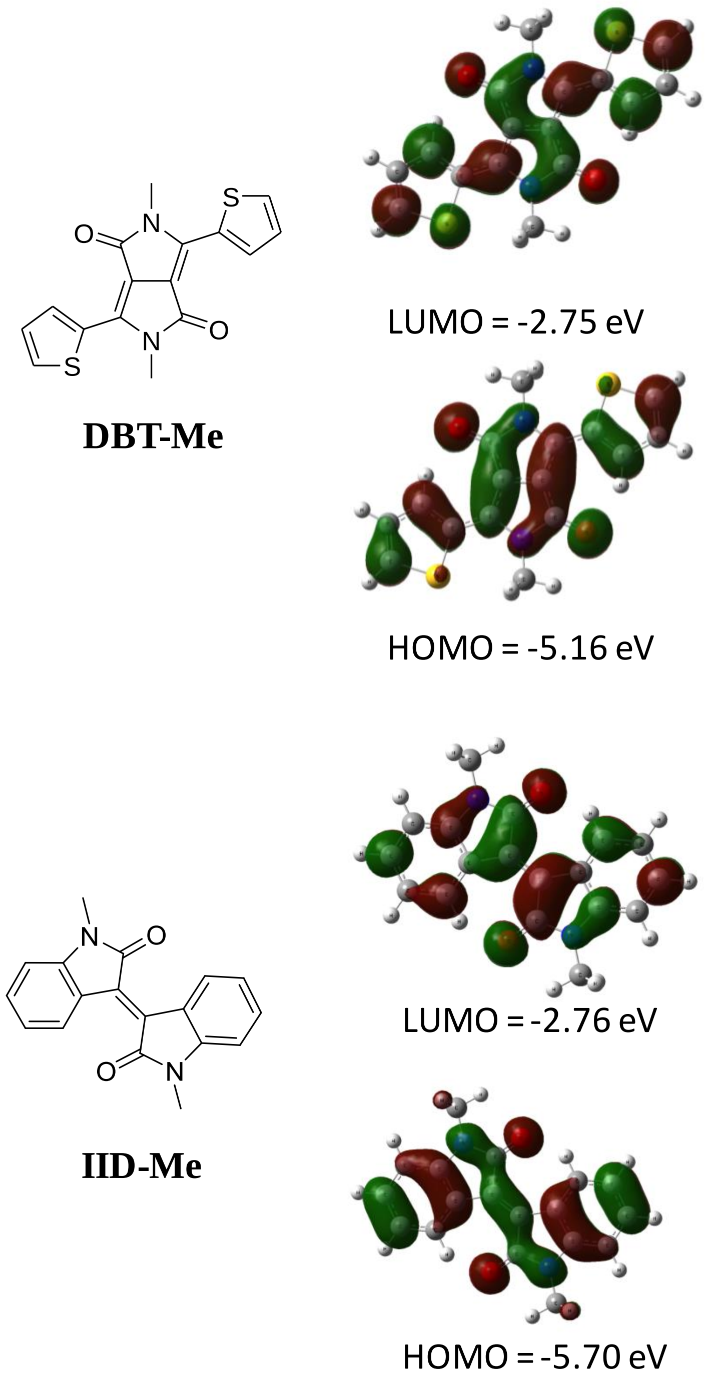

Figure 5. HOMO/LUMO orbitals of DBT-Me and IID-Me and the calculated HOMO/LUMO energy levels with respect to vacuum (0 eV). – Reproduced by permission of The Royal Society of Chemistry

2.1.2 Synthesis of 6-IBDF Monomer

Although the synthesis of IBDF pigment has been reported, this large fused aromatic compound was not soluble in any common solvents. In order to utilize IBDF structure in the D-A copolymer, strategies should be applied to solubilize the molecule. Attempts were made to introduce branched alkyl chains to the nitrogen atom through base-catalyzed *N*-alkylation. However, intolerance of the lactone group in the center core made this route unapproachable. Introduction of the alkyl chain was achieved by a two-step process, alkylation of 6-bromo-isatin followed by coupling with benzodifurandione in acetic acid. In this approach, soluble IBDF compounds can be achieved in moderate yield.

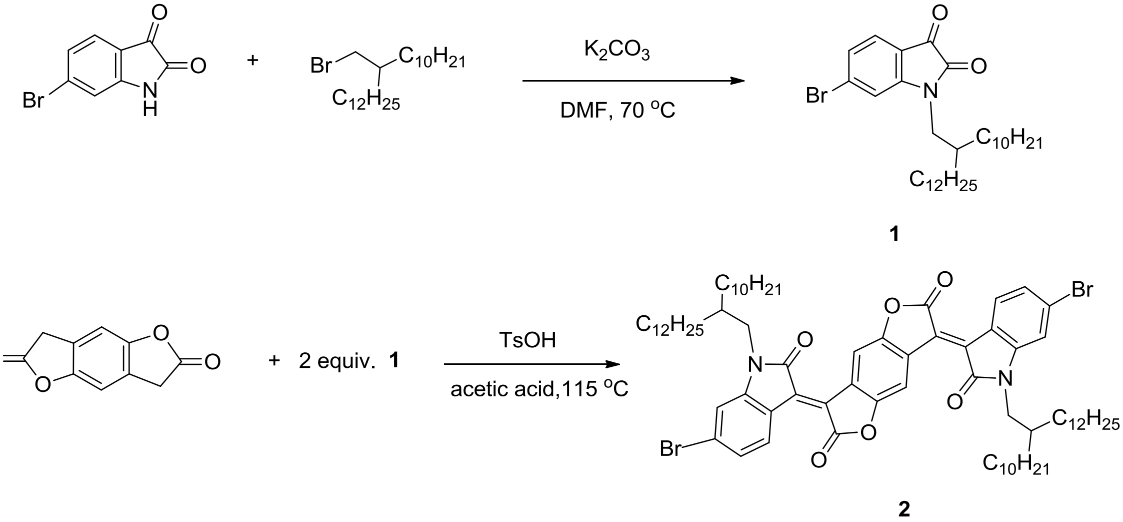

Scheme 4. Synthesis route of 6-Br-IBDF monomer.

The synthesis route for 6-Br-IBDF monomer was outlined in Scheme 4. Compound 6-bromo-1-(2-decyltetradecyl)indoline-2,3-dione (**1**) was conveniently prepared from 6-bromoindoline-2,3-dione via *N*-alkylation. The use of long, branched 2-decyltetradecyl groups was intended to improve the solubility of the final IBDF polymers. Compound **1** was then reacted with benzo[1,2-*b*:4,5-*b*']difuran-2,6(3*H*,7*H*)-dione, which was prepared via an established synthesis route,[58,59] to afford (3*E*,7*E*)-3,7-bis(6-bromo-1-(2-decyltetradecyl)-2-oxoindolin-3-ylidene)benzo[1,2-*b*:4,5-*b*']difuran-2,6(3*H*,7*H*)-dione (**2**), 6-Br-IBDF for short. Since the purity of the monomer significantly affects the chain length and molecular weight of the polymer, which in turn will influence the mobility of the resulting semiconducting polymer, the product of **2** was purified three times by column chromatography on silica gel and three times through recrystallization from dichloromethane-isopropanol to afford the final monomer used in Stille-coupling copolymerization.

2.2 Preparation and characterization of P6-IBDF-T

2.2.1 Synthesis of P6-IBDF-T

The first 6-IBDF polymer prepared in this study was **P6-IBDF-BT**, in which 6-Br-IBDF was copolymerized with 5,5’-bis(trimethylstannyl) bithiophene via Stille coupling (Scheme 5). Although bearing very large branched 2-decyltetradecyl side chains, **P6-IBDF-BT** is essentially insoluble in any solvent, indicating the very strong intermolecular interactions due to the large fused IBDF building block and the relatively linear backbone structure.

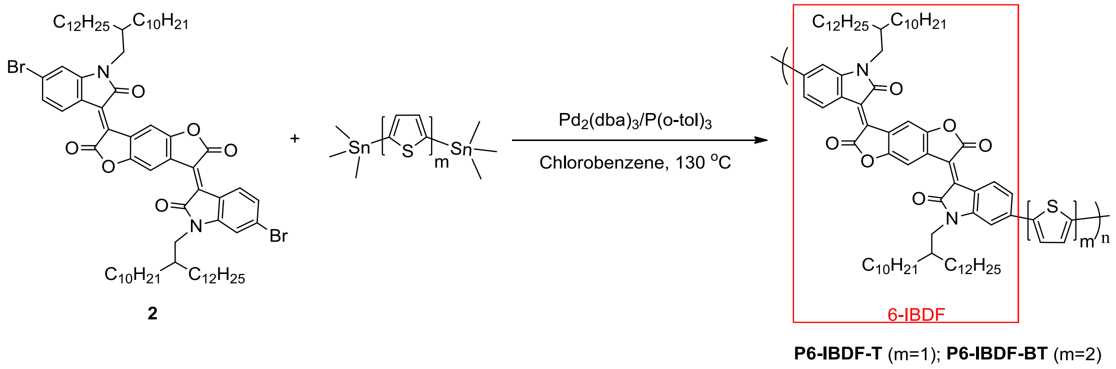

Scheme 5. Synthesis of **P6-IBDF-T** and **P6-IBDF-BT** via Stille-coupling.

P6-IBDF-T was then prepared via Stille coupling polymerization of **2a** with 2,5-bis(trimethylstannyl) thiophene, and purified using Soxhlet extraction. **P6-IBDF-T** is quite soluble in several solvents such as tetrachloroethane, chlorobenzene and 1,2-dichlorobenzene, because this polymer has a more zigzagged backbone. The number (M_n) and weight (M_w) average molecular weights of **P6-IBDF-T** were measured to be 34,200 and 50,100, respectively, using a high-temperature gel-permeation chromatography (HT-GPC) at a column temperature of 140 °C with 1,2,4-trichlorobenzene as an eluent and polystyrene as standards (Figure A-1). This polymer was fully characterized by UV-Vis, CV, TGA, AFM, and XRD to extract its optical bandgap, energy levels, thermal stability and crystallinity.

2.2.2 Characterization of P6-IBDF-T by DSC, TGA, UV-Vis, CV, AFM and XRD

The thermal behaviour of the polymers was characterized by thermal gravimetric analysis (TGA), which indicated that **P6-IBDF-T** has good thermal stability with a 5 % weight loss observed at 385 °C (Figure 6). Neither exothermic nor endothermic processes were observed in the DSC measurement of the polymer thin film, suggesting the absence of crystalline domains (Figure 7). **P6-IBDF-T** in tetrachloroethane (TCE) exhibited the maximum absorption (λ_{max}) at 744 nm and a similarly intense peak at 808 nm (Figure 8). In the solid thin film, both peaks slightly red shifted to 748 nm and 816 nm, respectively. The optical band gap calculated from the absorption onset of the polymer thin film is ~1.36 eV. The narrow band gap is due to the extended π-conjugation along the polymer backbone as well as strong intramolecular and intermolecular D-A interactions.

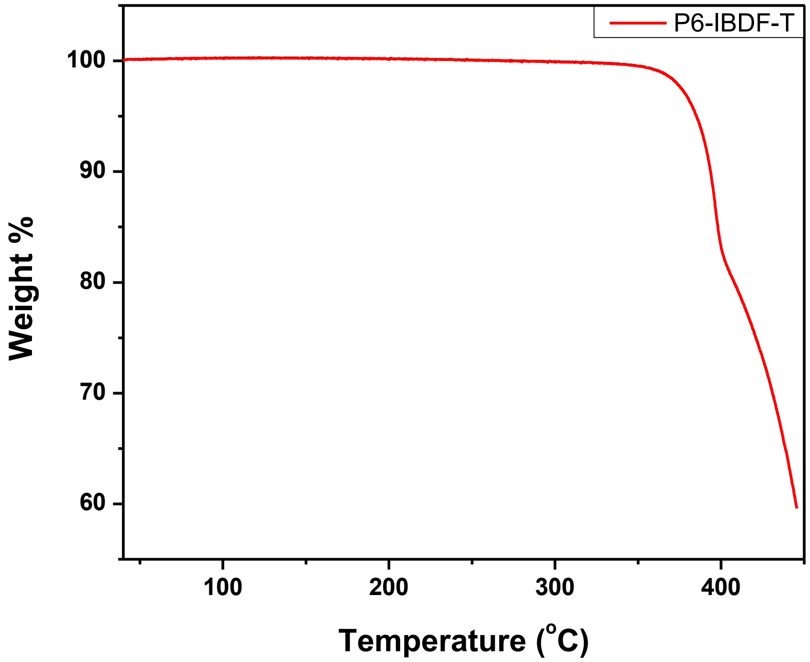

Figure 6. TGA curve of **P6-IDBF-T** measured with a heating rate of 10 ℃·min^{-1} under N_2. – Reproduced by permission of The Royal Society of Chemistry

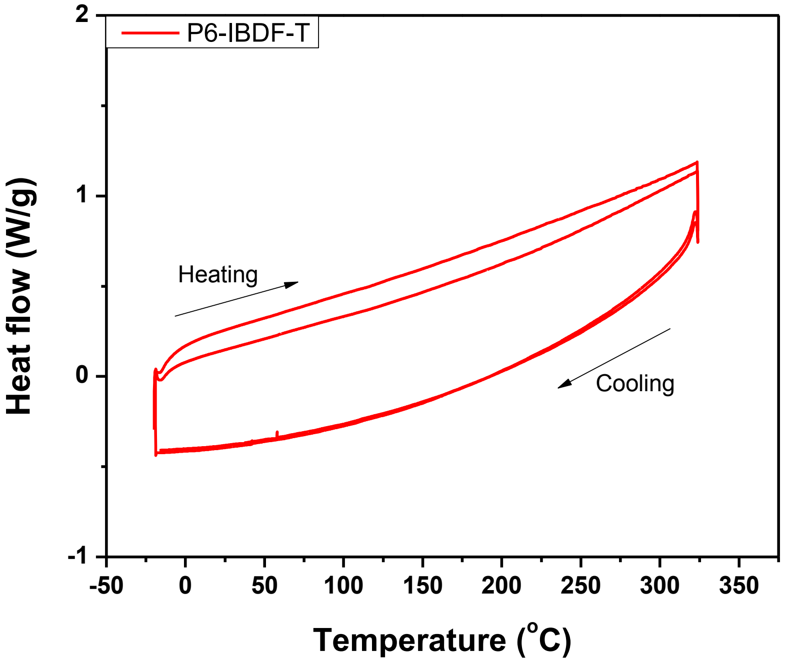

Figure 7. Differential scanning calorimetry (DSC) profiles of **P6-IBDF-T** obtained at a scanning rate of 10 ℃ min^{-1} under nitrogen.

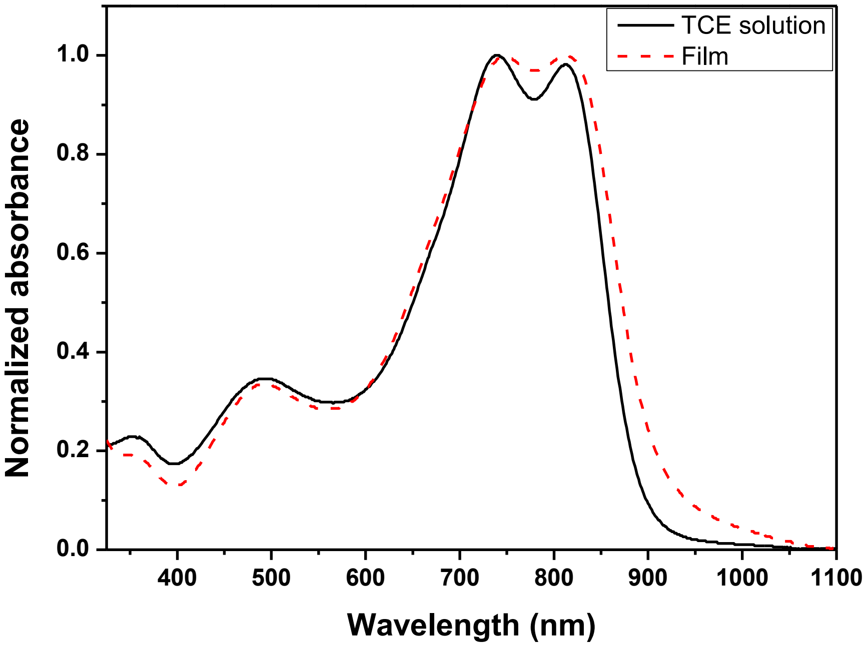

Figure 8. UV-vis-NIR absorption spectra of **P6-IBDF-T** in tetrachloroethane (TCE) and in thin film. – Reproduced by permission of The Royal Society of Chemistry

The cyclic voltammogram (CV) of **P6-IBDF-T** showed very reversible and reproducible redox cycles (Figure 9), suggesting that this polymer is stable towards both oxidation and reduction processes. The HOMO and LUMO energy levels were estimated from the oxidation and reduction onset potentials to be -5.79 eV and -4.11 eV, respectively. The LUMO level estimated from the between the LUMO level values obtained by two methods is considered due to the exciton binding energy of this polymer.[24,60] Nevertheless, the LUMO level of **P6-IBDF-T** is among the lowest LUMO/electron affinity values reported for n-type organic semiconductors,[23,53,61–63]which should be beneficial for electron injection and transport in OTFT devices.[21,64]

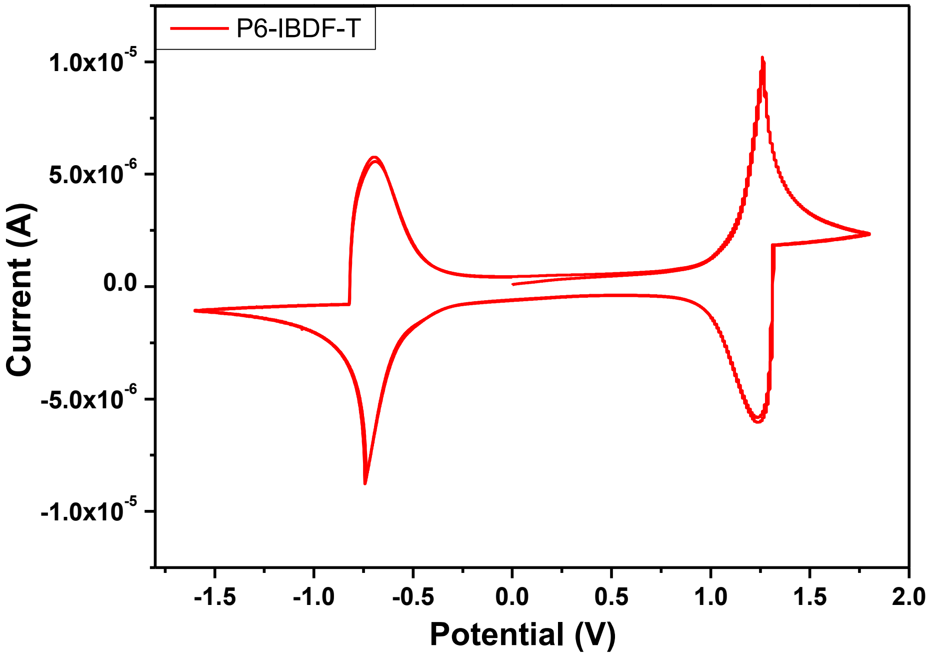

Figure 9. Cyclic voltammograms (two cycles) of a **P6-IBDF-T** thin film showing two oxidative and reductive cycles at a scan rate of 0.05 Vs^{-1}. The electrolyte was 0.1 M tetrabutylammonium hexafluorophosphate in anhydrous acetonitrile. – Reproduced by permission of The Royal Society of Chemistry

The surface morphology of **P6-IBDF-T** thin films spin coated on dodecyltrichlorosilane (DTS) modified SiO_2/Si wafer substrates were examined with atomic force microscopy (AFM). Tightly packed grains of ~50 nm in size are observed (Figure 10). However, the X-ray diffraction (XRD)

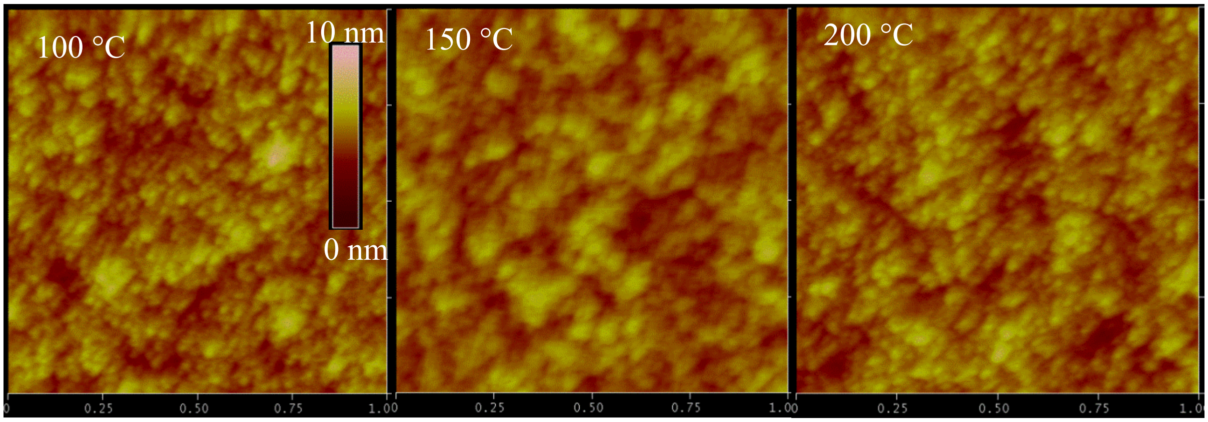

Figure 10. AFM height images (2 × 2 μm) of P6-IBDF-T thin films (~35 nm) spin-coated on DTS-modified SiO_2/Si substrates and annealed at different temperatures for 15min under nitrogen. – Reproduced by permission of The Royal Society of Chemistry

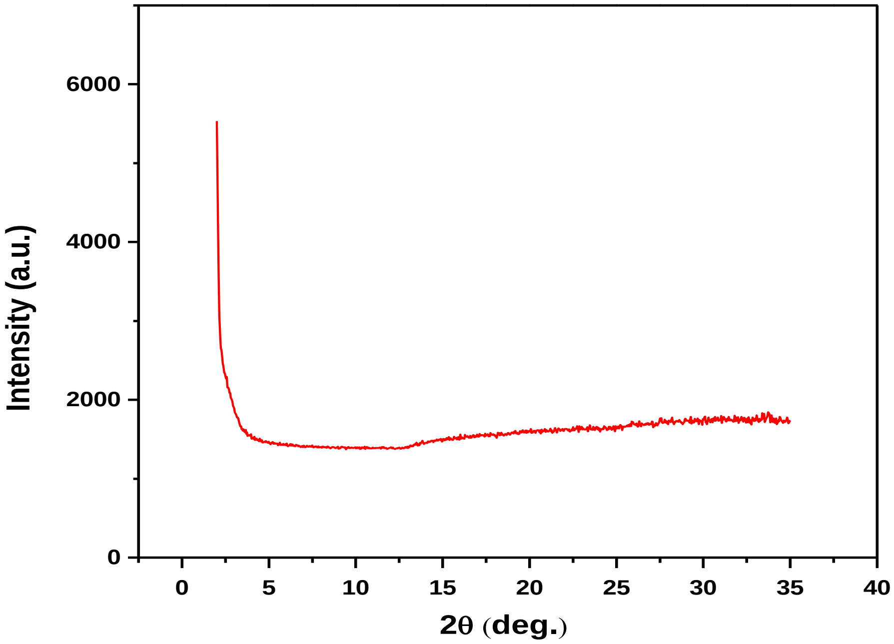

Figure 11. XRD diagram obtained from the spin-coated **P6-IDBF-T** thin film on dodecyltrichlorosilane (DTS)-modified SiO_2/Si substrates annealed at 150 °C in nitrogen. – Reproduced by permission of The Royal Society of Chemistry

analysis of the polymer films showed no appreciable long range order diffraction peaks (Figure 11). These indicated that these **P6-IBDF-T** films have poor crystallinity, which was in agreement with the DSC result.

2.2.3 Device Performance of P6-IBDF-T

P6-IBDF-T was evaluated as a channel semiconductor in OTFTs using a bottom-gate, bottom-contact configuration. A p-doped conductive Si wafer substrate with a ~200 nm thermal grown SiO_2 gate dielectric layer was pre-patterned with gold source/drain contact pairs using conventional photolithography and thermal deposition. Prior to use, the SiO_2 layer was modified with a monolayer of dodecyltrichlorosilane (DTS). A **P6-IBDF-T** solution was then spin coated on top of the SiO_2 layer to form a ~35 nm polymer film as the channel. After the semiconducting layer was annealed at a certain temperature for 15 min in nitrogen, the devices were optionally encapsulated with a layer of PMMA (~500 nm in thickness). Devices were characterized in air in dark.

OTFT devices with PMMA encapsulation exhibited typical n-channel transistor characteristics. The electron mobility of the P6-IBDF-T films annealed at 100 ^{o}C was up to 2.2×10^{-3} cm^{2}V^{-1}s^{-1} (current on-to-off ratio, $I_{on/off}$ = 1.1×10^{3}). After the films were annealed at 150 ^{o}C, the mobility increased to 3.0×10^{-3} cm^{2}V^{-1}s^{-1} ($I_{on/off}$ = 2.1×10^{3}). Annealing at 200 ^{o}C further improved the electron mobility to 5.4×10^{-3} cm^{2}V^{-1}s^{-1} ($I_{on/off}$ = 6.4×10^{3}) (Figure 12a and b). Increasing the annealing temperature further to 250 ^{o}C led to a decrease in mobility. The observed unipolar electron transport of this polymer is due to its very low-lying LUMO (-4.43 eV) and HOMO (-5.79 eV) levels with respect to the work function (~4.5-4.9 eV[65,66]) of the gold source/drain contacts. The low LUMO level facilitates the electron injection from gold to the polymer and stabilizes the electron transport,[53] while the low HOMO level builds up a large barrier for the hole injection. Surprisingly, the devices without encapsulation showed even higher electron mobility values, while distinct hole transport characteristics were also observed. The electron/hole mobilities are up to 8.2 ×10-3/1.0×10^{-2} cm^{2}V^{-1}s^{-1} for the 150 ^{o}C-annealed polymer films (Figure 12c). As the annealing temperature increased to 200 ^{o}C, the electron mobility improved slightly to 9.0×10^{-3} cm^{2}V^{-1}s^{-1}, while the hole mobility dropped to 4.9×10^{-3} cm^{2}V^{-1}s^{-1}.

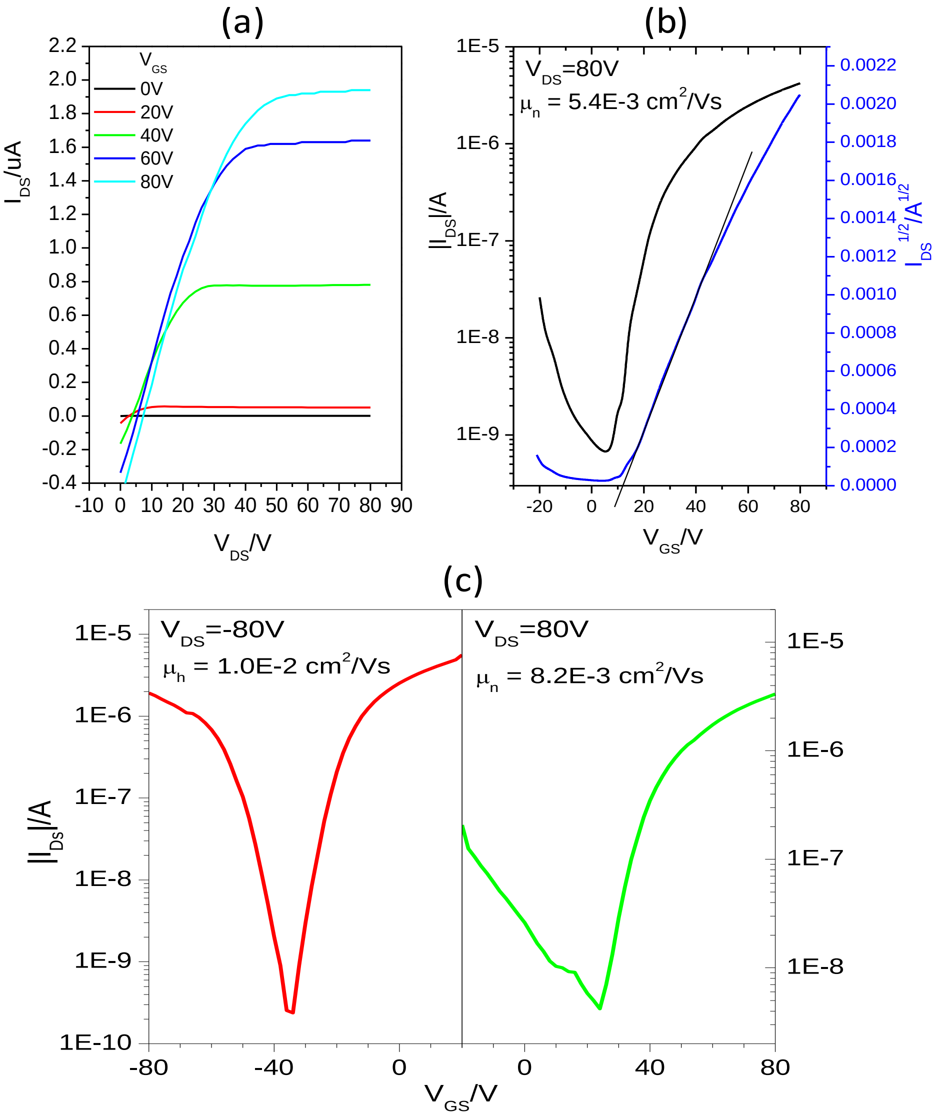

Figure 12. (a) and (b) show the output and transfer curves in the electron enhancement mode of a PMMA-encapsulated OTFT device fabricated with **P6-IBDF-T** thin film annealed at 150 °C; and (c) shows the transfer curves in the hole (left) and electron (right) enhancement modes of an OTFT without any encapsulation. **P6-IBDF-T** thin films annealed at 200 °C were used as the channel layers. – Reproduced by permission of The Royal Society of Chemistry

The mobilities PMMA-encapsulated and non-encapsulated OTFTs fabricated **P6- IBDF-T** thin films annealed at different temperatures are summarized in Table 2.1. The reason for the transition of these OTFTs from n-type to ambipolar charge transport upon exposure to air is still unclear. It probably relates to interactions of the water or oxygen molecules in air with P6-IBDF-T or the gold contacts, which might have altered the energy structures of the polymer or the work function of gold[66] to aid the injection and transport of holes.

Since **P6-IBDF-T** thin films are amorphous, the mobility values are quite impressive compared to many other amorphous polymers. Higher mobility is expected for the IBDF polymers with more linear structures such as **P6-IBDF-BT**, which should have more ordered molecular organization. Future work engaged in side chain engineering of **P6-IBDF-BT** and synthesis of other IBDF copolymers with better solubility and crystallinity are necessary to improve the charge transport performance of this new class of polymers.

Table 2.1 Summary of OTFT device performance using P6-IDBF-T as the channel layers. [a] . – Reproduced by permission of The Royal Society of Chemistry

Encapsulation with ~500 nm PMMA	Annealing temperature	Charge transport	Mobility ($cm^2V^{-1}s^{-1}$)	$I_{on/off}$
Yes	100 °C	n-type	$\mu_e = 1.5\text{-}2.2 \times 10^{-3}$	$\sim 10^3$
	150 °C	n-type	$\mu_e = 2.4\text{-}3.0 \times 10^{-3}$	$\sim 10^3$
	200 °C	n-type	$\mu_e = 4.2\text{-}5.4 \times 10^{-3}$	$\sim 10^3\text{-}10^4$
	250 °C	n-type	$\mu_e = 0.9\text{-}1.5 \times 10^{-3}$	$\sim 10^3$
No	150 °C	ambipolar	$\mu_e = 5.5\text{-}8.2 \times 10^{-3}$ $\mu_h = 0.8\text{-}1.0 \times 10^{-2}$	$\sim 10^3$ $\sim 10^4$
	200 °C	ambipolar	$\mu_e = 8.4\text{-}9.0 \times 10^{-3}$ $\mu_h = 4.7\text{-}4.9 \times 10^{-3}$	$\sim 10^3$ $\sim 10^2\text{-}10^3$
	250 °C	ambipolar	$\mu_e = 1.2\text{-}1.4 \times 10^{-3}$ $\mu_h = 2.5\text{-}3.3 \times 10^{-3}$	$\sim 10^4$ $\sim 10^6$

[a] The devices were annealed in a glove box on a hotplate at the selected temperature for 15 min under nitrogen. μ_e and μ_h are electron and hole mobilities in the saturated regions in electron and hole enhancement modes, respectively. Each set of data were obtained from 3-5 OTFT devices.

2.3 Preparation and Characterization of P6-IBDF

2.3.1 Preparation of P6-IBDF

With IBDF monomer being strongly electron-deficient, a homopolymer of IBDF without any electron donating building blocks is expected to possess a low LUMO energy level and potentially be a stable n-type semiconducting polymer. An attempt was made to synthesize **P6-IBDF** by Ni(0) catalyzed Yamamoto coupling(Scheme 6). However, compound **2** decomposed during the homocoupling reaction probably due to the reaction between nickel and the lactone group in **2**. Herein **P6-IBDF** was prepared by Pd(II) catalyzed reaction of **2** with hexamethyldistannane in anhydrous toluene, and the polymer was purified by Soxhlet extraction. Only 6.4 mg of **P6-IBDF** was obtained after impurities and oligomers were dissolved by acetone and hexane. This suggested that the polymer had low molecular weight and that **P6-IBDF** exhibited excellent solubility due to the long branched side chain. It also implied the weak intermolecular interactions between polymer chains without donor-acceptor interaction. Due to the low yield of the polymerization reaction, **P6-IBDF** was only characterized by UV-Vis and CV. Device performance was also tested.

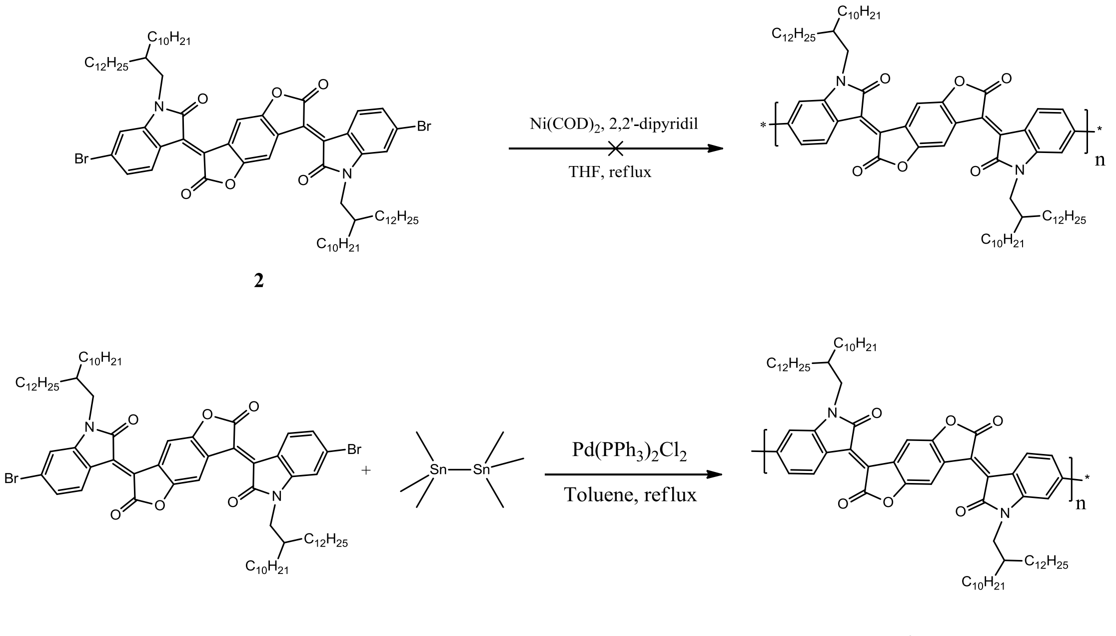

2

2

P6-IBDF

Scheme 6. Synthesis of **P6-IBDF.**

2.3.2 Characterization of P6-IBDF by UV-Vis and CV

P6-IBDF exhibited broad absorption over UV-Visible range from 350 to 900 nm (Figure 13). The chloroform solution of **P6-IBDF** showed a maximum absorption at 710 nm and an intense peak at 467 nm. In solid state, **P6-IBDF** witnessed a slight blue-shift in λ_{max} (703 nm) and a slight red-shift in onset absorption (850 nm), giving an optical bandgap of 1.46 eV. Comparing to the UV-Visible spectra of its monomer 6-Br-IBDF (Figure A-2), the absorption spectra of **P6-IBDF** is broader and showed weaker absorption in the short-wavelength, high-energy range but stronger absorption in the long-wavelength, low-energy range of the visible spectra. The onset wavelength for **P6-IBDF** film shifted ~115 nm bathochromically compare to 6-Br-IBDF film due to smaller energy bandgap and larger energy bands in the polymer as a result of extended conjugation in the polymer backbone.

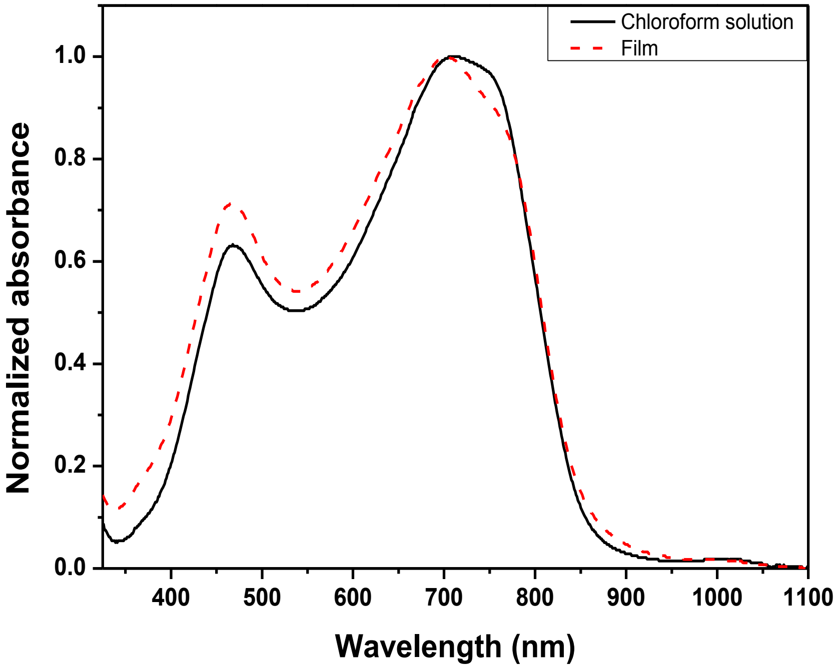

Figure 13. UV-vis-NIR absorption spectra of **P6-IBDF** in chloroform and in thin film.

The electrochemistry properties of **P6-IBDF** film were examined by CV (Figure 14). The polymer showed reproducible reduction current indicating its stability towards reduction process. The intensity of oxidation current experienced a decrease in the second scan. This is reasonable, since the repeating unit IBDF bears strong electron-withdrawing lactone and lactam groups but no strong electron-donating units. The HOMO and LUMO energy levels are calculated from the oxidation and reduction onset potential to be -5.61 and -4.18 eV, respectively, giving a bandgap of 1.42 eV, which is close to the optical bandgap estimated from absorption onset in UV-Vis. With its low lying HOMO/LUMO energy levels, **P6-IBDF** is expected to show electron transporting (n-type) characteristic.

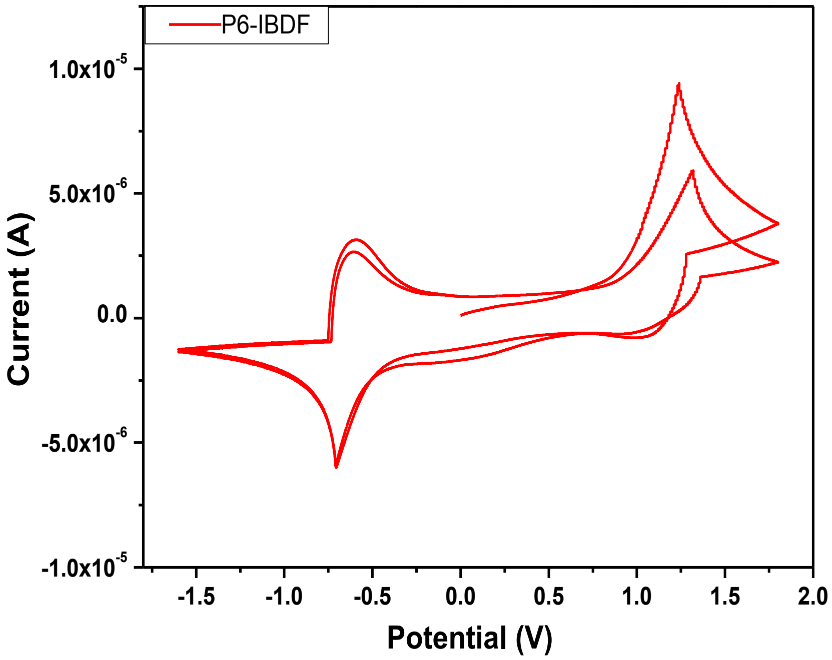

Figure 14. Cyclic voltammograms (two cycles) of a **P6-IBDF** thin film showing two oxidative and reductive cycles at a scan rate of 0.05 Vs^{-1}. The electrolyte was 0.1 M tetrabutylammonium hexafluorophosphate in anhydrous acetonitrile.

2.3.3 Device Performance of P6-IBDF

P6-IBDF was evaluated as a channel semiconductor in OTFTs using a bottom-gate, bottom-contact configuration. An n-doped conductive Si wafer was used as gate electrode. A ~300 nm-thick thermal grown SiO_2 modified with a monolayer of dodecyltrichlorosilane (DTS) was used as dielectric layer. Gold source/drain contact pairs were pre-patterned using conventional photolithography and thermal deposition. A **P6-IBDF** solution was then spin coated on top of the SiO_2 layer to form a polymer film as the channel. After the semiconducting layer was annealed at a certain temperature for 15 min in nitrogen, the devices were encapsulated with a layer of PMMA (~500 nm in thickness) and dried in vacuum oven for 30 min.

Table 2.2 Summary of OTFT device performance using **P6-IDBF** as the channel layers.[a]

Annealing temperature	Electron mobility ($cm^2V^{-1}s^{-1}$)	$I_{on/off}$	V_T (V)
100 °C	$\mu_e = 1.7 - 1.9 \times 10^{-5}$	$\sim10^3$	34
150 °C	$\mu_e = 1.9 - 2.0 \times 10^{-4}$	$\sim10^2 - 10^3$	34
200 °C	$\mu_e = 1.2 - 1.6 \times 10^{-4}$	$\sim10^2 - 10^3$	40

[a] The devices were annealed in a glove box on a hotplate at the selected temperature for 15 min under nitrogen. μ_e is electron mobilities in the saturated regions in electron enhancement modes. Each set of data were obtained from 3-5 OTFT devices.

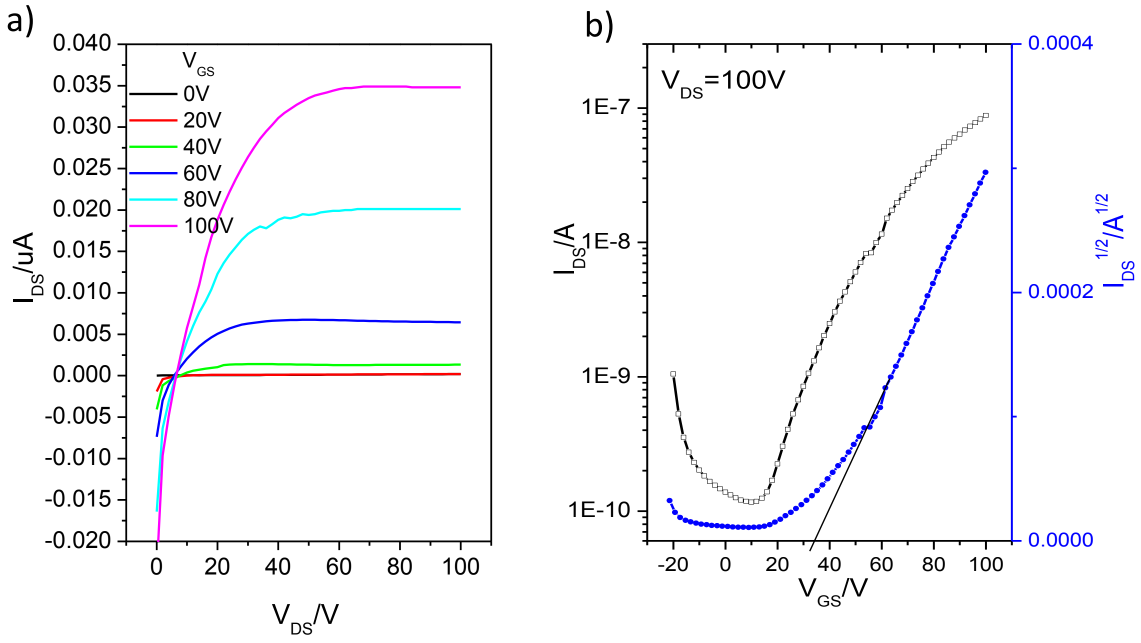

Figure 15. (a) The output and (b) the transfer curve in the electron accumiulation mode of a PMMA-encapsulated OTFT device fabricated with **P6-IBDF** thin film annealed at 150 °C. Device dimensions: channel length (*L*) = 30 μm; channel width (*W*) = 1 mm.

As expected, **P6-IBDF** showed typical electron transporting (n-type) characteristics. However, **P6-IBDF** showed poor film-forming property due to the weak interaction between polymer chains in absence of donor-acceptor interaction. As a result, the electron mobilities of **P6-IBDF** were one to two orders of magnitude lower than that of **P6-IBDF** (Table 2.2). **P6-IBDF** films annealed at 100 ^{o}C exhibited mobilities of 10^{-5} $\mathrm{cm^{2}V^{-1}s^{-1.}}$ Annealing the polymer thin film at higher temperature (150 and 200 ^{o}C) increased electron mobility by ten times while maintaining similar current on-and-off ratio. The highest electron mobility of 2.0×10^{-4} $\mathrm{cm^{2}V^{-1}s^{-1}}$ was recorded at V_{DS} = 100 V for device fabricated with 150 ^{o}C-annealed **P6-IBDF** film. Further increase in annealing temperature to 200 ^{o}C led to a slight decrease in mobility and an increase in threshold voltage (V_T = 40 V). The low mobilities were attributed to low molecular weight of the polymer as well as weak intermolecular interaction. Insufficient amount of polymer is available to fabricate devices without PMMA encapsulation due to the low yield of the homocoupling reaction.

2.4 Effect of Degree of Conjugation on Charge Transport of PIBDF-Ts

2.4.1 Conjugation effects

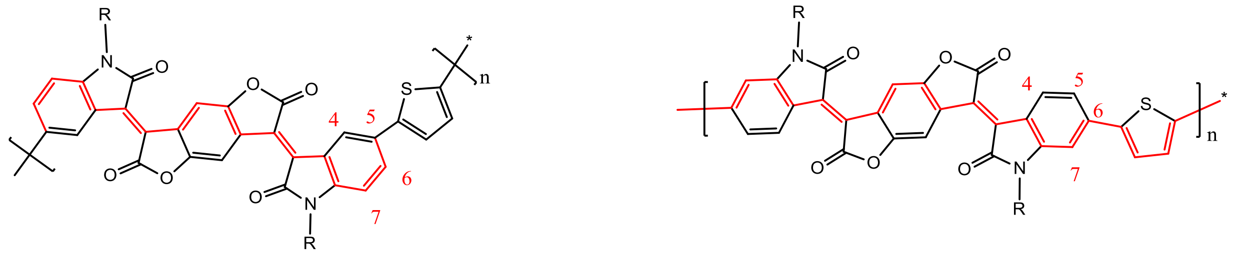

P5-IBDF-T **P6-IBDF-T**

Scheme 7. Comparison of conjugation in **P5-IBDF-T** and **P6-IBDF-T.**

Since charge transport along the polymer chain is realized by delocalization of charge carriers, a high degree of conjugation and coplanarity of the main backbone is crucial for polymer semiconductors. In order to attain the coplanarity of the in **PIBDF-T** polymer backbone, thiophene units should be attached to the 5- or 6-position of IBDF to avoid steric effects (Scheme 7). When comparing these two structures, alternatively arrange single and double bonds contributing to a higher degree of conjugation can be achieved in **P6-IBDF-T**. This arrangement, however, is not possible in **P5-IBDF-T**, where T is at the 5-position. It was also noted that **P6-**

IBDF-T has a more linear structure than **P5-IBDF-T**, which is beneficial for the formation of long range crystalline domain.

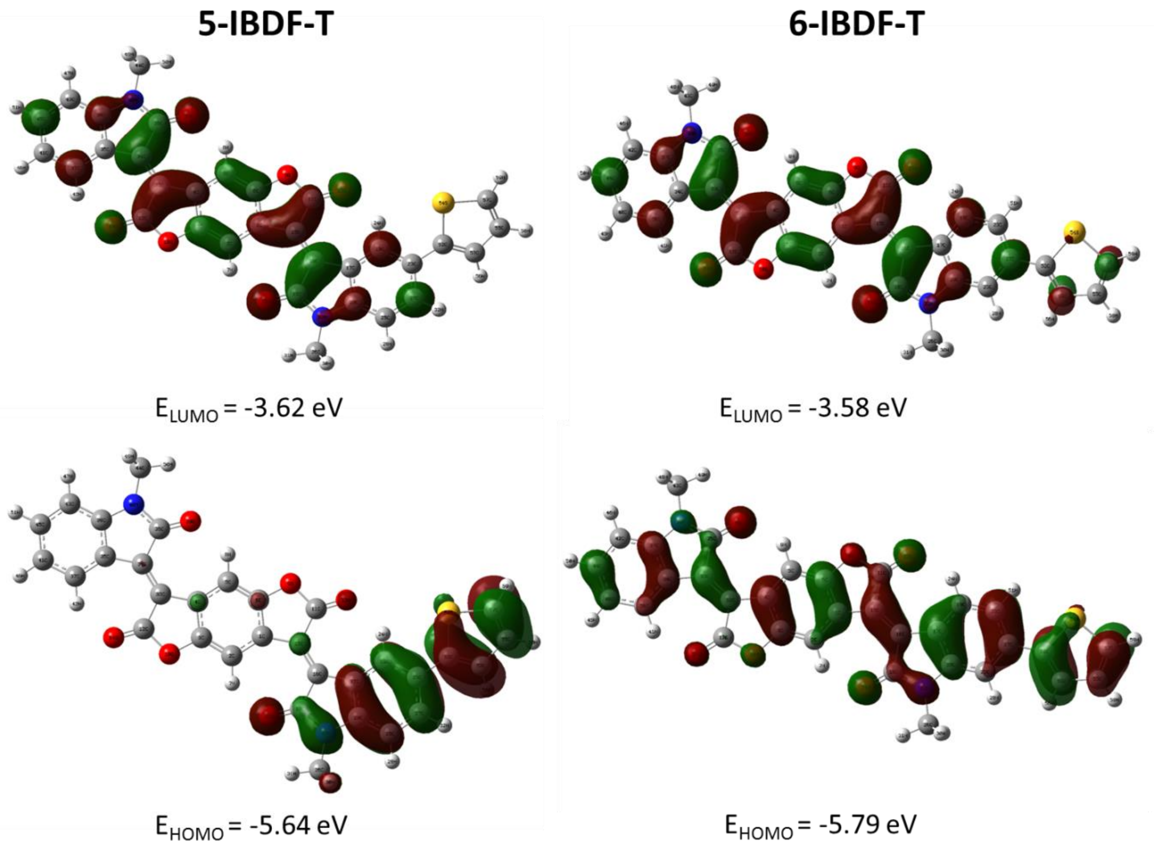

Figure 16. HOMO/LUMO orbitals of 5-IBDF-T and 6-IBDF-T and the calculated HOMO/LUMO energy levels with respect to vacuum (0 eV)**.**

In order to demonstrate the difference between **P5-IBDF-T** and **P6-IBDF-T** in terms of degree of conjugation, geometry optimizations were performed on the repeating units of these two polymers, 5-IBDF-T and 6-IBDF-T. The orbital surfaces of HOMO/LUMOs of both molecules were generated to visualize the electron distribution on the molecular orbitals (Figure 16). It is clearly shown in Figure 16 that electrons are evenly distributed over the whole molecule in the HOMO of 6-IBDF-T, while in the LUMO of 6-IBDF-T electrons distributes over IBDF and T moieties with higher electron density at IBDF building block. In contrast, localized electron distribution at T and the adjacent isatin moieties are observed in the HOMO of 5-IBDF-T;

meanwhile, electrons in LUMO are localized on IBDF moiety and no electron density was observed at T. These indicated that 6-IBDF-T has higher degree of conjugation than 5-IBDF-T to facilitate even electron distribution over the whole molecule. Another evidence of the low degree of conjugation in **P5-IBDF-T** is the large dihedral angle of ~25^{o} observed in the optimized structure of 5-IBDF-T. It was also noted that 6-IBDF-T has a more linear structure compared to 5-IBDF-T.

2.4.2 Preparation of 5-IBDF monomer and P5-IBDF-T

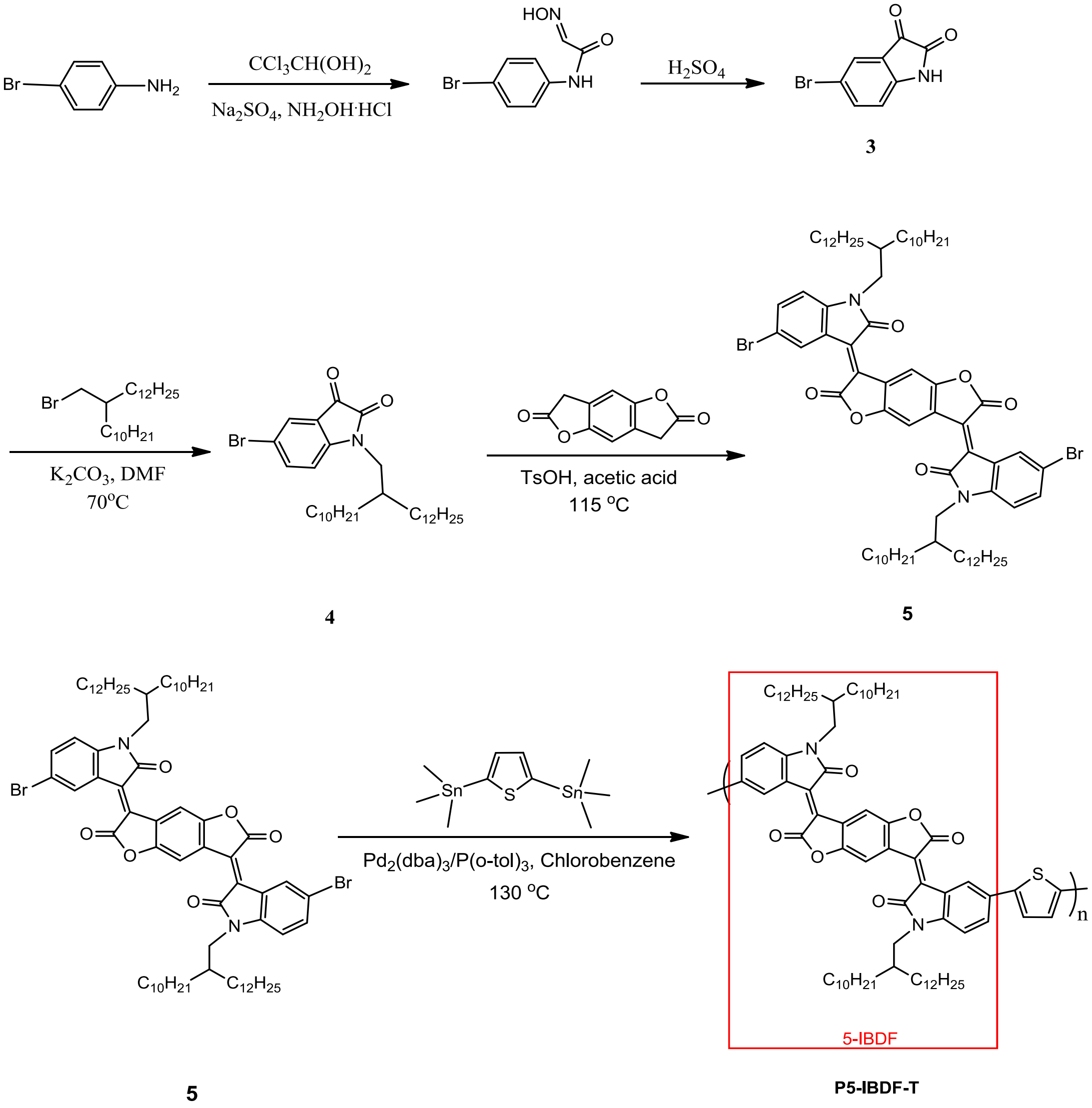

Scheme 8. Synthesis of dibrominated 5-IBDF monomer and **P5-IBDF-T**.

The preparation of dibromo functionalized 5-IBDF monomer and **P5-IBDF-T** are outlined in Scheme 8. 5-bromoindoline-2,3-dione (**3**) was prepared from 4-bromoaniline according to established route.[67–69] *N*-alkylation of **3** was accomplished in anhydrous DMF catalyzed by potassium carbonate in 55 % yield. Compound **4** was then reacted with benzo[1,2-*b*:4,5-*b*']difuran-2,6(3*H*,7*H*)-dione to afford the dibromo functionalized 5-IBDF monomer (**5**). **P5-IBDF-T** was prepared via Stille-coupling of **5** with 2,5-bis(trimethylstannyl) thiophene, and purified through Soxhlet extraction. After impurities and oligomers were removed using acetone and hexane, the polymer was dissolved in chloroform. Chlorobenzene was also used as the extracting solvent after chloroform fraction; however, a negligible amount of polymer with higher molecular weight was extracted in chlorobenzene. This suggested that **P5-IBDF-T** has better solubility than **P6-IBDF-T**, which is due to the weaker intermolecular interaction origin from the more zigzagged polymer backbone. The number average (M_n) and weight average molecular weight (M_w) was determined to be 24,600 and 70,600, respectively, using HT-GPC at a column temperature of 140 ^{o}C with 1,2,4-trichlorobenzene as eluent and polystyrene as standards.

2.4.3 Characterization of P5-IBDF-T by TGA, DSC, UV-Vis, and CV

P5-IBDF-T was analyzed by DSC and TGA to characterize crystallinity and thermal behaviour. The DSC curve for the polymer showed neither obvious exothermic nor endothermic signals (Figure 17), implying the absence of crystalline domain in **P5-IBDF-T**. TGA analysis showed that **P5-IBDF-T** has similar thermal stability as **P6-IBDF-T,** with a 5% weight loss recorded at 382 ^{o}C (Figure 18).

The UV-Vis-NIR absorbance spectra of **P5-IBDF-T** are shown in Figure 19. **P5-IBDF-T** in tetrachloroethane exhibited a maximum absorption ($\lambda_{\max}$) at 375 nm, with two less intense absorption peaks at 457 and 557 nm with decreasing intensity. The solid film of **P5-IBDF-T** showed a maximum absorption and the second intense absorption at the same wavelength and a redshift of 10 nm in the third intense peak (567 nm). The onset absorption of the solid state **P5-IBDF-T** is 978 nm, giving a bandgap of ~1.27 eV. This bandgap is smaller than the value measured for **P6-IBDF-T** (~1.36 eV). This observation is against the theory that higher degree of conjugation give rise to smaller energy bandgap. The contradiction between the theory and the experimental observation can be explained with the assistance of the computer simulation of 5-IBDF-T and 6-IBDFT. Due to the strong electron-deficiency of IBDF building block, the LUMO energy levels of both 5-IBDF-T and 6-IBDF-T are close to the predicted LUMO energy level of IBDF-Me. However, a difference of ~0.15 eV was found between the predicted HOMO energy levels. Because of the lower degree of conjugation in 5-IBDF-T, the HOMO of 5-IBDF-T is more localized on thiophene moiety, so that thiophene has stronger influence on the HOMO energy level of the molecule. This results in a higher HOMO energy level, thus a smaller bandgap.

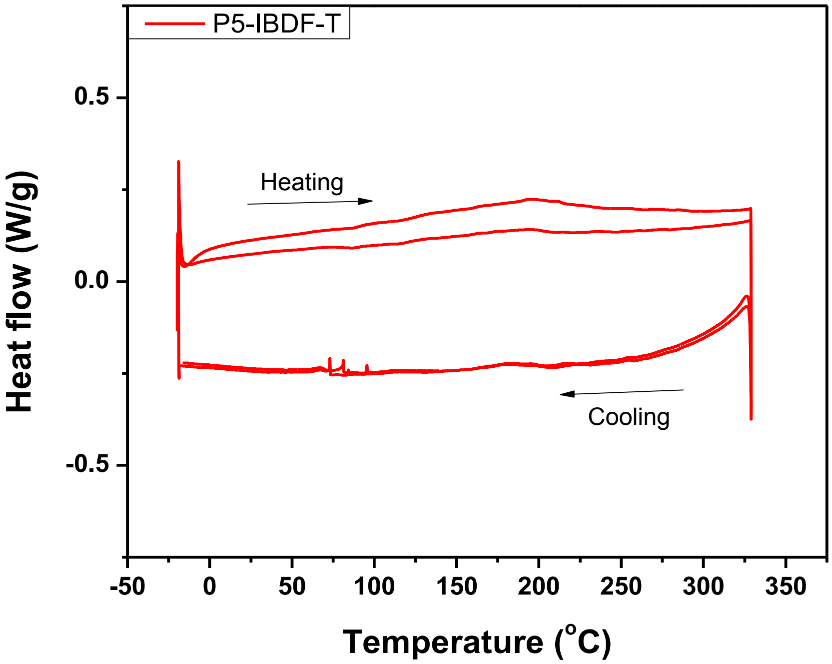

Figure 17. Differential scanning calorimetry (DSC) profiles of **P5-IBDF-T** obtained at a scanning rate of 10 ℃ min^{-1} under nitrogen

Future evidence for the low degree of conjugation in **P5-IBDF-T** is the weak absorption of light over the visible-NIR region, which can be explained by the uneven electron distribution in HOMO/LUMO of **P5-IBDF-T** as illustrated in Figure 20. When the polymer absorbed light of a certain wavelength, electrons on HOMO were excited to LUMO. Since the overlap between HOMO and LUMO is limited, only electrons in the overlapping area can easily jump to LUMO.

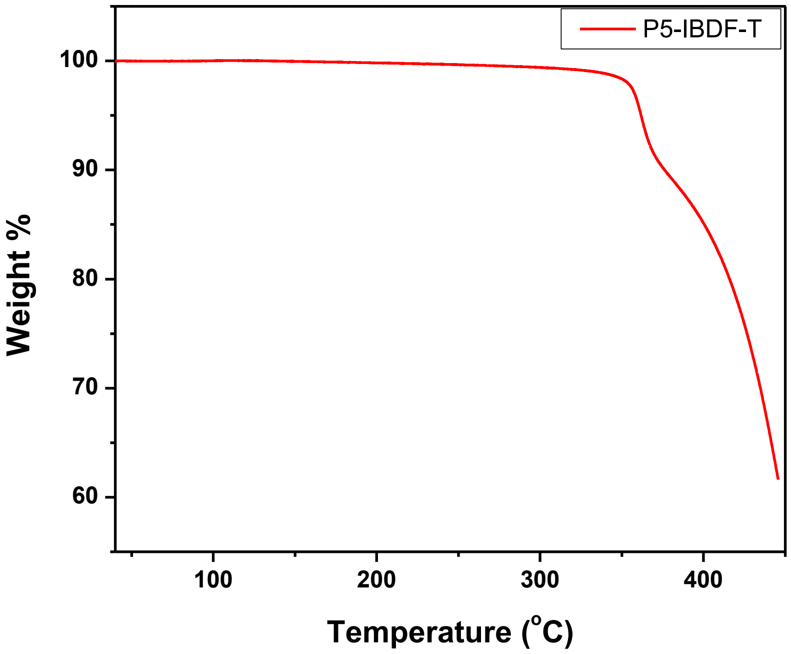

Figure 18. TGA curve of **P5-IDBF-T** measured with a heating rate of 10 ℃·min^{-1} under N_2.

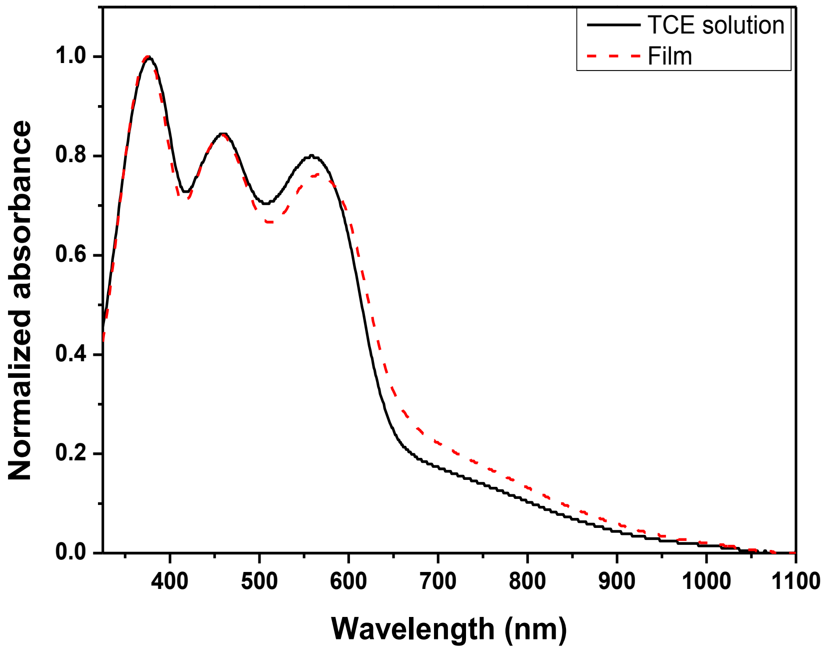

Figure 19. UV-Vis-NIR absorption spectra of **P5-IBDF-T** in tetrachloroethane (TCE) and in thin film.

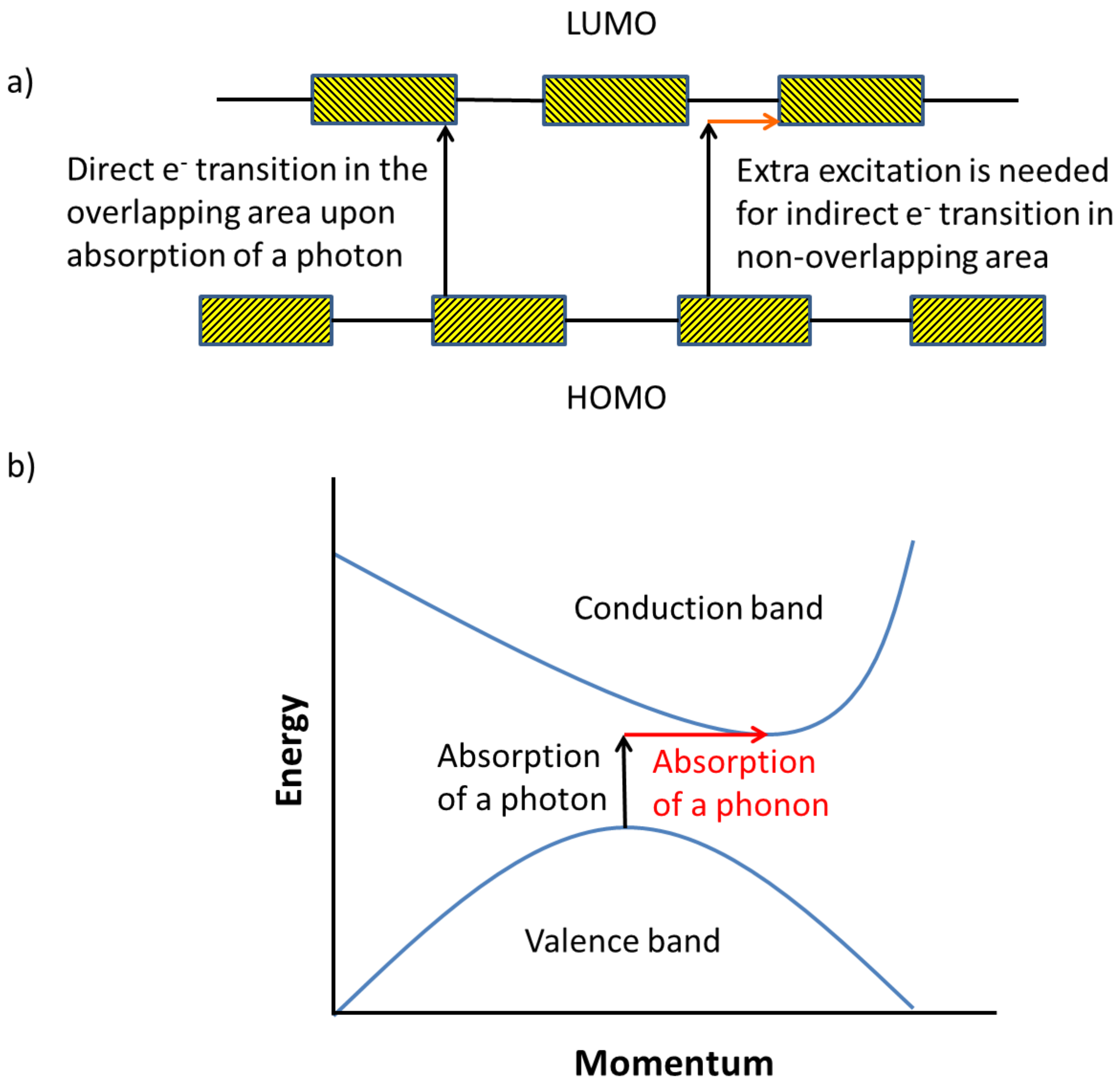

Figure 20. (a) Schematic diagram of electron transition from HOMO to LUMO in **P5-IBDF-T** and (b) schematic diagram of electron transition in indirect bandgap in silicon.

On the other hand, electrons in the non-overlapping area cannot reach LUMO with energy absorbed only from a photon. By analogy to the indirect bandgap in inorganic semiconductor silicon, where absorption or emission of a phonon is involved in the electron transition between the conduction and valance bands,[70–72] an external excitation is necessary to ease the electron transition from HOMO to LUMO in **P5-IBDF-T**. Therefore, even though **P5-IBDF-T** showed longer onset wavelength, thus smaller bandgap than **P6-IBDF-T**, the major absorption of radiation by **P5-IBDF-T** is in the shorter wavelength (higher radiation energy) UV-visible region, and the absorption over the long wavelength (lower radiation energy) visible-NIR range is relatively weak.

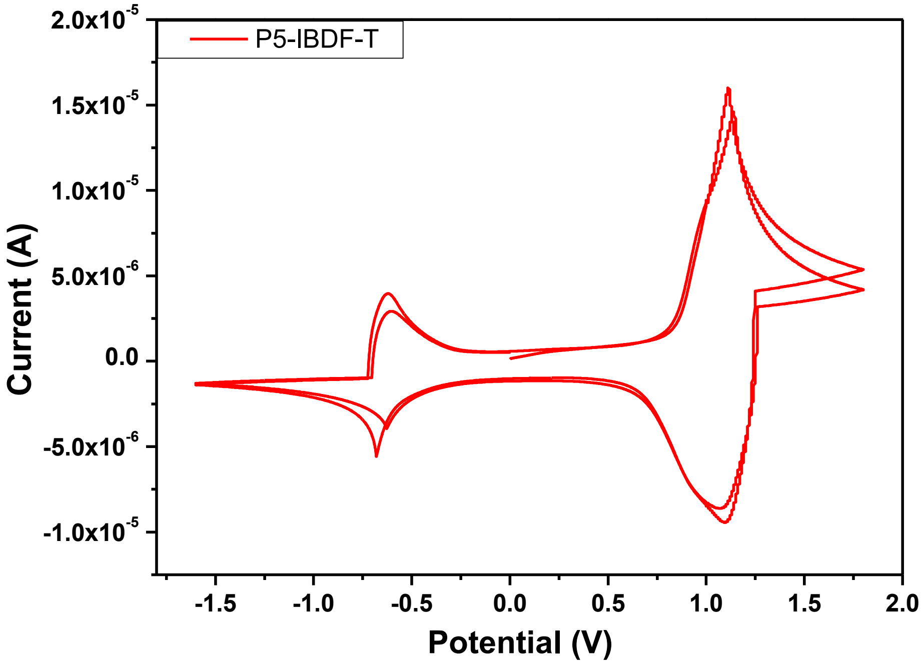

Figure 21. Cyclic voltammogram (two cycles) of a **P5-IBDF-T** thin film showing two oxidative and reductive cycles at a scan rate of 0.05 Vs^{-1}. The electrolyte was 0.1 M tetrabutylammonium hexafluorophosphate in anhydrous acetonitrile.

Similar to **P6-IBDF-T**, **P5-IBDF-T** showed reversible and reproducible redox cycles (Figure 21), suggesting that this polymer is stable toward both oxidation and reduction process. Oxidation current observed in the cyclic voltammogram was stronger than the reduction current. This indicates that **P5-IBDF-T** is potentially hole transporting semiconductor than electron transport. The HOMO/LUMO energy levels are -5.52 and -4.11 eV, respectively, calculated from oxidation and reduction onset potentials. The LUMO level estimated from the HOMO level obtained from the CV and the optical band gap is -4.25 eV.

2.4.4 Device Performance of P5-IBDF-T

The same device configuration as used in characterization of **P6-IBDF-T** was used to evaluate **P5-IBDF-T** as a channel semiconductor. The device was fabricated on an n-doped conductive Si wafer substrate. A ~200 nm thermal grown SiO_2 layer was modified with a monolayer of dodecyltrichlorosilane (DTS) and used as dielectric. A **P5-IBDF-T** solution was then spin coated on top of the SiO_2 layer to form the channel after gold source/drain contacts were thermal deposited. After the semiconducting layer was annealed at a 100, 150 and 200 ^{o}C for 15 min in nitrogen, the devices were encapsulated with a layer of PMMA (~500 nm in thickness) and tested outside the glove box.

Table 2.3 Summary of OTFT device performance using **P5-IDBF-T** as the channel layers.

Annealing temperature	Mobility ($cm^2V^{-1}s^{-1}$)	$I_{on/off}$
100 °C	$\mu_e = 0.8\text{-}1.1 \times 10^{-5}$ $\mu_h = 0.5\text{-}2.3 \times 10^{-5}$	~10^2 ~10^2
150 °C	$\mu_e = 0.9\text{-}1.6 \times 10^{-5}$ $\mu_h = 1.0\text{-}2.0 \times 10^{-5}$	~10^4 ~10^5
200 °C	$\mu_e = 1.7\text{-}2.4 \times 10^{-5}$ $\mu_h = 0.7\text{-}7.2 \times 10^{-5}$	~10^4 ~10^4

[a] The devices were annealed in a glove box on a hotplate at the selected temperature for 15 min under nitrogen. μ_e and μ_h are electron and hole mobilities in the saturated regions in electron and hole enhancement modes, respectively. Each set of data were obtained from 3-5 OTFT devices.

The device performance of **P5-IBDF-T** was summarized in Table 2.3. **P5-IBDT-T** showed both hole and electron transport in PMMA encapsulated OTFTs; however, the mobilities were two to three orders of magnitude lower than those recorded for P6-IBDF-T. All the mobilities recorded were in the magnitude of 10^{-6} to 10^{-5} $cm^2V^{-1}s^{-1}$ with the highest hole/electron mobilities of $2.4 \times 10^{-5}/7.2 \times 10^{-5}$ $cm^2V^{-1}s^{-1}$ ($I_{on/off}$ = ~10^4) recorded for an OTFT with a 200 ^{o}C-annealed polymer thin film as the channel (Figure 22 and Figure 23). The mobilities were observed to increase as annealing temperature increase from 100 to 200 ^{o}C. The low mobilities of **P5-IBDF-T** compared to **P6-IBDF-T** were attributed to discontinuous electron distribution in HOMO/

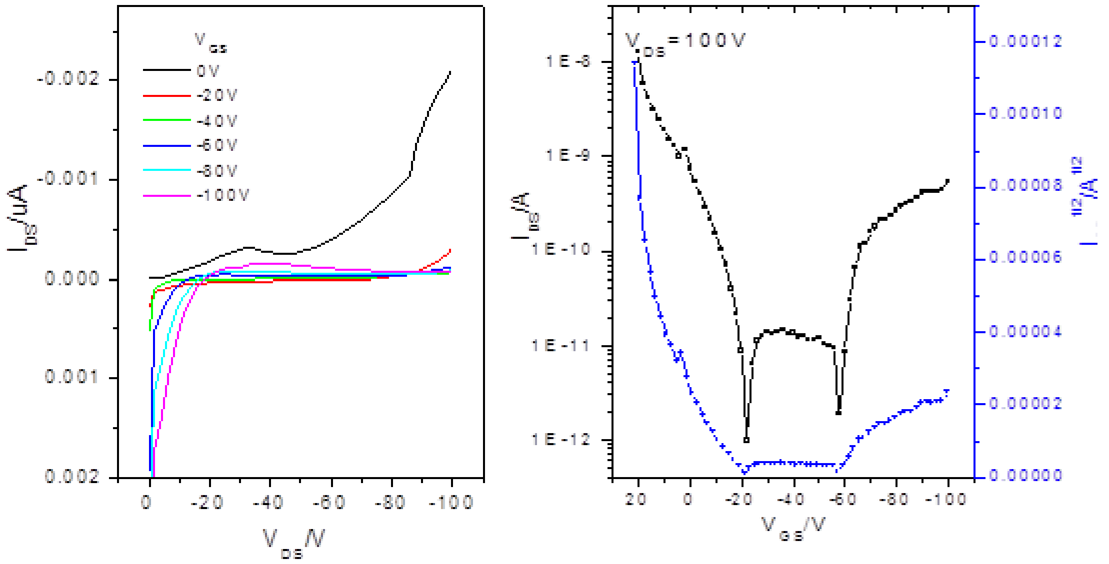

Figure 22. Output (left) and transfer (right) characteristics in the hole enhancement mode of an encapsulated OTFT device with a **P5-IBDF-T** film annealed at 200 °C for 15 min. Device dimensions: channel length (*L*) = 30 μm; channel width (*W*) = 1 mm.

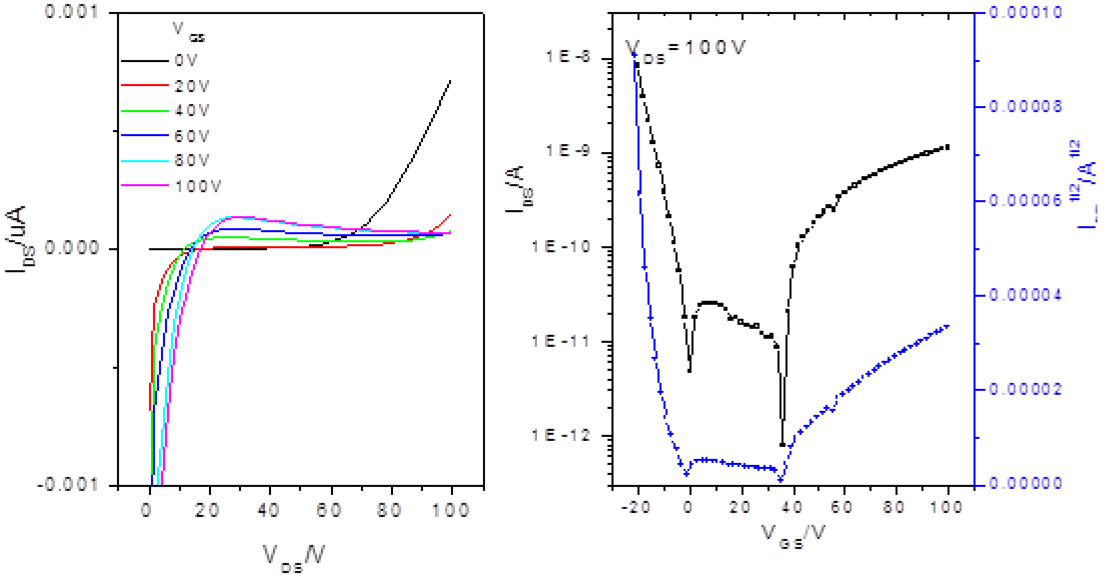

Figure 23. Output (left) and transfer (right) characteristics in the electron enhancement mode of an encapsulated OTFT device with a **P5-IBDF-T** film annealed at 100 °C for 15 min. Device dimensions: channel length (*L*) = 30 μm; channel width (*W*) = 1 mm.

LUMO arising from the low degree of conjugation and the large torsion angle between IBDF acceptor and T donor due to steric effect in **P5-IBDF-T**. These inhibited delocalization of charge carriers and thus weakened the dominant charge transport property in polymer semiconductors.

2.5 Experimental Section

2.5.1 General

All chemicals were purchased from Sigma-Aldrich and used without further purification. Benzo[1,2-b:4,5-b']difuran-2,6(3H,7H)-dione[58,59] and 5-bromoindoline-2,3-dione[67–69] were synthesized according to the literature methods.

Geometry optimization of 2,5-dihydro-2,5-dimethyl-3,6-di-2-thienyl-pyrrolo[3,4-***c***]pyrrole-1,4-dione (DBT-Me), (*E*)-3-(1,2-dihydro-1-methyl-2-oxo-3*H*-indol-3-ylidene)-1,3-dihydro-1-methyl-2*H*-indol-2-one (IID-Me), (3*E*,7*E*)-3,7-bis(1-methyl-2-oxoindolin-3-ylidene)benzo[1,2-*b*:4,5-*b*']difuran-2,6(3*H*,7*H*)-dione (IBDF-Me), (3E,7E)-3-(1-methyl-2-oxo-5-(thiophen-2-yl)indolin-3-ylidene)-7-(1-methyl-2-oxoindolin-3-ylidene)benzo[1,2-b:4,5-b']difuran-2,6(3H,7H)-dione (5-IBDF-T) and (3E,7E) -3-(1-methyl-2-oxo-6-(thiophen-2-yl)indolin-3-ylidene)-7-(1-methyl-2-oxoindolin-3-ylidene)benzo[1, 2-b:4,5-b']difuran-2,6(3H,7H)-dione (6-IBDF-T) were performed with density functional theory (DFT) calculation using the B3LYP hybrid functional[73,74] with the 6-31G basis set. Molecular orbital shapes and energies discussed in the text are those calculated at the optimized structures. Orbital pictures were prepared with GaussView 5.0 software.[75] All calculations were performed with Gaussian 09 package[76,77] on the Shared Hierarchical Academic Research Computer Network (SHARCNET) of Canada.

^{1}H NMR data were collected on a Bruker DPX 300 MHz spectrometer with chemical shift relative to tetramethylsilane (TMS, 0 ppm). UV-Visible spectra were recorded on a Thermo Scientific model GENESYS™ 10S VIS Spectrophotometer. Thermal gravimetric analysis (TGA) was carried out using a TGA Q500 (TA Instruments) at a heating rate of 10 ℃ min^{-1} under nitrogen. Cyclic voltammograms were obtained with a Digi-Ivy model DY2111 Potentiostat using an Ag/AgCl reference electrode, a platinum foil counter electrode and a platinum disk working electrode. The polymer film was coated on the working electrode by drop-casting a polymer solution. CV measurements were collected in 0.1 M tetrabutylammonium hexafluorophosphate in dry acetonitrile using ferrocene/ferrocenium (Fc/Fc+) couple as a standard at a scan rate of 50 mV s^{-1}. The HOMO energy levels were calculated using the equation $E_{HOMO} = -\left(E_{ox} - E_{Fc/Fc^+}\right) - 4.80$ eV, where E_{ox} and E_{Fc/Fc^+} are the onset oxidation potentials for the polymer sample and ferrocene against the Ag/AgCl reference electrode, and -4.80 eV is the HOMO energy level of ferrocene with respect to the vacuum level (0 eV).[78–80] XRD measurement are carried out with a Bruker D8 Advance powder diffractometer with Cu Kα radiation (λ = 1.5406 Å) using standard Bragg-Brentano geometry. Gel permeation chromatography (GPC) measurements were performed on on a Malvern 350 HT-GPC system using 1,2,4-trichlorobenzene as an eluent and polystyrene as standards at a column temperature of 140°C. AFM images were performed on polymer thin films on DTS-modified SiO_2/Si substrate using a Dimension 3100 Scanning Probe Microscope.

2.5.2 Fabrication and Characterization of OTFT devices

A bottom-contact, bottom-gate OTFT configuration was used. Heavily doped Si wafer functions as the gate electrode and a thermally grown SiO_2 layer (~200-300 nm) with a capacitance of ∼17 nF/cm^2 on top of the Si layer was used as the insulating dielectric. Au source and drain electrode pairs were pre-deposited on the SiO_2 layer with photolithography method. The substrate was cleaned with DI water, acetone, and isopropanol in an ultrasonic bath, followed by O_2 plasma. Subsequently, the substrate was immersed in a dodecyltrichlorosilane (DTS) solution in toluene (10 mg/mL) at 70 ℃ for 20 min. After washing with toluene, substrate was dried under a nitrogen flow. A polymer solution in chloroform (10 mg/mL) was spin coated on the substrate at 3000 rpm for 60 s to give a film, which was subjected to thermal annealing at different temperatures for 15 min in a glove box. After annealing, the devices were encapsulated with a 500 nm-thick PMMA (M_W = 120,000) by spin coating a PMMA solution in butyl acetate (8 wt %) at 3000rpm for 50 s, and dried at 80 ℃ for 30min. OTFT devices have a channel length (L) of 30 μm with a channel width (W) of 1000 μm. The devices were characterized in air using an Agilent 4155C Semiconductor Analyzer. The carrier mobility in the saturated regime, μ_{sat}, was calculated according to the equation of $I_{DS} = C_i \mu_{sat} (W/2L)(V_G - V_T)^2$, where I_{DS} is the drain current, C_i is the capacitance per unit area of the gate dielectric, W and L are, respectively, the semiconductor channel width and length, and V_{GS} and V_T are, respectively, the gate voltage and threshold voltage. V_T of the devices was determine from extrapolation of the linear fit of the $(I_{DS})^{1/2}$ versus V_{GS} curve in the saturation regime at $I_{DS} = 0$.

2.5.3 Synthetic Procedures

Synthesis of 6-bromo-1-(2-decyltetradecyl)indoline-2,3-dione (1): To a mixture of 6-bromoindoline-2,3-dione (1.5 g, 6.64 mmol, 1.0 equiv.), K_2CO_3 (3.6 g, 26.05 mmol, 3.92 equiv.) and anhydrous DMF (18 mL) were in a 50 mL two-necked round bottom flask, 11-(bromomethyl)tricosane (4.16 g, 9.95 mmol, 1.15 equiv.) was added. The reaction mixture was heated with stirring at 70 °C under argon for 20 h. Solvent was then evaporated under a reduced pressure and 50 mL water was added. The mixture was extracted with dichloromethane (3 × 50 mL) and the organics were combined, dried over Na_2SO_4, and concentrated under a reduced pressure. The residue was purified by column chromatography on silica gel (dichloromethane:hexane 2:1) to yield 2.46 g (66 %) of 6-bromo-1-(2-decyltetradecyl)indoline-2,3-dione as an orange liquid. ^{1}H NMR (300 MHz, $CDCl_3$): δ 7.46 (d, J= 7.95 Hz, 1H), 7.26 (d, J= 7.74 Hz, 1H), 7.01 (s, 1H), 3.56 (d, J= 7.44 Hz, 2H), 1.81 (br, 1H), 1.15-1.40 (m, 40H), 0.84-0.89 (m, 6H).

Synthesis of (3*E*,7*E*)-3,7-bis(6-bromo-1-(2-decyltetradecyl)-2-oxoindolin-3-ylidene)benzo [1,2-*b*:4,5-*b*']difuran-2,6(3*H*,7*H*)-dione (2): This compound was prepared following a similar procedure described for (3*E*,7*E*)-3,7-bis(2-oxoindolin-3-ylidene)benzo[1,2-*b*:4,5-*b*']difuran-2,6(3*H*,7*H*)-dione.[6] Benzo[1,2-*b*:4,5-*b*']difuran-2,6(3*H*,7*H*)-dione (0.285 g, 1.50 mmol, 1.0 equiv.), 6-bromo-1-(2-decyltetradecyl)indoline-2,3-dione (1.69 g, 3.00 mmol, 2.0 equiv.), and toluenesulfonic acid (TsOH) (0.08 g, 0.42 mmol, 0.28 equiv.) were stirred in acetic acid (15 mL) at 115 °C under argon for 17 h. The reaction mixture was then cooled to room temperature and filtered. The solid was washed with acetic acid and then methanol. The dark purple solid obtained was purified through column chromatography on silica gel (dichloromethane: hexane 1:1, v:v) to yield 1.33 g (69 %) of compound **2** as a deep blue solid. ^{1}H NMR (300 MHz,

$CDCl_3$): δ 9.06 (s, 2H), 8.91 (d, J= 8.67 Hz, 2H), 7.18 (d, J= 8.68 Hz, 2H), 6.88 (s, 2H), 3.61 (d, J= Hz, 4H), 1.87 (m, 2H), 1.14-1.45 (m, 80H), 0.82-0.88 (m, 12H).

Synthesis of 5-bromo-1-(2-decyltetradecyl)indoline-2,3-dione (4): This compound was prepared from 5-bromoindoline-2,3-dione following the procedure described above for the preparation of compound **1**. Yield: 2.458 g (55% yield); ^1H NMR (300 MHz, $CDCl_3$) δ 7.70 – 7.63 (m, 2H), 6.75 (d, *J* = 8.2 Hz, 1H), 3.56 (d, *J* = 7.4 Hz, 2H), 1.80 (m, 1H), 1.22 (s, 40H), 0.86 (t, *J* = 6.6 Hz, 6H).

Synthesis of (3E,7E)-3,7-bis(5-bromo-1-(2-decyltetradecyl)-2-oxoindolin-3-ylidene)benzo[1,2-b:4,5-b']difuran-2,6(3H,7H)-dione (5): This compound was prepared from benzo[1,2-*b*:4,5-*b*']difuran-2,6(3*H*,7*H*)-dione and compound **4** following the same procedure described above for the preparation of compound **2**. Yield: 1.4992 g (74 % yield); ^1H NMR (300 MHz, $CDCl_3$) δ 9.18 (s, 2H), 9.09 (s, 2H), 7.45 (d, *J* = 8.2 Hz, 2H), 6.62 (d, *J* = 7.2 Hz, 2H), 3.63 (d, *J* = 6.3 Hz, 4H), 1.83 (s, 2H), 1.25 (m, 80H), 0.84 (s, 12H).

Synthesis of P6-IBDF-T: A 100-mL dry two-neck round bottom flask equipped with a water condenser was charged with compound **2** (0.29 g, 0.227 mmol, 1.0 equiv.), 2,5-bis(trimethylstannyl)thiophene (0.093 g, 0.22 mmol, 1.0 equiv.) and tri(o-tolyl)phosphine (P(o-tol)$_3$) (0.006 g, 0.01816 mmol, 0.08 equiv.). Anhydrous chlorobenzene (9 mL) was injected through a septum, and a solution of tris(dibenzylideneacetone)dipalladium ($Pd_2(dba)_3$) (3.6 mg, 0.0045 mmol, 0.02 equiv.) in 1 mL of chlorobenzene was added with a syringe. The reaction mixture was then heated at 130 ^oC under argon atmosphere for 60 h. Bromobenzene (0.5 mL) was added to react with the residual trimethylstannyl end group. After cooling down to room temperature, the reaction mixture was poured into stirring acetone (150 mL). The solid was collected by filtration, washed with acetone, dried and further purified through Soxhlet extraction using acetone, hexane and chloroform to remove oligomers and other impurities. The remaining polymer was dissolved in chlorobenzene. A black film was obtained upon removal of the solvent. Yield: 0.0930 g (34 %). M_w/M_n (GPC) = 50,100 / 34,200. Found: C, 78.2; H, 9.5; N, 2.6. Calc. for C78H108N2O6S: C, 78.0; H, 9.1; N, 2.3.

Synthesis of P6-IBDF-BT: This polymer was synthesized following a similar procedure described for **P6-IDBF-T** using compound **2** (0.3 g, 0.23 mmol, 1.0 equiv.) and 5,5'-bis(trimethylstannyl)-2,2'-bithiophene (0.115 g, 0.23 mmol, 1.0 equiv.) as monomers. The solid product was purified through Soxhlet extraction using acetone, hexane, and chloroform to remove impurities and oligomers. Extraction with tetrachloroethane or chlorobenzene could not dissolve the remaining polymer. Yield of the insoluble fraction: 0.269 g (91 %). Found: C, 76.2; H, 9.0; N, 2.4. Calc. for C82H110N2O6S2: C, 76.7; H, 8.6; N, 2.2.

Synthesis of P6-IBDF: A well-dried 50 mL two-necked round bottom flask was charged with compound **2** (0.1 g, 0.0782 mmol, 1 equiv.) and hexamethylditin (0.027 g, 0.0821 mmol, 1.05 equiv.). The vessel was vacuumed and refilled with argon, after which anhydrous toluene (7 mL) was injected through a septum. $Pd(PPh_3)_2Cl_2$ (0.003 g, 0.0039 mmol, 0.05 equiv.) was then added. The mixture was refluxed for 48 h under Ar. The mixture was then poured into 150 mL acetone and filtered. The collected polymer was purified through Soxhlet extraction using acetone and hexane and then dissolved in chloroform. Yield: 6.4 mg (7%).

Synthesis of P5-IBDF-T: This polymer was synthesized following a similar procedure described for **P6-IDBF-T** using compound **5** (0.3 g, 0.23 mmol, 1.0 equiv.) and 2,5-bis(trimethylstannyl)thiophene (0.115 g, 0.23 mmol, 1.0 equiv.) as monomers. The solid was purified through Soxhlet extraction using acetone and hexane to remove impurities and oligomers, and then dissolved in chloroform. Yield: 0.2491 g (83 %). M_w/M_n (GPC) = 70,600 / 24,600

Chaptor 3

DTA Based Donor-Acceptor Copolymer for OTFTs

3.1 Novel (*E*)-1,2-di(thiazol-2-yl)diazene (DTA) Monomer for Constructing Donor-Acceptor Copolymers

3.1.1 Molecular Design

Azo-compounds are commonly used as dyes, and they have been considered as promising candidates for optical data storage.[81] Recently, azobenzene derivatives have been reported to be used as charge carrier trap in pentacene-based thin film transistors to induce electric bistability.[82] However, semiconducting polymers with azo moieties in the backbone has never been reported. In this study, we combined azo group with thiazole moiety and prepared (*E*)-1,2-di(thiazol-2-yl)diazene (DTA) (Scheme 9) as the novel electron donating building block for D-A polymers.

The study of DTA-based copolymer started from computer simulation on a simple DTA molecule, (E)-1,2-bis(4-methylthiazol-2-yl)diazene (DTA-Me) with a methyl group at 4-position, to study the geometry, electron distribution and energy levels of the DTA building block. The modeling results demonstrated that the geometry of DTA molecule takes a highly coplanar geometry with a dihedral angle of 180^{o} between the two thiazole rings, which is crucial for forming closely packed π-π stack.

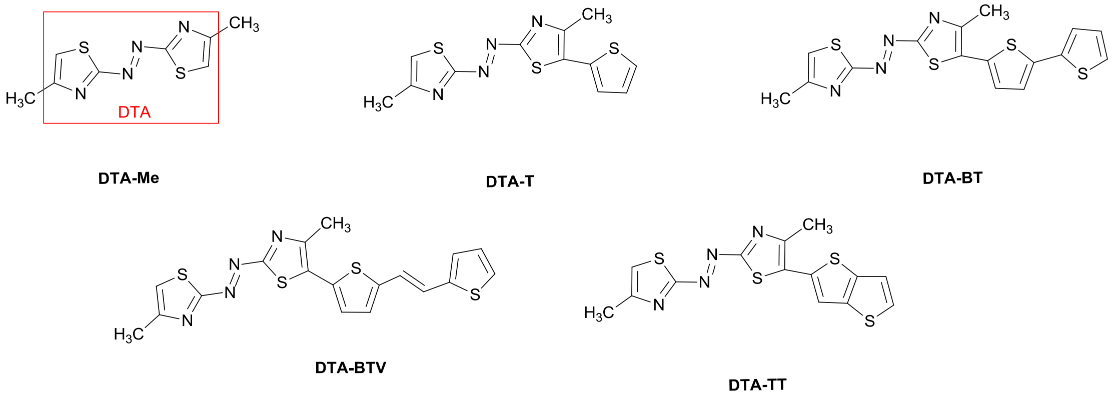

Scheme 9. Structure of DTA-Me, DTA-BTV, DTA-T, DTA-BT and DTA-TT.

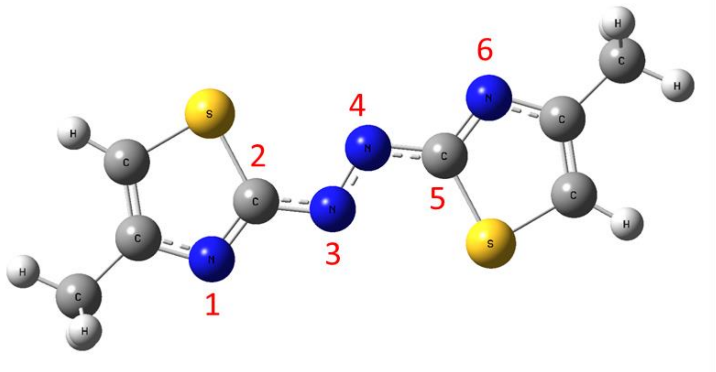

N1-C2-N3-N4	179.950
C2-N3-N4-C5	179.996
N6-C5-N4-N3	179.955
N1-C2-C5-N6	179.993

Figure 24. Optimized structure of (E)-1,2-di(thiazol-2-yl)diazene (DTA-Me) and some dihedral angle values obtained by computer simulation.

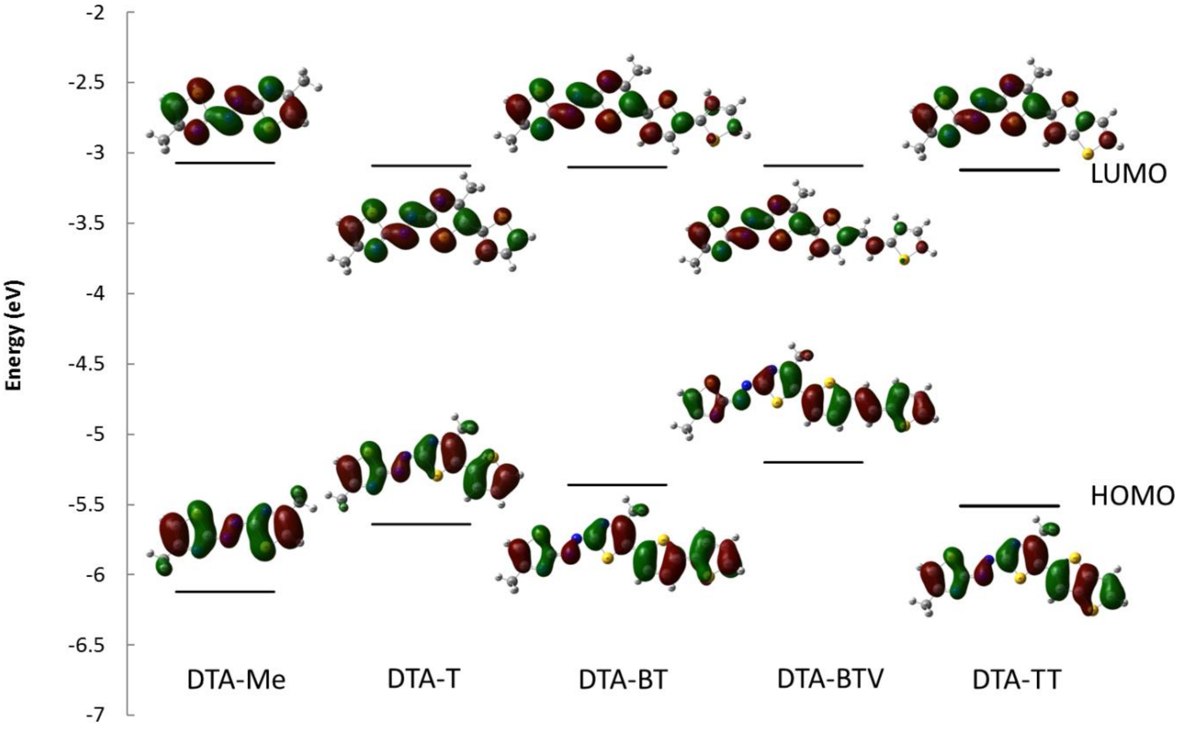

Figure 25. Predicted energy levels of DTA-Me, DTA-BTV, DTA-T, PDTA-BT and PDTA-TT.

We designed four DTA based D-A copolymers, **PDTA-T**, **PDTA-BT**, **PDTA-BTV** and **PDTA-TT**. Geometry optimizations were conducted on each repeating unit, namely DTA-BTV, DTA-T, DTA-BT and DTA-TT and the energy levels of each molecule were predicted (Figure 25). It was observed that in all four molecules, electrons are evenly distributed over the whole molecule in the highest occupied molecular orbital (HOMO). The predicted HOMO energy level of each molecule is higher than the predicted value for DTA-Me, which is due to raise of HOMO by the electron-donating unit resulting from effective donor-acceptor interaction. On the other hand, electron distribution is more localized on the DTA moiety in the lowest unoccupied molecular orbital (LUMO) in each molecule, and the predicted LUMO energy level is close to the LUMO of DTA-Me. These indicated the strong electron deficiency of the DTA building block; therefore, it is potentially a promising electron acceptor for donor-acceptor polymer semiconductors.

3.1.2 Synthesis of Novel DTA Monomers

The synthesis of the dibrominated DTA monomers are outlined in Scheme 10. 1-bromomethyl alkyl ketone (**6**) was prepared via bromination of the corresponding methyl ketone. The alkyl group in the ketone ended up being the side chains in polymers, which are intended to improve the solubility of resulting polymers. White crystals of 1-bromotridecan-2-one (**6a**) can be easily isolated as product precipitated out over reaction process. However, 1-bromo-5-hexyltridecan-2-one (**6b**) bearing branched alkyl groups was separated as an oil from the reaction mixture in methanol, and column chromatography was necessary to separate **6b** from the by-product, its isomer 4-bromo-6-hexyltetradecan-3-one. Reaction of compound **6** with hydrazine-1,2-bis(carbothioamide), followed by oxidation by sodium nitrite yielded 1,2-bis(4-alkylthiazol-2-yl)diazene (**7**). Compound **7a** can be purified through recrystallization from toluene-methanol to give orange crystals in 78 % yield. Compound **7b**, on the other hand, is an orange sticky solid

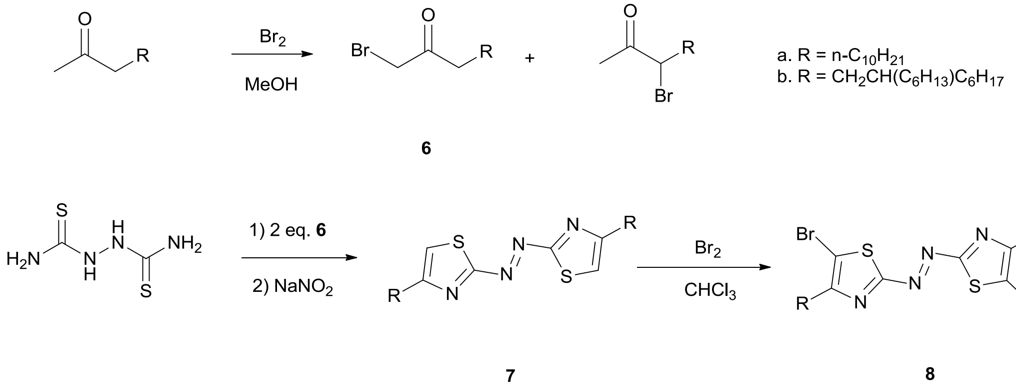

Scheme 10. Synthesis of 1,2-bis(5-bromo-4-alkylthiazol-2-yl)diazene monomers.

and can only be isolated through column chromatography (75 % yield). 1,2-bis(4-alkylthiazol-2-yl)diazene was then subject to brominaition by bromine to give 1,2-bis(5-bromo-4-alkylthiazol-2-yl)diazene (**8**) as the monomer for copolymerization (28–38 %). The bromination was conducted at 0 °C in chloroform in dark to minimize side reactions, the brominaition of methylene groups in alkyl side chains.

3.2 Preparation and characterization of PDTA-T

3.2.1 Synthesis of PDTA-T

The first DTA based D-A copolymer prepared was **PDTA-T**, in which a simple electron donor, thiophene (T) was used. **PDTA-T** was prepared via Stille-coupling polymerization of compound **8a** with 2,5-bis(trimethylstannyl) thiophene in 27 % yield (Scheme 11), and purified through Soxhlet extraction. The polymer exhibits good solubility in common solvents such as chloroform, chlorobenzene and tetrahydrofuran at room temperature. The number average (M_n) and weight average molecular weight (M_w) were measured using gel permeation chromatography (GPC) at a column temperature of 40 °C with THF as an eluent and polystyrene as standards. Accurate values of M_n and M_w cannot be extracted due to the large polydispersity of the polymer. GPC trace of the polymer (Figure A-12) showed multiple peaks, some of which came from oligomers.

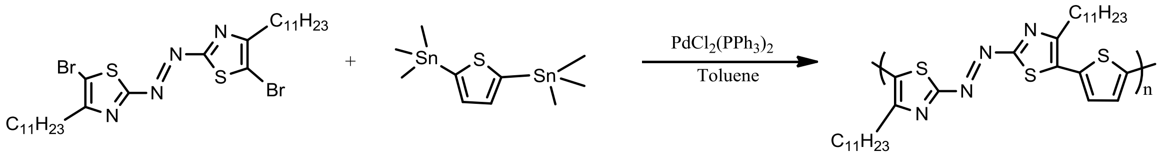

8a

PDTA-T

Scheme 11. Synthesis of **PDTA-T** through Stille-coupling.

3.2.2 Characterization of PDTA-T by UV-Vis, CV, DSC, TGA, AFM and XRD

PDTA-T showed broad absorption over the UV-Vis-NIR range due to *cis-/trans-* transformation of the azo group upon absorption of UV light (Figure 26).[81] **PDAT-T** in chloroform solution exhibited a featureless absorption with a maximum absorbance at 695 nm. In solid state, **PDTA-T** polymer film showed even broader absorption and witnessed a redshift in both maximum absorbance (λ_{max} = 716 nm) and onset absorption (~1018 nm). The optical gap of **PDTA-T** is ~1.22 eV, calculated from the onset wavelength of the polymer thin film.

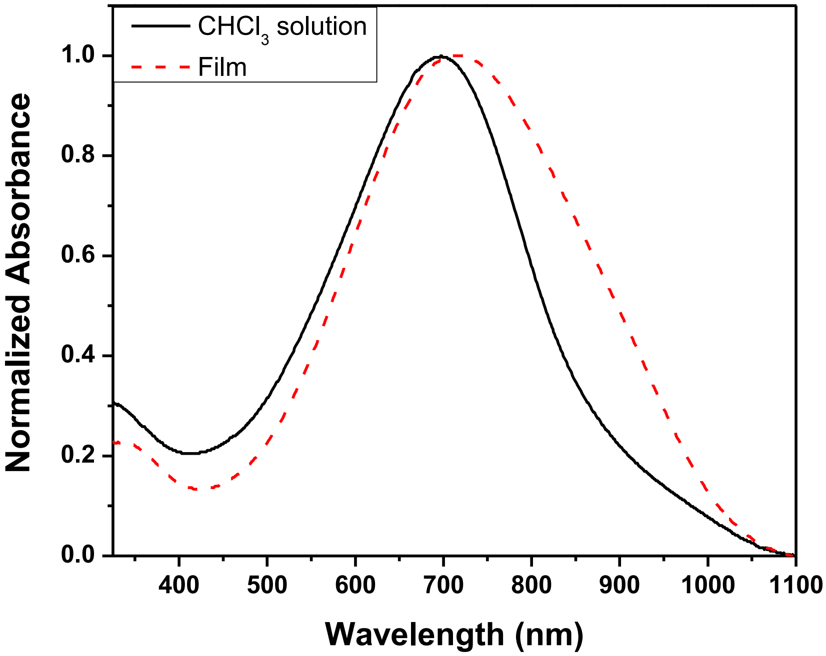

Figure 26. UV-vis-NIR absorption spectra of **PDTA-T** in chloroform ($CHCl_3$) and in a thin film.

The redox properties of **PDTA-T** polymer was investigated by cyclic voltammetry (CV) to determine the highest occupied molecular orbital (HOMO) and lowest unoccupied molecular orbital (LUMO) energy levels (Figure 27). The cyclic voltammogram of **PDTA-T** reversible redox cycles, suggesting that it is stable towards both oxidation and reduction processes. The HOMO/LUMO energy levels are -5.50/-4.21 eV, estimated from the oxidation/reduction onset potential. LUMO energy level calculated from the HOMO from CV and optical bandgap from UV-Vis is -4.28 eV. The difference between the LUMO energy levels from two methods is considered due to the exiton binding energy of this polymer.[24,60]

PDTA-T was subject to thermal gravimetric analysis (TGA) to study its thermal behaviour. A 5 % weight loss was observed at 253 ^{o}C for **PDTA-T** (Figure 28). The phase transition property of **PDTA-T** polymer was characterized with differential scanning calorimetry (DSC) (Figure 29). As the polymer was heated during the first heating scan, it underwent exothermic decomposition as temperature approached 190 ^{o}C (onset temperature) with largest amount of heat released at

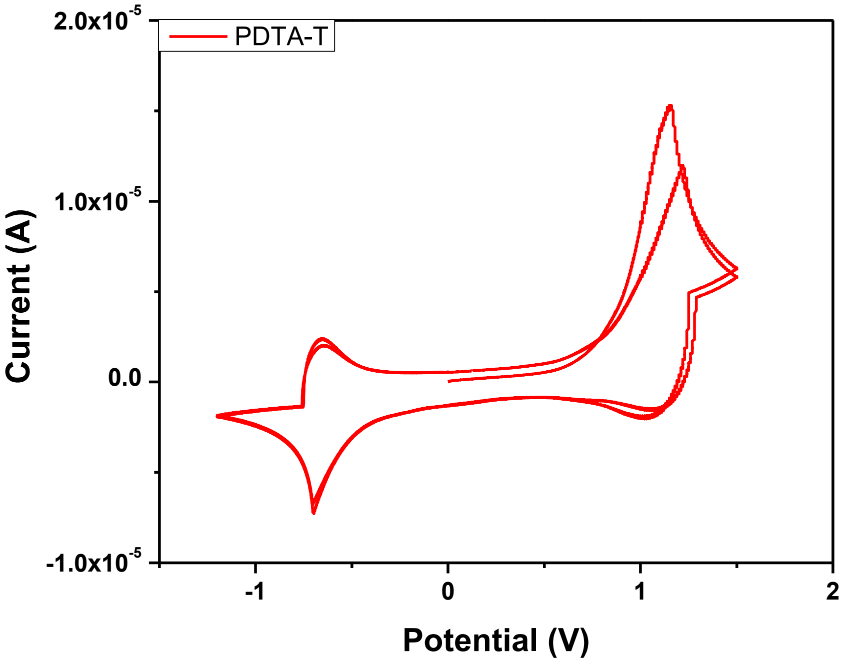

Figure 27. Cyclic voltammogram (two cycles) of a **PDTA-T** thin film showing two oxidative and reductive cycles at a scan rate of 0.05 V s^{-1}. The electrolyte was 0.1 M tetrabutylammonium hexafluorophosphate in anhydrous acetonitrile.

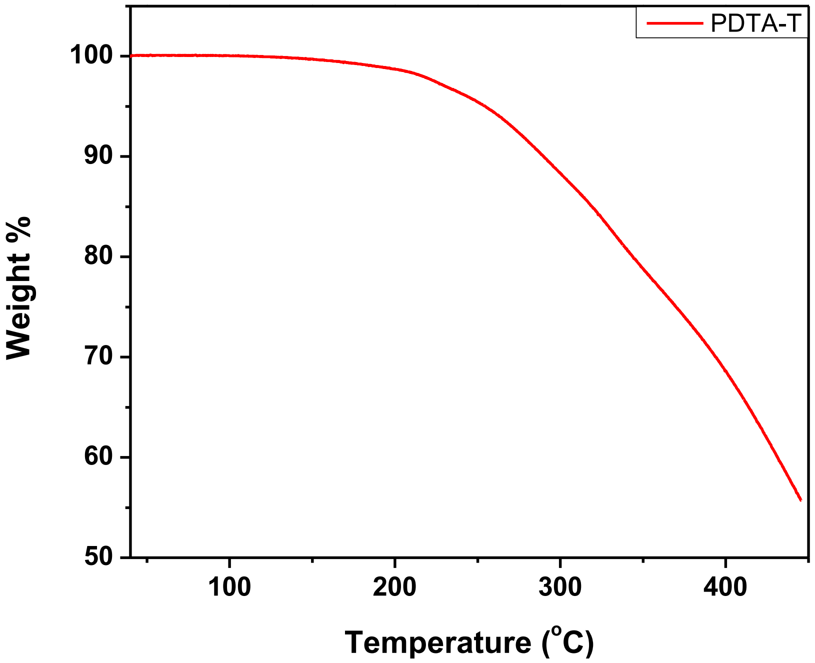

Figure 28. TGA curve of **PDTA-T** measured with a heating rate of 10 ℃·min^{-1} under N_2.

215 °C. Phase transition was observed during neither heating scan nor cooling scan, and no signals were recorded in the second scan due to the decomposition of **PDTA-T** in the first heating scan.

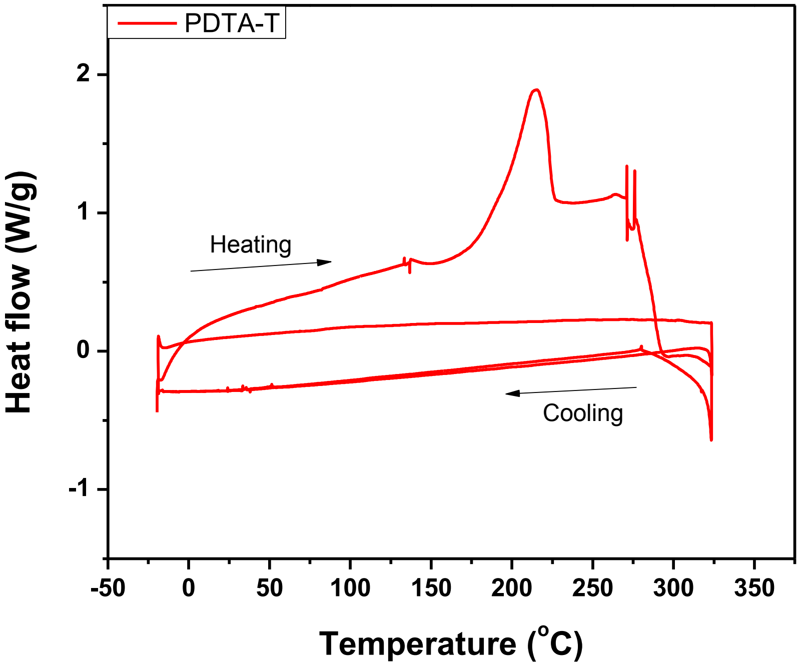

Figure 29. Differential scanning calorimetry (DSC) profiles of **PDTA-T** obtained at a scanning rate of 10 ℃ min^{-1} under nitrogen.

The AFM images of **PDTA-T** thin films annealed at different temperatures not only demonstrated the temperature-dependent morphology of the thin films spin coated on DTS modified SiO_2/Si wafer substrates, but also confirmed the thermal instability of the polymer (Figure 30). As annealing temperature increased from 100 to 150 °C, more closely packed grains with larger grain boundaries were observed. However, further increasing the annealing temperature to 200 °C led to appearance of dark spots on the thin film, which may resulted from the formation of nitrogen gas during the decomposition of azothiazole moieties in the polymer.[83–85] X-ray diffraction patterns (Figure 31) showed that **PDTA-T** film annealed at 100 °C was amorphous with no diffraction peaks observed. Upon annealing at 150 °C, a diffraction peat at 2θ = ~4.0° corresponding to a interlayer distance of ~ 22 Å appeared. A weak second order diffraction peak was also observed at 2θ = ~8.5°. This indicated that a higher degree of crystallinity was observed in the **PDTA-T** film annealed at 150 °C. In agreement with AFM image for the thin film annealed at 200 °C, XRD pattern of the 200 °C-annealed polymer film showed no diffraction peaks due to thermal decomposition.

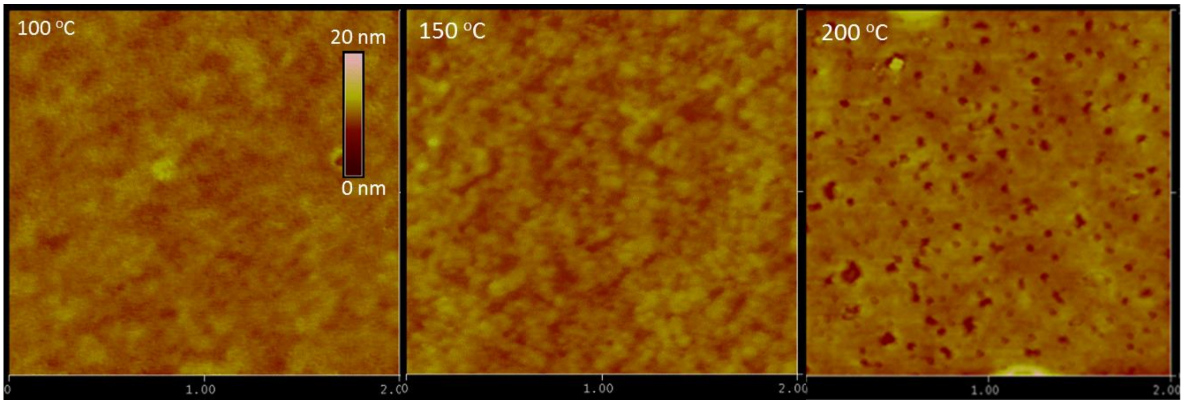

Figure 30. AFM height images (2 × 2 μm) of **PDTA-T** thin films (~35 nm) spin-coated on DTS-modified SiO_2/Si substrates and annealed at different temperatures for 15min under nitrogen.

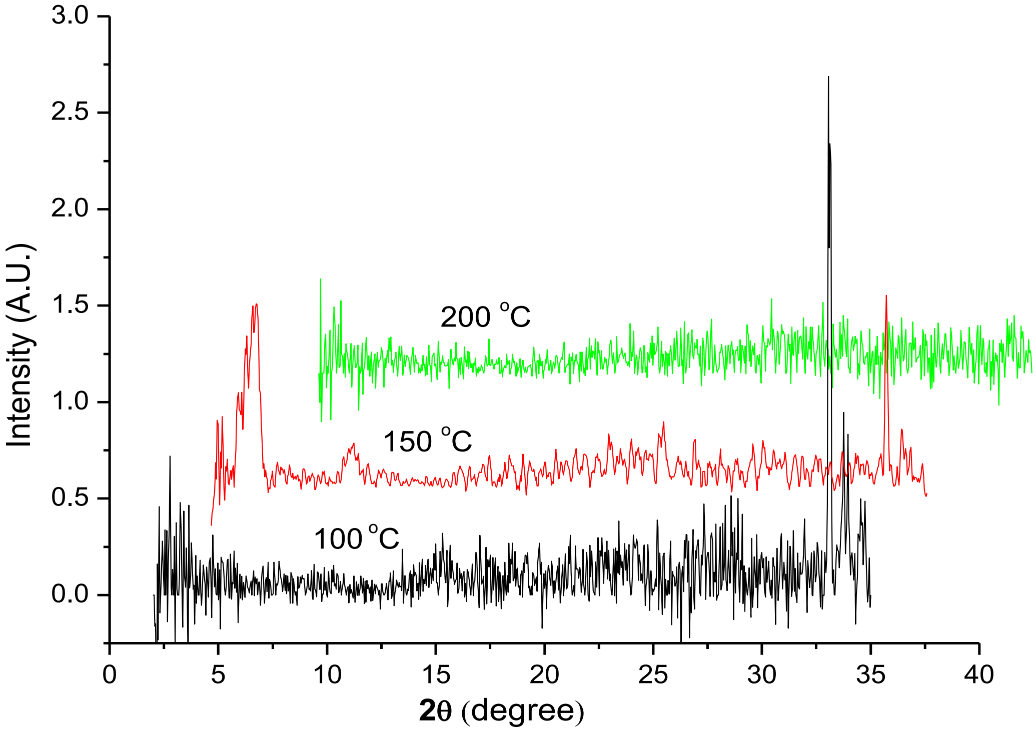

Figure 31. X-Ray diffraction (XRD) data obtained from spin-coated **PDTA-T** thin films on DTS modified SiO_2/Si substrates annealed at different temperatures.

3.2.3 Device performance of PDTA-T

PDTA-T was characterized as the channel semiconductor in bottom-contact, bottom-gate OTFTs with gold being the drain and source electrodes and p-doped silicon wafer being gate electrode. **PDTA-T** thin films were obtained by spin coating a polymer solution in chloroform onto DTS-modified SiO_2 dielectric layer, and optionally annealed at different temperatures in a glove box filled with nitrogen. The devices were then encapsulated with PMMA and tested in ambient condition.

With the low-lying LUMO energy level and the low density of electron donor in the polymer backbone, **PDTA-T** exhibited electron transporting (n-type) characteristics. OTFT devices with non-annealed **PDTA-T** thin films showed almost no performance with low electron mobilities of $\sim 10^{-7}$ $cm^2V^{-1}s^{-1}$ recorded. An average electron mobility of 1.9×10^{-5} $cm^2V^{-1}s^{-1}$ ($I_{on/off}$ = $\sim 10^3$) was extracted from five OTFTs with **PDTA-T** thin films annealed 100 °C. Annealing the polymer thin film at a higher temperature of 150 °C led to an average mobility of 3.3×10^{-4} $cm^2V^{-1}s^{-1}$ ($I_{on/off}$ = $\sim 10^5$). The highest mobility recorded was 4.0×10^{-4} $cm^2V^{-1}s^{-1}$ (Figure 32). This improvement in device performance was attributed to the improvement in crystallinity of the polymer semiconductor upon thermal annealing, as indicated by AFM and XRD results. Because of the instability of the polymer at high temperature, **PDTA-T** annealed at 200 °C and higher temperatures didn't show any performance in OTFTs.

Table 3.1 Summary of OTFT device performance using **PDTA-T** as the channel layers. [a]

Annealing temperature	Electron mobility ($cm^2V^{-1}s^{-1}$)	$I_{on/off}$	V_T (V)
r.t.	No performance		
100 °C	$\mu_e = 1.5 – 2.6 \times 10^{-5}$	$\sim 10^3 – 10^4$	-38
150 °C	$\mu_e = 2.5 – 4.0 \times 10^{-4}$	$\sim 10^4 – 10^5$	-62
200 °C	No performance		

[a] The devices were annealed in a glove box on a hotplate at the selected temperature for 15 min under nitrogen. μ_e are electron mobilities in the saturated regions in electron enhancement mode. Each set of data were obtained from 3-5 OTFT devices.

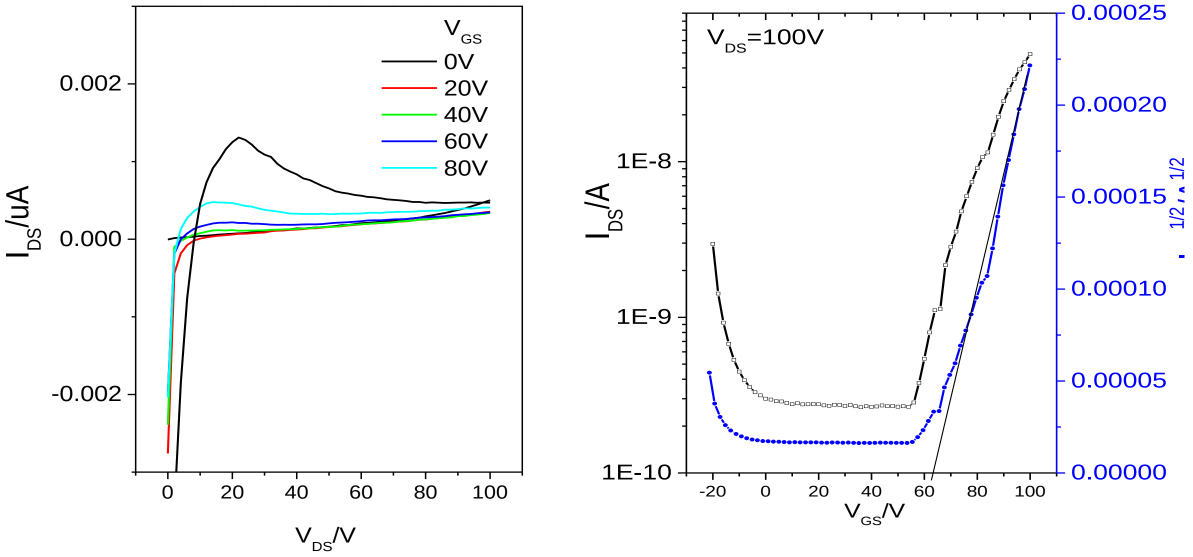

Figure 32. Output (left) and transfer (right) characteristics in the electron enhancement mode of an encapsulated OTFT device with a **PDTA-T** film annealed at 150 °C for 15 min. The calculated hole mobility is 4.0×10^{-4} $cm^2V^{-1}s^{-1}$ at V_{DS} = 100 V. Device dimensions: channel length (L) = 30 µm; channel width (W) = 1 mm.

3.3 Preparation and characterization of PDTA-BT

3.3.1 Synthesis of PDTA-BT

The relatively unsatisfactory performance of **PDTA-T** was considered partially due to the unbalanced area of electron-donor and electron-acceptor in the polymer backbone. To synthesize a copolymer of DTA and thiophene with similar donor and acceptor π-π stacking area, another thiophene ring was introduced into the polymer backbone. A copolymer of DTA and bithiophene (BT), **PDTA-BT** as prepared. Compound **8a** was initially as a monomer to prepare **PDTA-BT** via Palladium-catalyzed Stille-coupling. However, the straight eleven-carbon side chains are not sufficient to solubilize the resulting polymer, suggesting the very strong π-π interaction in the solid state. Compound **8b** was then prepared and copolymerized with 5,5'-bis(trimethylstannyl) bithiophene to afford a solution-processible **PDTA-BT** in 62 % yield. **PDTA-BT** is soluble in chloroform and chlorobenzene at room temperature and can be dissolved in THF at elevated temperature. Number average (M_n) and weight average molecular weight (M_w) were measured using gel permeation chromatography (GPC) at a column temperature of 40 ^{o}C using THF as eluting solvent and polystyrene as standards (Figure A-13). Oligomers were present in the polymer sample, which made the extraction of accurate M_n and M_w values difficult.

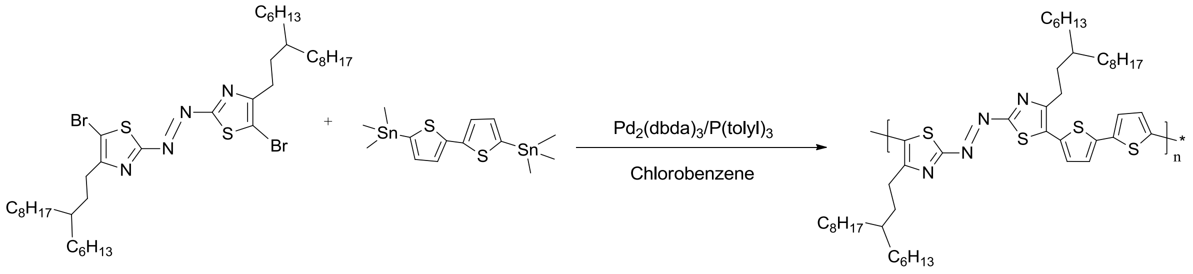

8b

PDTA-BT

Scheme 12. Synthesis of **PDTA-BT** through Stille-coupling**.**

3.3.2 Characterization of PDTA-BT by UV-Vis, CV, DSC, TGA, AFM and XRD

PDTA-BT also showed broad absorption over the visible to near infrared range from 500 to 1000 nm (Figure 33). **PDTA-BT** in chloroform exhibits the maximum absorption (λ_{max}) at 770 nm. In solid thin film, **PDTA-BT** showed a similar maximum absorption (~773 nm), and a shoulder was observed at 862 nm, which implied more distinct energy levels resulting from higher degree of ordering in the thin film of **PDTA-BT**. However, **PDTA-BT** film witnessed a slight blue-shift in onset wavelength (979 nm) compared to its chloroform solution, giving an optical band gap of 1.27 eV.

The electrochemistry property of **PDTA-BT** was investigated by cyclic voltammetry (Figure 34). Reversible and reproducible redox cycles were observed in the cyclic voltammogram, suggesting the stability of this polymer towards both oxidation and reduction processes. The highest occupied molecular orbital (HOMO) and lowest unoccupied molecular orbital (LUMO) energy levels are determined from the oxidation and reduction onset potential. A same HOMO energy level (-5.50 eV) was recorded for **PDTA-BT** as for **PDTA-T**. This appropriate HOMO level, along with the stronger oxidation current than the reduction current in the cyclic voltammogram, suggested that **PDTA-BT** is likely a p-type semiconductor. LUMO energy levels were estimated with two methods, one from reduction onset potential in CV (-4.08 eV), the other from HOMO energy level and the optical bandgap (-4.23 eV). It was noted that the LUMO recorded here is higher than the LUMO level of **PDTA-T**. Hybridization of LUMO's of the extended electron-donor (BT) and electron-acceptor (DTA) accounts for higher LUMO energy level.

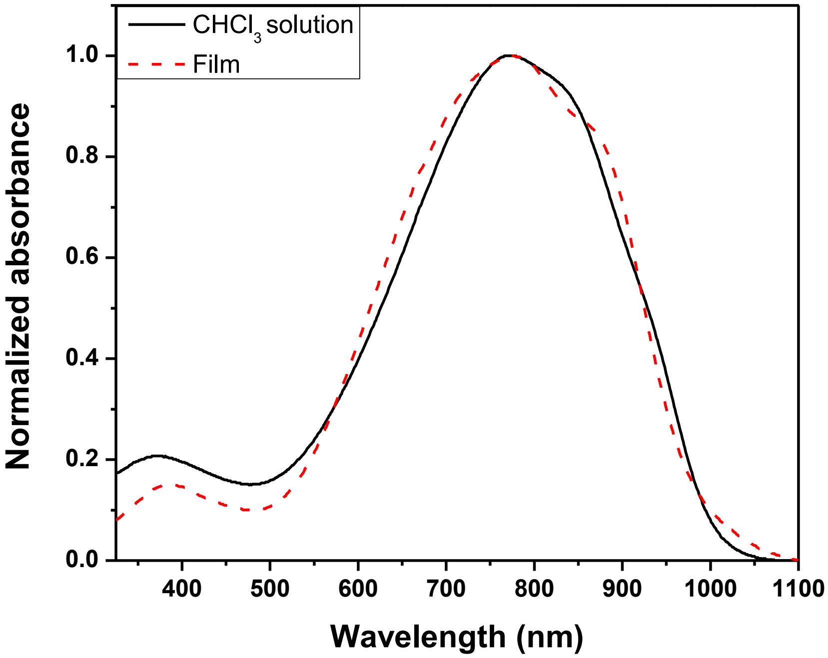

Figure 33. UV-vis-NIR absorption spectra of **PDTA-BT** in chloroform ($CHCl_3$) and in a thin film.

PDTA-BT showed a better thermal stability than **PDTA-T** with a 5 % weight lost in TGA (Figure 35) observed at 304 ^{o}C, 52 ^{o}C higher that the decomposition temperature of **PDTA-T**. The polymer thin film was subject to DSC analysis to characterize the phase transition property (Figure 36). No endothermic peak arising from melting of crystals was recorded during the first heating scan, suggesting the poor crystallinity of the polymer. A broad exothermic peak resulting from decomposition of the polymer was observed at 240 ^{o}C in the first heating scan. This also indicated that although **PDTA-BT** has a slightly better thermal stability then **PDTA-T**, it underwent decomposition upon heating at a higher temperature than ~210 ^{o}C. Therefore, no signals were observed in the second scan.

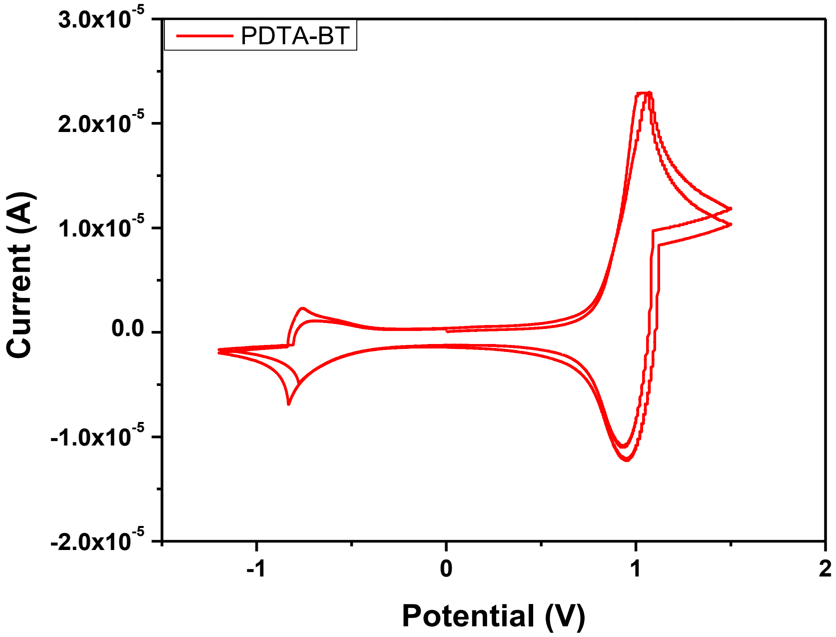

Figure 34. Cyclic voltammogram (two cycles) of a **PDTA-BT** thin film showing two oxidative and reductive cycles at a scan rate of 0.05 V s^{-1}. The electrolyte was 0.1 M tetrabutylammonium hexafluorophosphate in anhydrous acetonitrile.

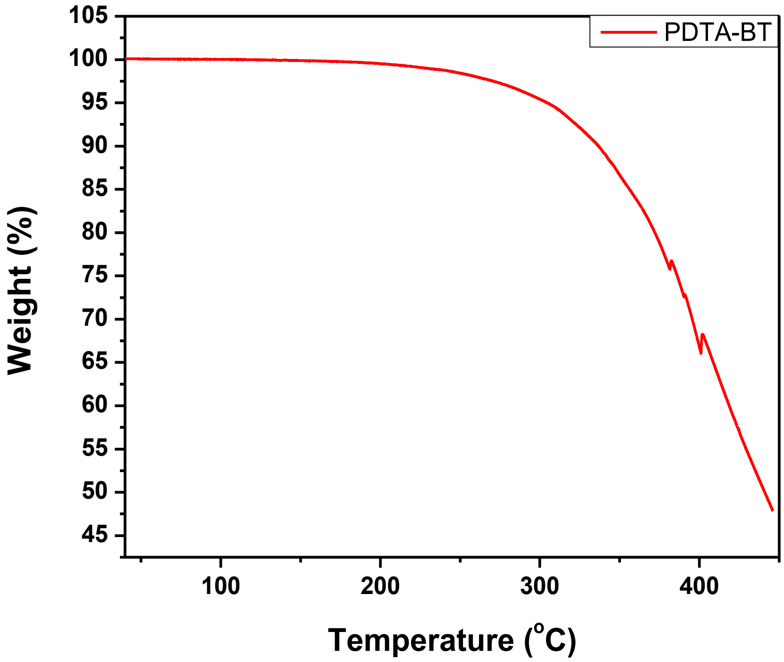

Figure 35. TGA curve of **PDTA-BT** measured with a heating rate of 10 ℃·min^{-1} under N_2.

The AFM images of spin-coated **PDTA-BT** films on dodecyltrichlorosilane (DTS) modified SiO_2/Si wafer substrates annealed at different temperatures are shown in Figure 37. The film annealed at 100 ^{o}C showed connected crystalline grains. Annealing at a higher temperature of 150 ^{o}C gave a smoother film surface with grains of ~30 nm. Further increasing annealing temperature to 200 ^{o}C led to decomposition of **PDTA-BT** film, showing an amorphous surface with small dark spots due to in AFM. XRD analysis (Figure 38) agreed with these observations in AFM. Clear diffraction peaks arising from interlayer spacing up to the second order were observed in the diffractogram of the **PDTA-BT** film annealed at 100 ^{o}C. Two diffraction peaks were observed at $2\theta = 4.27^{o}$ (d = 20.6 Å) and 8.74^{o}. No diffractions arising from π-π stacking were observed. Increasing the annealing temperature to 150 ^{o}C led to a decrease in the interlayer distance with two diffraction peaks observed at $2\theta = 4.58^{o}$ (d = 19.2 Å) and 8.97^{o}. Increase in annealing temperature also led to a decrease in the diffraction intensity. This may result from the *cis*-/*tran*- transformation of the azo group during the thermal treatment,[86] which might cause some defects in crystalline domains. Further increasing annealing temperature to 200 ^{o}C caused the polymer to degrade and no diffraction peaks were observed.

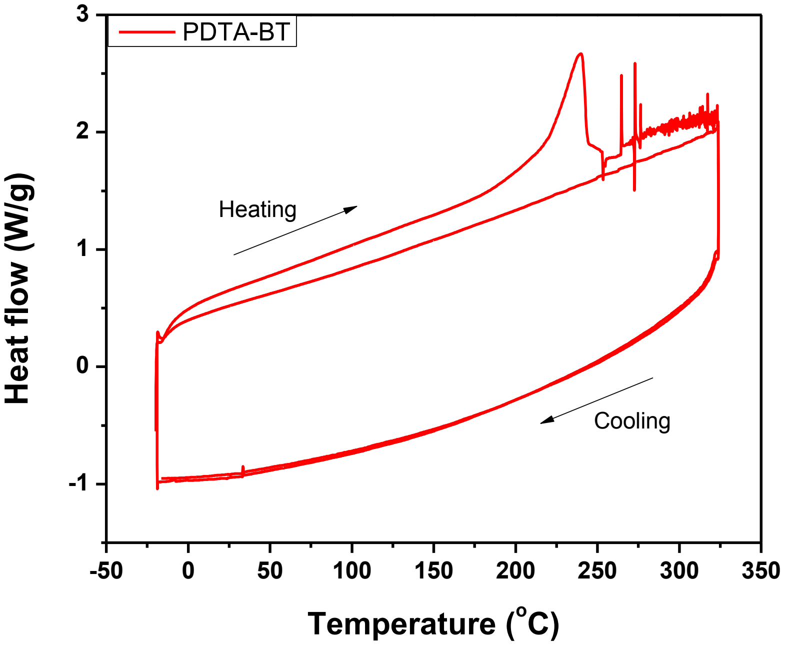

Figure 36. Differential scanning calorimetry (DSC) profiles of **PDTA-BT** obtained at a scanning rate of 10 ℃ min^{-1} under nitrogen.

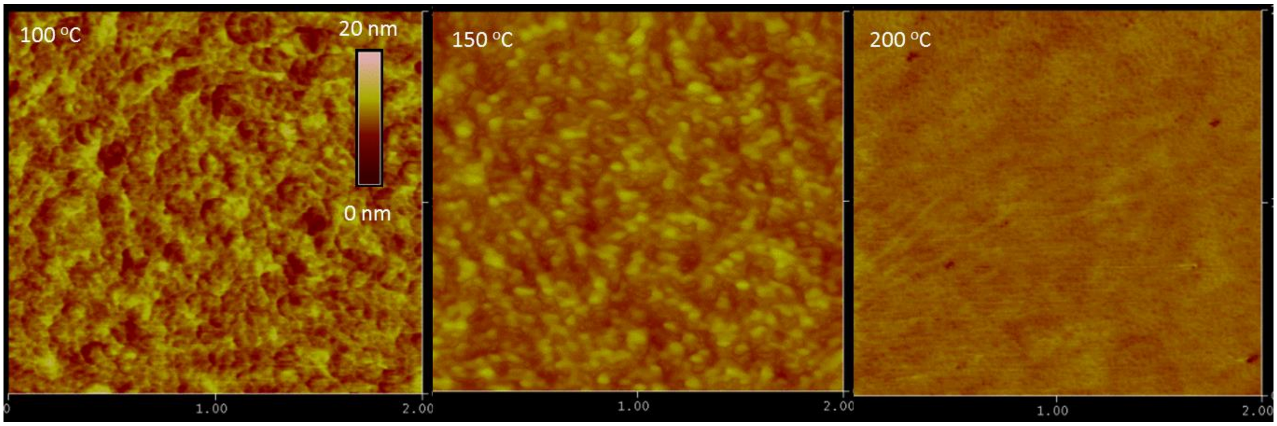

Figure 37. AFM height images (2 × 2 μm) of **PDTA-BT** thin films (~35 nm) spin-coated on DTS-modified SiO_2/Si substrates and annealed at different temperatures for 15min under nitrogen.

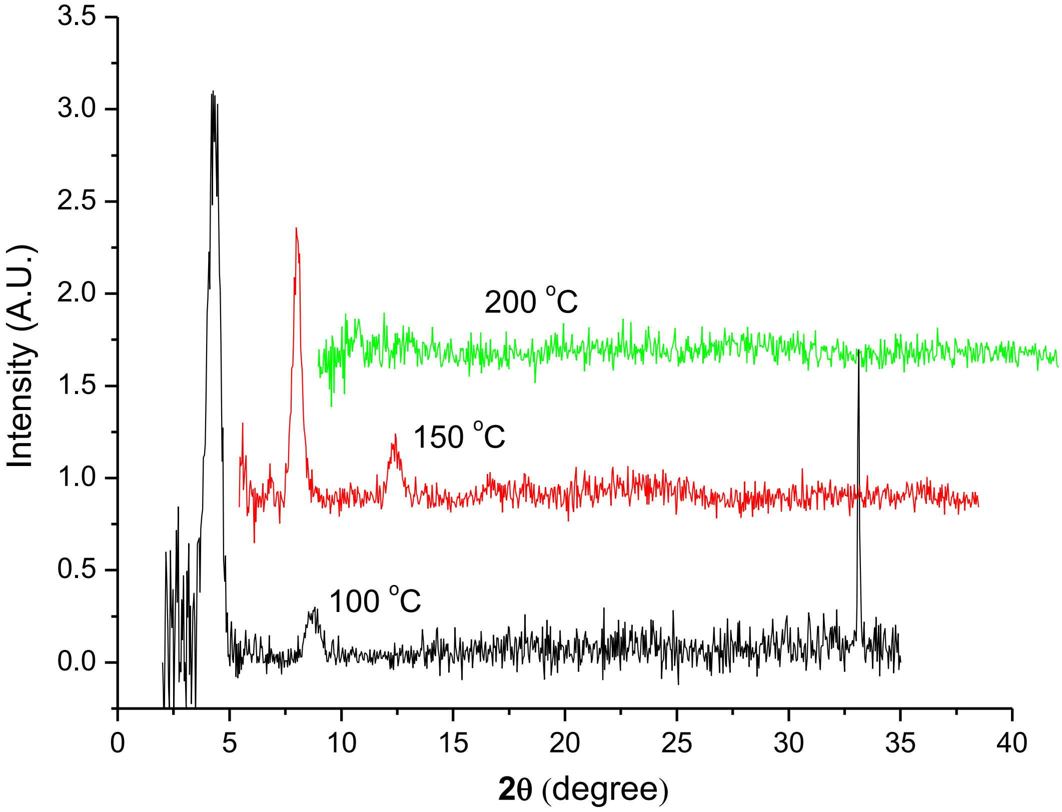

Figure 38. X-Ray diffraction (XRD) data obtained from spin-coated **PDTA-BT** thin films on DTS modified SiO_2/Si substrates annealed at different temperatures.

3.3.3 Device Performance of PDTA-BT

PDTA-BT was tested on OTFT devices using the same configuration as described above for the characterization of **PDTA-T**. Since both AFM and XRD analysis suggested that **PDTA-BT** was unstable when subjected to high temperature treatment, **PDTA-BT** was annealed at moderate temperatures during the fabrication of OTFT devices. All devices are encapsulated with a layer of PMMA of ~500 nm in thickness to prevent contact with air and moisture. With its appropriate HOMO energy level and the increased donor area, **PDTA-BT** showed typical p-type semiconducting characteristic. Hole mobilities, current on-and-off ratios, and threshold voltages measured for OTFTs fabricated with **PDTA-BT** films annealed at different temperatures are listed in Table 3.2. Mobilities listed are calculated from the saturated regions at V_{DS} = -100 V. Non-annealed **PDTA-BT** films exhibited an average hole mobility of 6.4 $\times 10^{-4}$ cm^{2}V^{-1}s^{-1}(V_T = -71 V). An average mobility of 8.8 $\times 10^{-4}$ cm^{2}V^{-1}s^{-1} ($I_{on/off}$ ~ $10^2 – 10^3$) was extracted from four devices with 100 ^{o}C-annealed **PDAT-BT** films. The maximum hole mobility recorded is 9.2 $\times 10^{-4}$ cm^{2}V^{-1}s^{-1} (Figure 39). As shown in XRD patterns, 150 ^{o}C-annealed film has lower crystallinity than 100 ^{o}C-annealed film. This account for the decrease in mobility extracted from OTFTs with **PDTA-BT** films annealed at 150 ^{o}C. The average mobility dropped to 6.8 $\times 10^{-4}$ cm^{2}V^{-1}s^{-1} with the highest mobility of 7.1 $\times 10^{-4}$ cm^{2}V^{-1}s^{-1} recorded.

Table 3.2 Summary of OTFT device performance using **PDTA-BT** as the channel layers.[a]

Annealing Temperature	Hole mobility (cm^{2}V^{-1}s^{-1})	$I_{on/off}$	V_T (V)
r.t.	$\mu_h = 2.3 – 9.0 \times 10^{-4}$	$\sim 10^2 – 10^3$	-71
100 ^{o}C	$\mu_h = 8.3 – 9.2 \times 10^{-4}$	$\sim 10^2 – 10^3$	-69
150 ^{o}C	$\mu_h = 6.3 – 7.1 \times 10^{-4}$	$\sim 10^2 – 10^3$	-62

[a] The devices were annealed in a glove box on a hotplate at the selected temperature for 15 min under nitrogen. μ_h are hole mobilities in the saturated regions in hole enhancement mode. Each set of data was obtained from 3-5 OTFT devices.

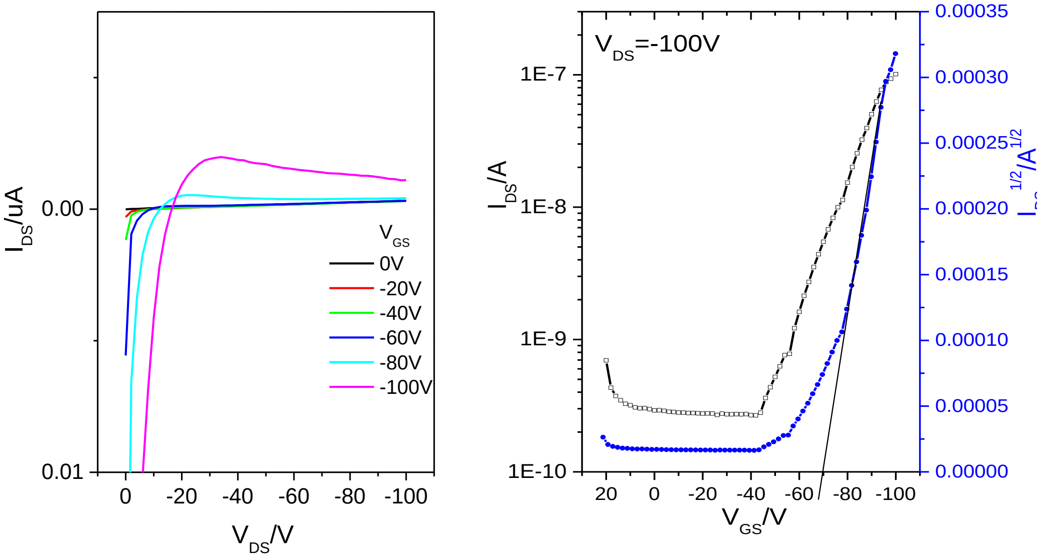

Figure 39. Output (left) and transfer (right) characteristics in the hole enhancement mode of an encapsulated OTFT device with a **PDTA-BT** film annealed at 100 °C for 15 min. The calculated hole mobility is 9.2×10^{-4} $cm^2V^{-1}s^{-1}$ at V_{DS} = -100 V. Device dimensions: channel length (L) = 30 μm; channel width (W) = 1 mm.

3.4 Preparation and Characterization of PDTA-BTV

3.4.1 Synthesis of PDTA-BTV

In order to effectively increase the intermolecular interaction between polymer chains in D-A copolymer, the areas of the donor and the acceptor should be comparable to facilitate effective π-π overlap. Bithiophene-vinylene (BTV) has an analogous structure to DTA with two 5-membered thiophene ring connected by a carbon-carbon double bond. Meanwhile, both vinylene and thiophene moieties are known to be electron-rich, thus potentially useful as electron-donating groups in D-A copolymer.

PDTA-BTV combined DTA as electron-acceptor and BTV as electron-donor in the main backbone. Compound **8a** was copolymerized with (E)-((4-dodecyl-5-(2-(3-dodecyl-5-(trimethylstannyl) thiophen-2-yl)vinyl)thiophen-2-yl)dimethylstannyl)methylium in toluene catalyzed by $PdCl_2(PPh_3)_2$ to yield PDTA-BTV (Scheme 13). Bearing four straight side chains in one repeating unit, **PDTA-BTV** showed excellent solubility with majority of the polymer dissolved in hexane after oligomers and impurities were removed using methanol through Soxhlet extraction. Only 14.5 mg (7 % of theoretical yield) of polymer was dissolved in chloroform. Due to the low yield of the polymerization reaction, **PDTA-BTV** was characterized by only UV-Vis and CV. Device performance data were collected for **PDTA-BTV**.

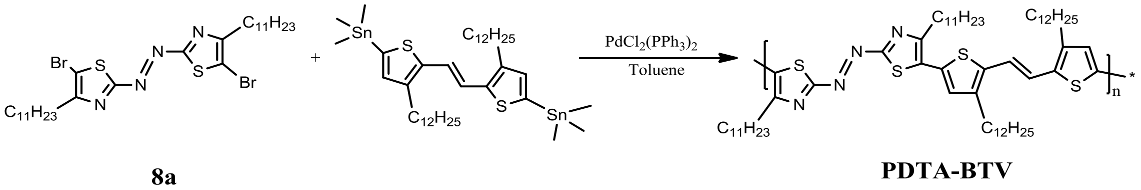

Scheme 13. Synthesis of **PDTA-BTV** through Pd(II) catalyzed Stille-coupling.

3.4.2 Characterization of PDTA-BTV by UV-Vis and CV

UV-Vis-NIR spectra of **PDTA-BTV** were obtained for both drop cast film and chloroform solution of the polymer (Figure 40). In chloroform solution, **PDTA-BTV** exhibited a maximum absorption (λ_{max}) at 720 nm. The **PDTA-BTV** thin film showed broader absorption with a blue-shift in λ_{max} but a red- shift of ~160 nm in onset wavelength. In solid state, **PDTA-BTV** showed maximum absorbance at 667 nm and onset absorption at ~1050 nm. The optical band gap of the polymer was then calculated to be 1.18 eV. This small bandgap is ideal for applications in organic solar cells for effective light harvesting.

Electrochemistry of **PDTA-BTV** was investigated by cyclic voltammetry (Figure 41). HOMO energy level of **PDTA-BTV** was determined from the oxidation onset potential in CV to be -5.32 eV. LUMO energy level was determined from the optical band gap and HOMO energy level to be -4.14 eV. **PDTA-BTV** was predicted to be hole transporting (p-type) polymer semiconductor based on the fact that repeatable oxidation current with two oxidation peaks was observed, while weak reduction current was measured.

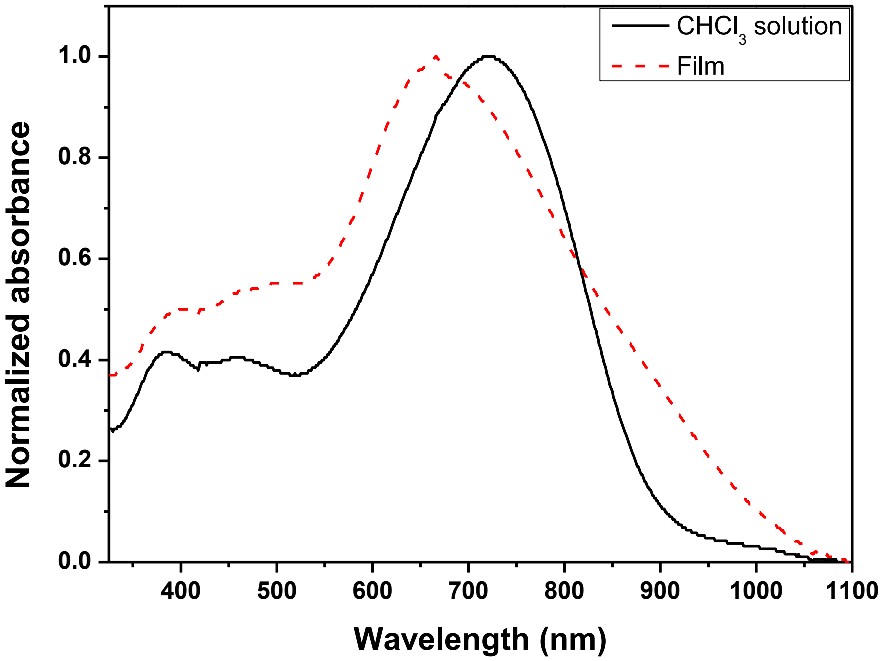

Figure 40. UV-vis-NIR absorption spectra of **PDTA-BTV** in chloroform and in a thin film.

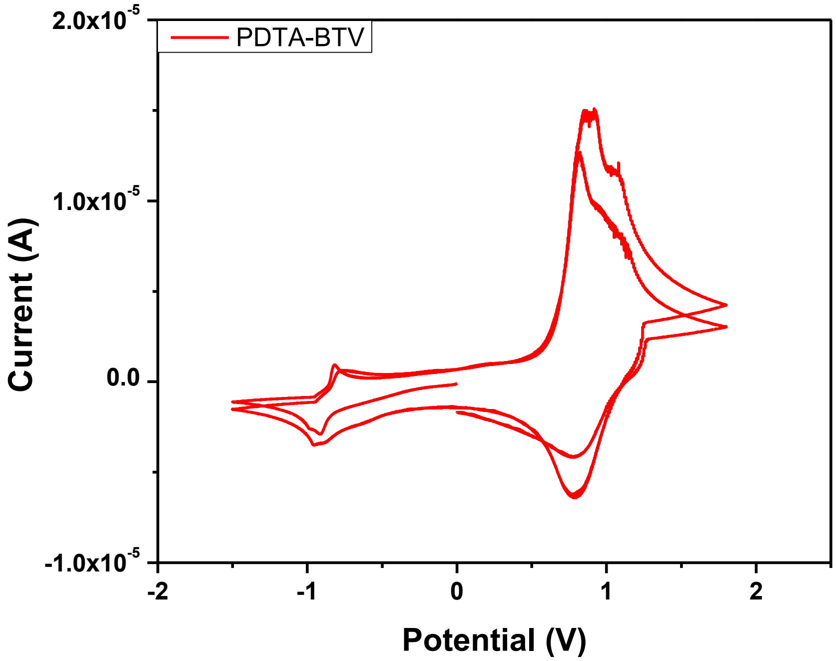

Figure 41. Cyclic voltammograms (two cycles) of a **PDTA-BTV** thin film showing two oxidative and reductive cycles at a scan rate of 0.05 V s^{-1}. The electrolyte was 0.1 M tetrabutylammonium hexafluorophosphate in anhydrous acetonitrile.

3.4.3 Device Performance of PDTA-BTV

PDTA-BTV was evaluated as a channel semiconductor in OTFT devices with bottom-contact, bottom-gate configuration. Gold was used as source and drain electrode, and doped p-silicon wafer was used as gate electrode. The polymer thin film was spin-coated on top of the DTS-modified SiO_2/Si substrate from a 1 % chloroform solution of **PDTA-BTV**. The polymer film was optionally annealed at a selected temperature for 15 min under nitrogen atmosphere. The device was then encapsulated by a layer of PMMA of 500 nm in thickness and dried at 80 ^{o}C for 30 min.

Table 3.3 Summary of OTFT device performance using **PDTA-BTV** as the channel layers. [a]

Annealing temperature	Hole mobility ($cm^2V^{-1}s^{-1}$)	I_{on}/I_{off}	V_T (V)
r.t.	$\mu_h = 0.93 - 1.3 \times 10^{-3}$	$\sim 10^3 - 10^4$	-4.4
100 °C	$\mu_h = 1.2 - 1.5 \times 10^{-3}$	$\sim 10^3 - 10^4$	-5
150 °C	No performance		

[a] The devices were annealed in a glove box on a hotplate at the selected temperature for 15 min under nitrogen. μ_h are hole mobilities in the saturated regions in hole enhancement mode. Each set of data were obtained from 3-5 OTFT devices.

As expected, all devices fabricated with **PDTA-BTV** thin film exhibited typical p-type characteristics. OTFTs with non-annealed **PDTA-BTV** films exhibited an average hole mobility of 1.1×10^{-3} $cm^2V^{-1}s^{-1}$ ($I_{on/off}$ = ~ 10^3). Thermal annealing of the polymer thin film didn't bring about significant increase in mobilities. The highest mobility of 1.5×10^{-3} $cm^2V^{-1}s^{-1}$ was recorded for an OTFT device with a **PDTA-BTV** film treated at a moderate temperature of 100 ^{o}C. The output and transfer curve for the OTFT giving the highest hole mobility are presented in Figure 42. An average hole mobility of 1.3×10^{-3} $cm^2V^{-1}s^{-1}$ (V_T= -5 V) in the saturation regime with a current on-to-off ratio (I_{on}/I_{off}) ratios of 10^3 was extracted from five OTFT devices with 100 ^{o}C-annealed **PDTA-BTV** thin films. **PDTA-BTV** films annealed at 150 ^{o}C or higher temperature showed no performance which is probably because of the instability of the polymer during the annealing process. Although **PDTA-BTV** didn't show impressive mobilities, considering its excellent solubility and ultralow bandgap it is a potential candidate for OPV applications where a mobility of ~10^{-3} is high enough for most applications.

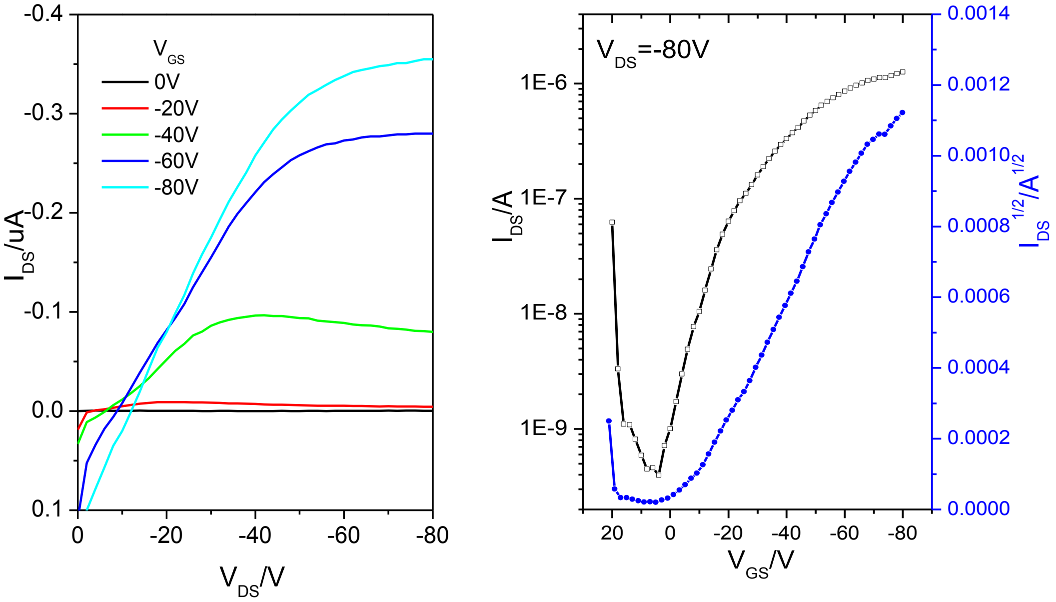

Figure 42. Output (left) and transfer (right) characteristics of the **PDTA-BTV** based OTFT device showing the best performance. **PDTA-BTV** thin film annealed at 100 °C was used as the channel layer. The calculated hole mobility is 1.5 × 10^{-3} $cm^2V^{-1}s^{-1}$ at V_{DS} = -80 V. Device dimensions: channel length (*L*) = 30 μm; channel width (*W*) = 1 mm.

3.5 Preparation and characterization of PDTA-TT

3.5.1 Synthesis of PDTA-TT

Fused aromatic electron-donor, thieno[3,2-b]thiophene (TT) was also copolymerized with DTA to afford a D-A copolymer, **PDTA-TT. PDTA-TT** was prepared via Stille-coupling polymerization of compound **8b** with 2,5-bis(trimethylstannyl)thieno[3,2-b]thiophene (Scheme 14). The polymer was purified through Soxhlet extraction using methanol, acetone, hexane and dichloromethane, and dissolved in chloroform (0.187 g, 68 % yield). Number average (M_n) and weight average molecular weight (M_w) were measured using gel permeation chromatography (GPC) at a column temperature of 40 °C using THF as eluting solvent and polystyrene as standards (Figure A-14). GPC trace showed a broad peak overlapping with two sharp peaks. As the case in **PDTA-T** and **PDTA-BT**, the presence of oligomers in the polymer sample, made the extraction of accurate M_n and M_w values difficult.

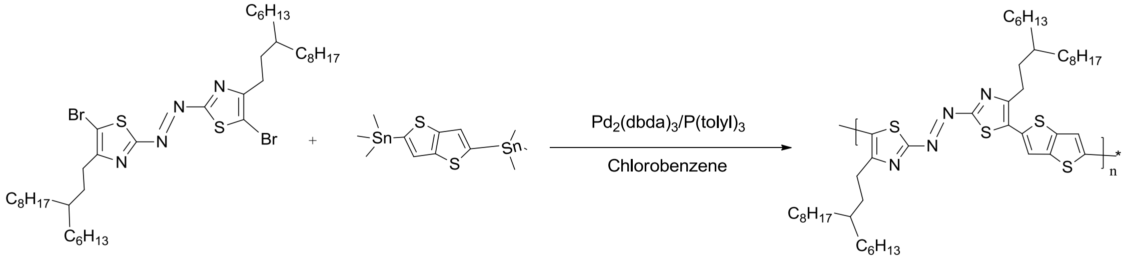

8b

PDTA-TT

Scheme 14. Synthesis of **PDTA-TT** through Stille-coupling**.**

3.5.2 Characterization of PDTA-TT by UV-Vis, CV, DSC, TGA, AFM and XRD

PDTA-TT showed broad and featureless absorption over visible-near infrared range (Figure 43). The absorption spectra of **PDTA-TT** in different solvents revealed the polymer's solvent-dependent light absorption. **PDTA-TT** in chloroform exhibited a maximum absorption at 810 nm, while in tetrahydrofuran and in toluene **PDTA-TT** showed λ_{max} at 800 nm. The **PDTA-TT** solid film showed a blue-shift of ~40 nm in λ_{max} (810 nm) but a ~84 nm blue-shift in onset absorption (1016 nm), as compared to its chloroform solution. The THF and toluene solution showed a similar cut-off wavelength to the solid state. The optical band gap is calculated to be ~1.22 eV from the absorption cut-off wavelength for **PDTA-TT** thin film.

PDTA-TT showed similar reproducibility and reversibility in cyclic voltammogram (Figure 44) as **PDTA-BT**. A stronger oxidation current was observed than the reduction current, suggesting potential hole transport characteristic of this polymer. The HOMO/LUMO are -5.53/-3.98 eV, determined from oxidation/reduction onset potential. Taking exciton binding energy into account, [24,60] the LUMO energy level calculated from HOMO in CV and optical bandgap is -4.31 eV.

Thermal gravimetric analysis of **PDTA-TT** polymer showed a 5 % weight lost at 287 ^oC (Figure 45). Differential scanning calorimetry (DSC) analysis of PDTA-TT showed no

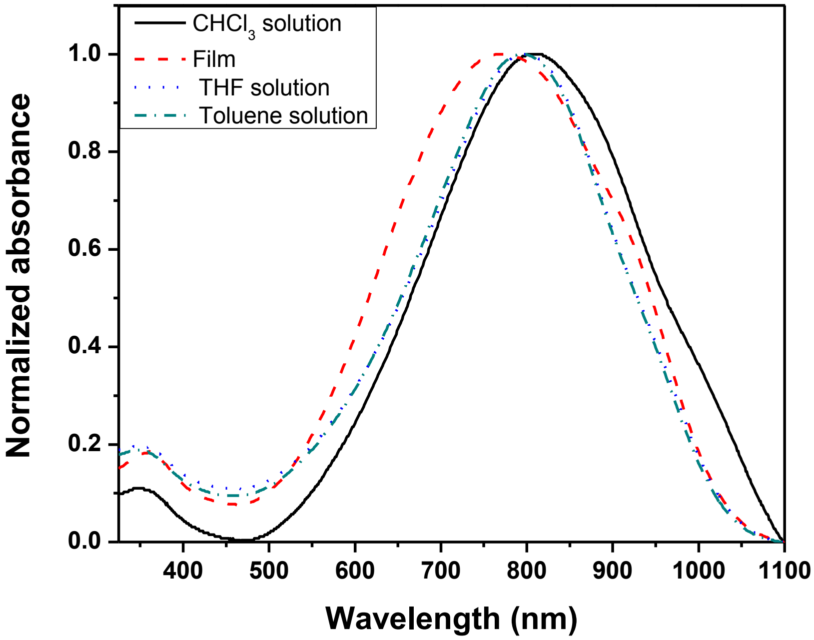

Figure 43. UV-vis-NIR absorption spectra of **PDTA-TT** in chloroform (CHCl$_3$), tetrahydrofuran, toluene and in a thin film.

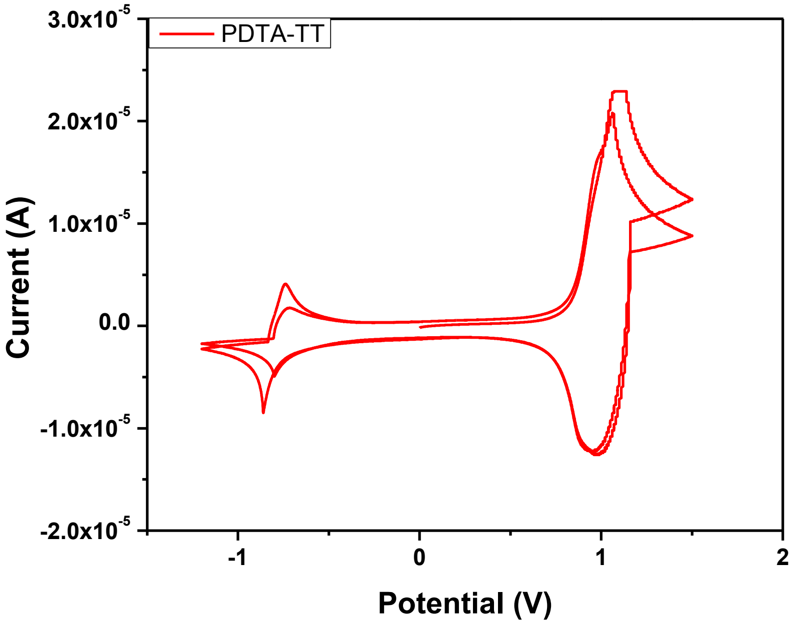

Figure 44. Cyclic voltammogram (two cycles) of a **PDTA-TT** thin film showing two oxidative and reductive cycles at a scan rate of 0.05 V s^{-1}. The electrolyte was 0.1 M tetrabutylammonium hexafluorophosphate in anhydrous acetonitrile.

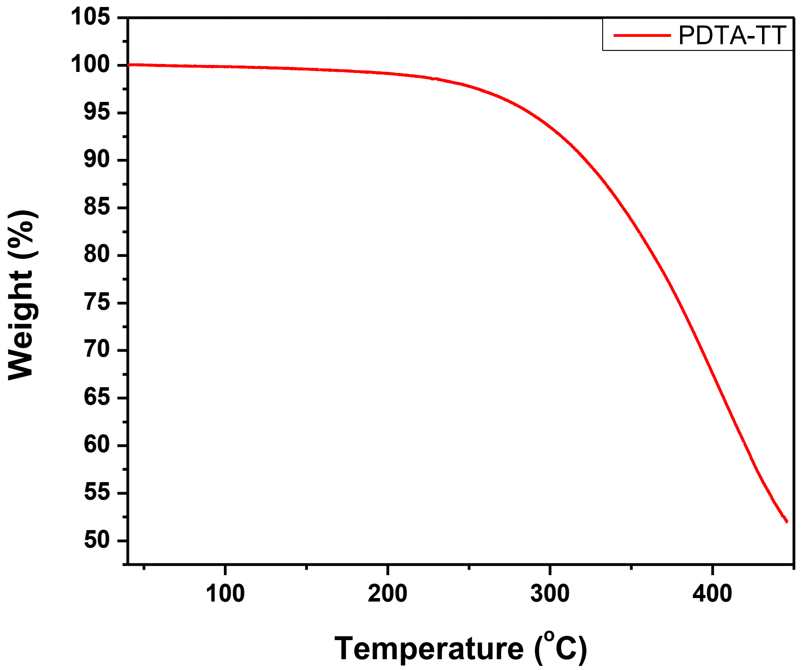

Figure 45. TGA curve of **PDTA-TT** measured with a heating rate of 10 ℃·min^{-1} under N$_2$.

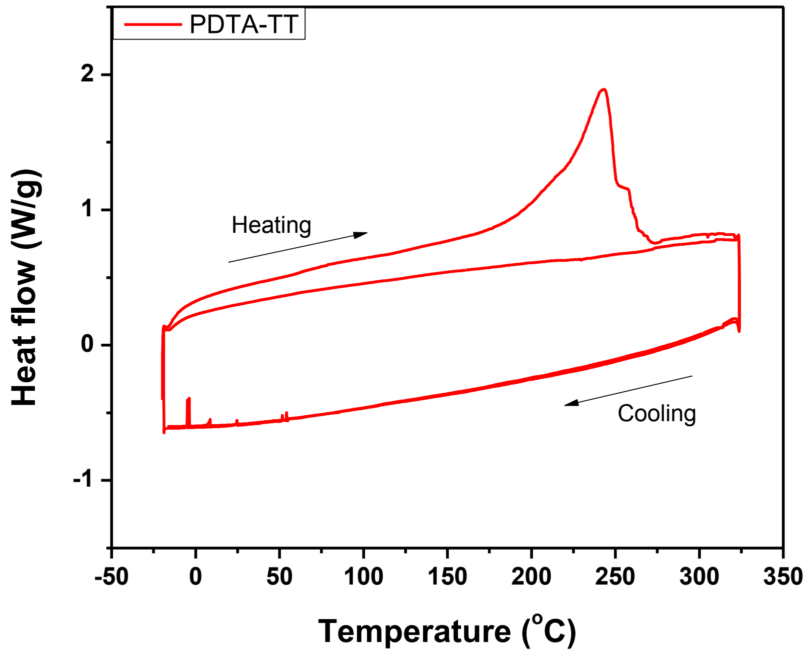

Figure 46. Differential scanning calorimetry (DSC) profiles of **PDTA-TT** obtained at a scanning rate of 10 ℃ min^{-1} under nitrogen.

endothermic peak resulting from melting of crystalline domains during the first heating scan. Similar to **PDTA-T** and **PDTA-BT**, a broad exothermic peak from 187 to 263 ^{o}C (maximum at 243 ^{o}C) in the first heating scan was observed due to the degradation of **PDTA-TT** (Figure 46). The crystallinity and thermal stability of **PDAT-TT** films were studied by AFM (Figure 47). The polymer film annealed at 100 ^{o}C showed grains of ~20 to 40 nm in size with large grain boundaries. The surface of the film became more uniform after annealed at 150 ^{o}C for 15 min under nitrogen atmosphere. Same as the case in **PDTA-T** and **PDTA-BT**, annealing **PDTA-TT** thin film at 200 ^{o}C caused the polymer to degrade. An amorphous film with dark spots was observed in the AFM image due to the formation of nitrogen gas bubbles during the decomposition.

The XRD patterns of **PDTA-TT** films annealed at different temperatures showed a similar temperature-dependent trend as observed for **PDTA-BT** films. **PDTA-TT** films showed a larger interlayer spacing (d = 23.2 Å) than **PDTA-BT** with first and second order diffraction peaks observed at $2\theta = 3.88^{o}$ and 7.83^{o}, respectively. Annealing the polymer film at 150 ^{o}C allowed closer packing of layers in crystalline domains, and a diffraction peak was observed at $2\theta = 4.11^{o}$ (d = 21.4 Å). Same as the case in **PDTA-BT**, diffraction intensity decreased as annealing temperature increased from 100 to 150 ^{o}C and a weak second order diffraction peak was observed at $2\theta \sim 8.2^{o}$. Due to its thermal instability, **PDTA-TT** film annealed at 200 ^{o}C showed no diffraction peaks, which is in accordance with AFM analysis result.

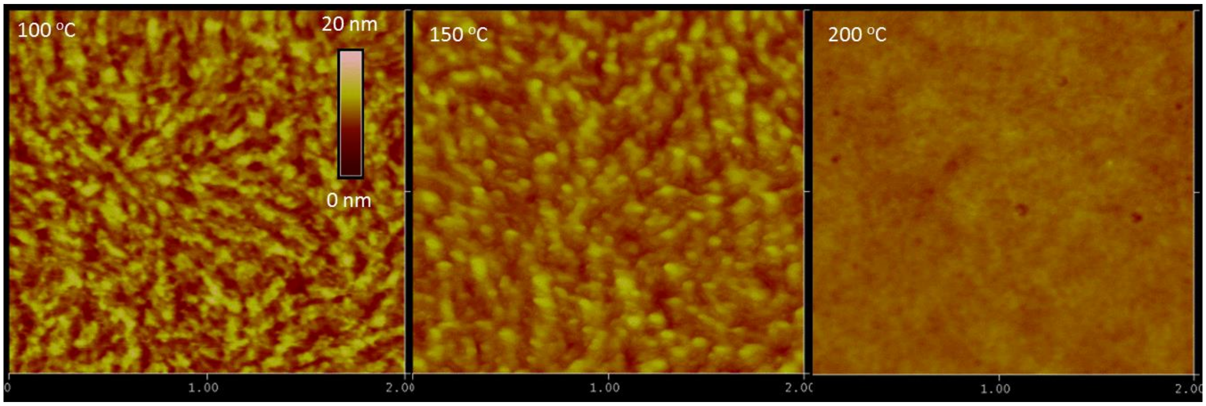

Figure 47. AFM height images (2 × 2 μm) of **PDTA-TT** thin films (~35 nm) spin-coated on DTS-modified SiO_2/Si substrates and annealed at different temperatures for 15min under nitrogen.

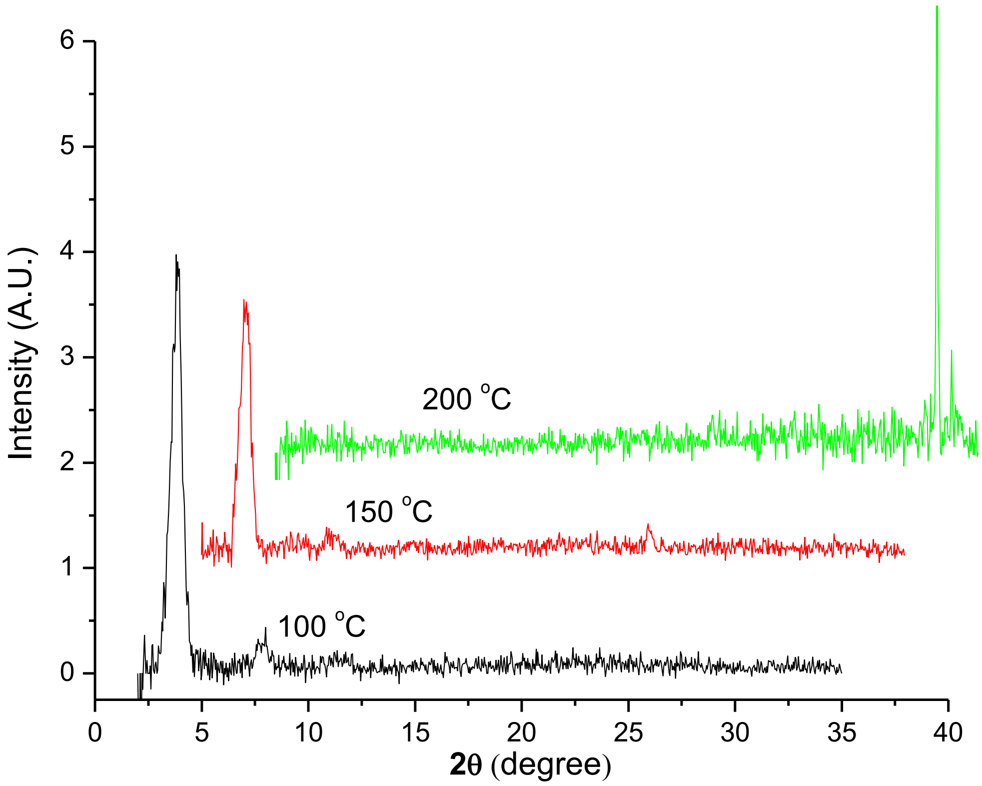

Figure 48. X-Ray diffraction (XRD) data obtained from spin-coated **PDTA-TT** thin films on DTS modified SiO_2/Si substrates annealed at different temperatures.

3.5.3 Device Performance of PDTA-TT

PDTA-TT was tested on bottom-gate, bottom contact OTFTs as used for characterizing **PDTA-T** and **PDTA-BT**. Gold was used as the drain and source electrodes, and n-doped silicon wafer was used as gate electrode. Again, only moderate temperature thermal treatments were applied to the polymer thin film considering the poor thermal stability of **PDTA-TT**. The spin coated **PDTA-TT** thin films on DTS-modified SiO_2 dielectric layer were optionally annealed at different temperatures in a glove box filled with nitrogen. The devices were then encapsulated with PMMA and tested outside the glove box. Since fused aromatic rings can provide increased π-π overlap area thus stronger intermolecular interaction,[18] a donor-acceptor copolymer with thieothiophene as the donor is expected to show similar, if not better, device performance than that with bithiophene when a same acceptor is used. As far as we are concerned here, **PDTA-TT** and **PDTA-BT** showed comparable performance in OTFTs. All OTFTs fabricated with **PDTA-**

TT exhibited hole transporting characteristics with mobility close to 10^{-3} $cm^2V^{-1}s^{-1}$ observed (Table 3.4).

Table 3.4 Summary of OTFT device performance using **PDTA-TT** as the channel layers.

Annealing temperature	Hole Mobility ($cm^2V^{-1}s^{-1}$)	$I_{on/off}$	V_T (V)
r.t.	$3.5 – 9.9 \times 10^{-4}$	$\sim10^2 – 10^3$	-70
100 °C	$1.1 – 1.9 \times 10^{-4}$	$\sim10^3 – 10^4$	-62
150 °C	$1.6 – 2.6 \times 10^{-4}$	$\sim10^3 – 10^4$	-64

[a] The devices were annealed in a glove box on a hotplate at the selected temperature for 15 min under nitrogen. μ_h are hole mobilities in the saturated regions in hole enhancement mode. Each set of data were obtained from 3-5 OTFT devices.

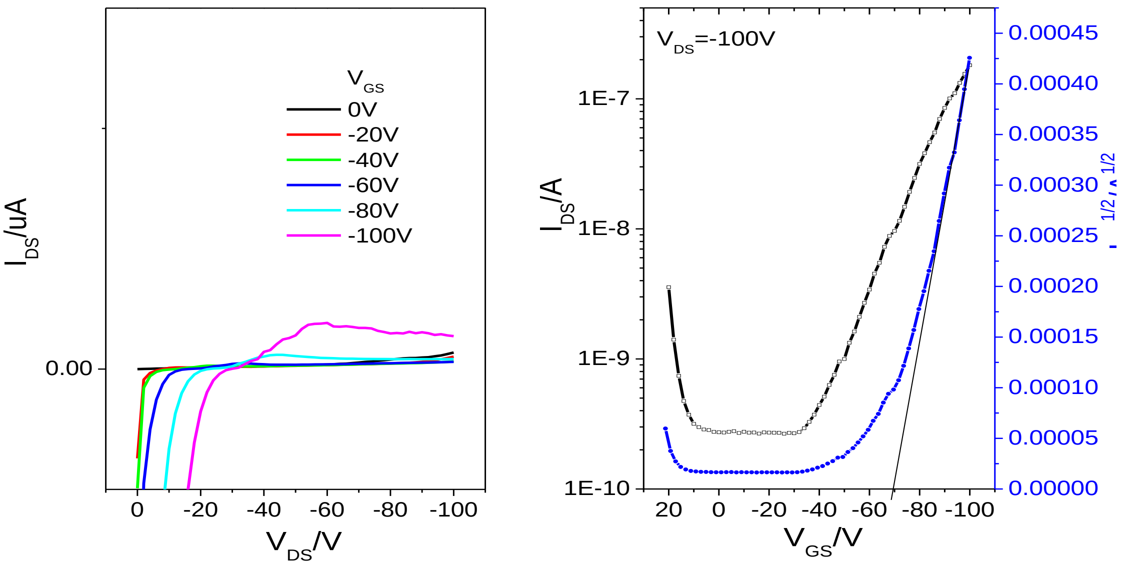

Figure 49. Output (left) and transfer (right) characteristics in the hole enhancement mode of an encapsulated OTFT device with a **PDTA-TT** film annealed at 100 °C for 15 min. The calculated hole mobility is 9.2×10^{-4} $cm^2V^{-1}s^{-1}$ at V_{DS} = -100 V.

To our surprise, the highest mobility was achieved in OTFTs with non-annealed **PDTA-TT** films. The hole mobility was up to $9.9 \times 10^{-4} \times 10^{-4}$ $cm^2V^{-1}s^{-1}$ ($I_{on/off}$~10^3, V_T = -70 V) (Figure 49). Thermal treatment of the polymer thin film led to decrease in charge carrier mobility but increase in current on-and-off ratio. An average mobility of 1.4 ×10^{-4} $cm^2V^{-1}s^{-1}$ was extracted from four OTFTs fabricated with 100 °C-annealed **PDTA-TT** films. Increasing the annealing temperature to 150 °C led to a slight increase in hole mobility and threshold voltage. The average mobility from four devices is 2.2 ×10^{-4} $cm^2V^{-1}s^{-1}$.

3.6 Experimental Section

3.6.1 General

All chemicals were purchased from Sigma-Aldrich and used without further purification. 5-Hexyltridecan-2-one was synthesized according to the literature method[87,88].

Geometry optimizations of (E)-1,2-bis(4-methylthiazol-2-yl)diazene (DTA-Me), (E)-4-methyl-2-((4-methylthiazol-2-yl)diazenyl)-5-(thiophen-2-yl)thiazole (DTA-T), (E)-5-([2,2'-bithiophen]-5-yl)-4-methyl-2-((4-methylthiazol-2-yl)diazenyl)thiazole (DTA-BT), 4-methyl-2-((E)-(4-methylthiazol-2-yl)diazenyl)-5-(5-((E)-2-(thiophen-2-yl)vinyl)thiophen-2-yl)thiazole (DTA-BTV), and (E)-4-methyl-2-((4-methylthiazol-2-yl)diazenyl)-5-(thieno[3,2-b]thiophen-2-yl)thiazole (DTA-TT) were performed with density functional theory (DFT) calculation using the B3LYP hybrid functional[73,74] with the 6-31G* basis set. Molecular orbital shapes and energies discussed in the text are those calculated at the optimized structures. Orbital pictures were prepared with GaussView 5.0 software.[75] All calculations were performed with Gaussian 09 package[76,77] on the Shared Hierarchical Academic Research Computer Network (SHARCNET) of Canada.

Instruments and methods used for acquiring ^1H NMR, UV-vis, CV, DSC, TGA, AFM and XRD data are same as described above in section 2.5.1. Gel permeation chromatography (GPC) measurement of **PDTA-T**, **PDTA-BT** and **PDTA-TT** was performed on Waters 2690 System using THF as eluent and polystyrene as standards at a column temperature of 40 °C.

3.6.2 Fabrication and Characterization of OTFT devices

The device fabrication procedure used for testing DTA based copolymers was same as that described in section 2.5.2 for the fabricating OTFTs of **P6-IBDF-T**. P-doped Si wafer was used for fabricating **PDTA-T** based OTFTs, and n-doped Si wafer was used for **PDTA-BT**, **PDTA-**

BTV and **PDTA-TT** based OTFTs. Si wafer functions as the gate electrode and a thermally grown SiO_2 layer (~300 nm) on top of the Si layer was used as the insulating dielectric. After encapsulation with PMMA, the devices were tested under ambient condition using an Agilent 4155C Semiconductor Analyzer.

3.6.3 Synthesis procedures

Synthesis of 1-bromotridecan-2-one (6a)[89]: Bromine (4.66 mL, 90.45 mmol, 1.0 equiv.) was added dropwise to a solution of 2-tridecanone (17.88g, 90.16 mmol, 1.0 equiv.) in methanol (150 mL) at -10 ^oC with stirring. The mixture was stirred for 1 h at 0 ^oC and then 1 h at room temperature. Water (27 mL) and concentrated sulfuric acid (98% wt, 49 mL) was added to the mixture at 0 ^oC. After the mixture was stirred overnight at room temperature, white precipitates were collected by suction filtration and washed with water. The solid was then dried in under vacuum at35 ^oC for 1 h: 19.32 g (77 % yield). ^1H NMR (300 MHz, $CDCl_3$) δ 3.87 (s, 2H), 2.63 (t, *J* = 7.4 Hz, 2H), 1.67 – 1.56 (m, 2H), 1.25 (s, 16H), 0.87 (t, *J* = 6.5 Hz, 3H). ^{13}C NMR (75 MHz, $CDCl_3$) δ 202.02, 39.69, 34.16, 31.77, 29.45, 29.30, 29.19, 28.91, 23.74, 22.54, 13.96.

Synthesis of 1-bromo-5-hexyltridecan-2-one (6b): 6b was prepared according to procedure described above for the preparation of **6a**. Pure material was isolated by column chromatography on silica gel (hexane:dichloromethane, 2:1) in 35 % yield. ^1H NMR (300 MHz, $CDCl_3$): δ 3.87 (s, 2H), 2.60 (t, J= Hz, 2H), 1.55 (q, J= Hz, 2H), 1.13-1.32 (m, 25H), 0.86 (t, J= Hz, 6H). ^1H NMR (300 MHz, $CDCl_3$) δ 3.87 (s, 2H), 2.60(t, *J* = 7.8 Hz, 2H), 1.61 – 1.53 (m, 2H), 1.24 (s, 15H), 0.86 (t, *J* = 6.3 Hz, 6H). ^{13}C NMR (75 MHz, $CDCl_3$) δ 202.61, 37.32, 36.96, 34.26, 33.36, 31.92, 31.89, 30.05, 29.71, 29.63, 29.34, 27.61, 26.57, 26.54, 22.69, 14.11.

Synthesis of 1,2-bis(4-undecylthiazol-2-yl)diazene (7a):[90] Compound **6a** (19.32 g, 69.69 mmol, 2.0 equiv.) and hydrazine-1,2- bis(carbothioamide) (5.23 g, 34.84 mmol, 1.0 equiv.) were heated in ethanol (15 mL) at 50 ^oC for 3 h under Ar. The mixture was then cooled to rt and left to sit overnight. The white solid was collected by suction filtration, washed with ethanol and dried. $NaNO_2$ (2.40 g, 34.84 mmol, 1.0 equiv.) solution in 80 mL of water is added dropwise into the dispersion of the white solid in 500 mL of water. The white dispersion turned yellow immediately and then to orange. The mixture was stirred for 2 h after the addition of $NaNO_2$

solution. Orange solid was collected by suction filtration and recrystallized from toluene-methanol to yield 9.9554 g (78 %) of orange crystals. ^{1}H NMR (300 MHz, $CDCl_3$) δ 7.11 (s, 2H), 2.85 (t, *J* = 7.6 Hz, 4H), 1.95 – 1.69 (m, 4H), 1.69 – 1.08 (m, 32H), 0.85 (t, *J* = 6.3 Hz, 6H). ^{13}C NMR (75 MHz, $CDCl_3$) δ 174.04, 160.24, 118.01, 31.79, 31.77, 29.49, 29.48, 29.41, 29.26, 29.19, 29.11, 28.97, 22.54, 13.97.

Synthesis of 1,2-bis(4-(3-hexylundecyl)thiazol-2-yl)diazene (7b). Compound **6b** (1.38 g, 3.82mmol, 2.0 equiv.) and hydrazine-1,2- bis(carbothioamide) (0.287 g, 1.91 mmol, 1.0 equiv.) were heated in ethanol (6 mL) at 50 °C for 2.5 h under Ar. The mixture was then cooled to rt and stirred overnight. Ethyl acetate was then added into the mixture to precipitate a white solid. The white sticky solid was then collected by suction filtration, washed with small amount of ethanol and ethyl acetate, and briefly dried. The resulting solid was then stirred in 20 mL of ethyl acetate and 40 mL of water. An aqueous solution of $NaNO_2$ (0.13 g, 1.91 mmol, 1.0 equiv.) was added dropwise into the reaction mixture. The reaction was stopped when no white solid was observed (approx. 1 h.). The two layers were separated and the aqueous layer was extracted by ethyl acetate. The combined organics were dried over $MgSO_4$, filtered and solvent removed under reduced pressure. The residue was purified through column chromatography on silica gel (hexane:dichloromethane, 2:1) to give an orange solid (0.73g, 75 %). ^{1}H NMR (300 MHz, $CDCl_3$) δ 7.14 (s, 2H), 2.86 (t, *J* = 8.1Hz, 4H), 1.83 – 1.66 (m, 4H), 1.56 – 1.00 (m, 50H), 0.88 (t, *J* = 6.4 Hz, 12H). ^{13}C NMR (75 MHz, $CDCl_3$) δ 174.08, 160.67, 117.88, 37.10, 33.38, 33.04, 31.80, 30.00, 29.66, 29.54, 29.25, 26.51, 26.48, 22.58, 22.57, 14.00.

Synthesis of 1,2-bis(5-bromo-4-undecylthiazol-2-yl)diazene (8a):[91,92] Compound **7a** (1.50 g, 2.97 mmol, 1.0 equiv.) was dissolved in 80 mL of chloroform and cooled in an ice-water bath. A bromine (0.95 g, 5.94 mmol, 2.0 equiv.) solution in chloroform (20 mL) was added dropwise at 0 °C in the dark. The reaction was monitored by TLC. The mixture was stirred for extra 5 min after addition of bromine solution. The reaction mixture was then poured into 50 mL of saturated $NaHCO_3$ solution, and the two layers were separated. The aqueous was extracted with DCM (2×50 mL). The combined organics was washed with dilute $Na_2S_2O_3$ solution (50 mL), dried over Na_2SO_4, filtered and concentrated under reduced pressure. The residue was purified through column chromatography on silica gel (hexane/toluene 2:1) to yield an orange solid (0.74 g, 38 %). ^{1}H NMR (300 MHz, CDCl$_3$) δ 2.85 (t, *J* = 7.6 Hz, 4H), 1.79 (quint, *J* = 6.9 Hz, 4H), 1.18-1.41 (m, 32H), 0.85 (t, *J* = 6.6 Hz, 6H). ^{13}C NMR (75 MHz, CDCl$_3$) δ 172.35, 159.12, 113.18, 31.79, 29.77, 29.50, 29.40, 29.22, 29.08, 28.47, 22.56, 13.99.

Synthesis of 1,2-bis(5-bromo-4-(3-hexylundecyl)thiazol-2-yl)diazene (8b): 8b was prepared from **7b** according to the procedure described above for the preparation of **8a**. Pure material was isolated by column chromatography on silica gel (hexane:toluene, 3:1) in 28 % yield. ^{1}H NMR (300 MHz, CDCl$_3$) δ 2.83(t, *J* = 8.1 Hz, 4H), 1.73 (m, 4H), 1.17-1.43 (m, 32H), 0.88 (t, *J* = 6.1 Hz, 12H). ^{13}C NMR (75 MHz, CDCl$_3$) δ 172.52, 159.66, 113.20, 37.27, 33.43, 32.43, 31.94, 30.12, 29.78, 29.69, 29.39, 27.39, 26.59, 22.72, 14.15.

Synthesis of PDTA-T. A 100 mL heat gun-dried two-neck round bottom flask was charged with **8a** (0.331 g, 0.5 mmol, 1.0 equiv.), 2,5-bis(trimethylstannyl)thiophene (0.205 g, 0.5 mmol, 1.0 equiv.) and tri(*o*-tolyl)phosphine (0.012 g, 0.04 mmol, 0.08 equiv.) and equipped with a water condenser. The vessel was vacuumed and refilled with Ar three times. Anhydrous chlorobenzene (10 mL) was injected through a septum, and tris(dibenzylideneacetone)dipalladium (9.2 mg, 0.01 mmol, 0.02 equiv.) was added. The reaction mixture was then heated at 90 °C under argon atmosphere for 72 h. 0.5 mL of bromobenzene was added, and the reaction mixture was heated for another 12 h at 90 °C. After cooled down to rt, the reaction mixture was pipetted into a 400 mL beaker containing 150 mL of stirring acetone. The polymer was collected by filtration (black/deep red filtrate) and purified through Soxhlet extraction using methanol, acetone, hexane and dichloromethane and then dissolved in chloroform. Yield: 0.0799 g (27 % yield).

Synthesis of PDTA-BT: PDTA-BT was prepared using via Stille-coupling of **8b** with 5,5'-bis(trimethylstannyl)-2,2'-bithiophene according the procedure described above. The polymer was purified by Soxhlet extraction using methanol, acetone, hexane, and dichloromethane and then dissolved with chloroform (0.182 g, 62 %).

Synthesis of PDTA-BTV: A 100 mL heat gun-dried two-neck round bottom flask was charged with **8a** (0.132 g, 0.2 mmol, 1.0 equiv.) and (E)-((4-dodecyl-5-(2-(3-dodecyl-5-(trimethylstannyl)thiophen-2-yl)vinyl)thiophen-2-yl)dimethylstannyl)methylium (0.171 g, 0.2

mmol, 1.0 equiv.) and equipped with a water condenser. The vessel was vacuumed and refilled with Ar three times. Anhydrous toluene (10 mL) was injected through a septum, and Bis(triphenylphosphine)palladium(II) dichloride (0.004 g, 0.006 mmol, 0.03 equiv.) was added. The reaction mixture was then heated for 65 h at 90 ^{o}C and 2 h at 110 ^{o}C. 0.5 mL of bromobenzene was then added and the reaction mixture was heated at 110 ^{o}C for 4 h. After cooled down, the mixture was transferred into a beaker containing 100 mL of MeOH with a pipette and solid collected by suction filtration. The polymer was then purified through Soxhlet extraction with methanol and hexane, then dissolved in chloroform. Yield: 0.0145 g (7% yield).

Synthesis of PDTA-TT: PDTA-TT was prepared using via stille-coupling of **8b** with 2,5-bis(trimethylstannyl)thieno[3,2-b]thiophene according the procedure described above. The polymer was purified by Soxhlet extraction using methanol, acetone, hexane, and dichloromethane and then dissolved with chloroform (0.187 g, 68 %).

Chaptor 4

Summary and Future Work

Two novel electron-accepting building blocks, IBDF and DTA, were prepared and incorporated into D-A copolymers. Both are reported for the first time to make D-A copolymers. Two copolymers of IBDF and thiophene, **P6-IBDF-T** and **P6-IBDF-T**, were reported. Homopolymer of IBDF, **P6-IBDF** was also synthesized and characterized. DTA was copolymerized with thiophene, bithiophene, bithiophene vinylene, and thienothiophene to afford **PDAT-T**, **PDTA-BT**, **PDTA-BTV** and **PDTA-TT**, respectively.

P6-IBDF-T showed good solution processability and exhibited characteristic n-type semiconductor performance in encapsulated OTFTs with electron mobility as high as 5.4 ×10^{-3} $cm^2V^{-1}s^{-1}$ even though the polymer films are rather disordered. The non-encapsulated devices exhibited ambipolar charge transport behaviour with balanced electron/hole mobilities up to 8.2 ×10^{-3}/1.0 ×10^{-2} $cm^2V^{-1}s^{-1}$. These values are impressive considering the amorphousness of P6-IBDF-T thin films. In spite of its low molecular weight, the homopolymer of IBDF, **P6-IBDF**, showed typical n-type characteristics with electron mobility up to 2 ×10^{-4} $cm^2V^{-1}s^{-1}$. Our preliminary results demonstrated that IBDF is potentially a promising electron acceptor building block for polymer semiconductors. Side chain engineering of **P6-IBDF-BT** and synthesis of other IBDF copolymers with better solubility and crystallinity will be key in future research to improve the charge transport performance of this new class of polymers.

The effect of conjugation on the charge carrier mobility of polymer semiconductors was studied by comparing **P5-IBDF-T** with **P6-IBDF-T**. **P5-IBDF-T**, with lower degree of conjugation showed mobilities two order of magnitude lower than that of **P6-IBDF-T**. The insufficient interaction of donor and acceptor in **P5-IBDF-T** also leads to uneven electron distribution in HOMO and LUMO, which accounts for the smaller energy bandgap and weak absorption over visible-NIR range. Conclusion can be drawn from these observations that copolymerization of IBDF at 5-position is inferior to 6-postion in terms of conjugation.

All DTA based D-A copolymers required low to moderate thermal treatment. As the area of electron donor increased from T in **PDTA-T** to BTV in **PDTA-BTV**, the mobility of the semiconductor increased, and the charge transport property shift from n-type to p-type. **PDAT-T** showed the highest electron mobility of 4 $\times 10^{-4}$ $cm^2V^{-1}s^{-1}$ for 150 ^oC-annealed films. Non-annealed and 100 ^oC-annealed **PDTA-BT** thin film showed hole mobility of 9 $\times 10^{-4}$ $cm^2V^{-1}s^{-1}$ or higher. Non-annealed **PDTA-TT** film showed hole mobility as high as 9.9 $\times 10^{-4}$ $cm^2V^{-1}s^{-1}$. With comparable donor and acceptor areas, **PDTA-BTV** exhibited mobilities of 10^{-3} $cm^2V^{-1}s^{-1}$ on OTFTs with non-annealed and 100 ^oC-annealed thin films. The low processing temperature (lower than 150 ^oC) of DTA based D-A copolymers and their instability at higher temperature can be attractive for feasible manufacturing of disposable electronics. In addition, DTA based polymer semiconductors showed ultra-small bandgap between 1.18 – 1.27 eV. Therefore, although these polymer semiconductors are not suitable for OTFTs applications seeking high charge carrier mobility, they are promising candidates for OPV applications such as light sensor, where a small bandgap and a broad absorption over the visible light range are more important than charge carrier mobility.

Appendix A

Additional data

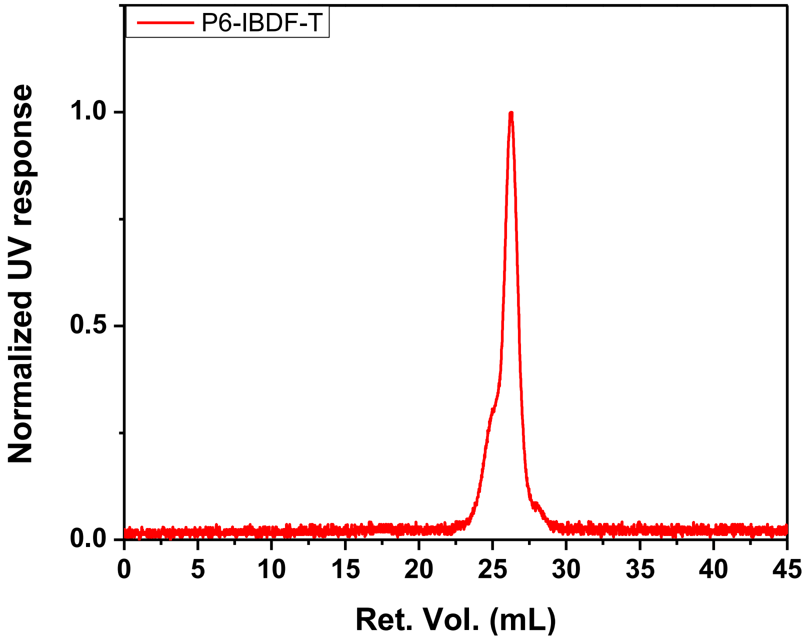

Figure A-1. GPC elution curve of **P6-IBDF-T** using 1,2,4-trichlorobenzene as eluent at a column temperature of 140 ℃.

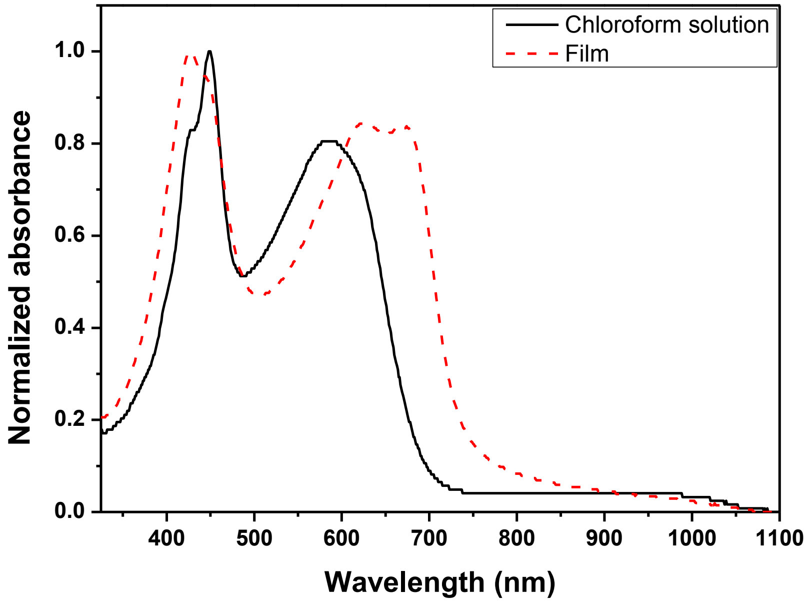

Figure A-2. UV-vis-NIR absorption spectra of 6-Br-IBDF (**2**) in chloroform and in a thin film.

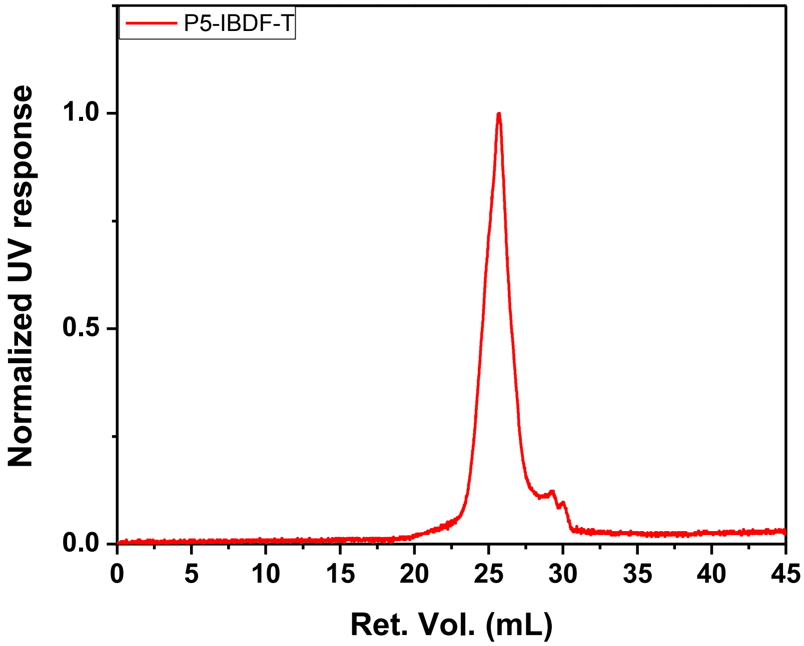

Figure A-3. GPC elution curve of **P5-IBDF-T** using 1,2,4-trichlorobenzene as eluent at a column temperature of 140 ℃.

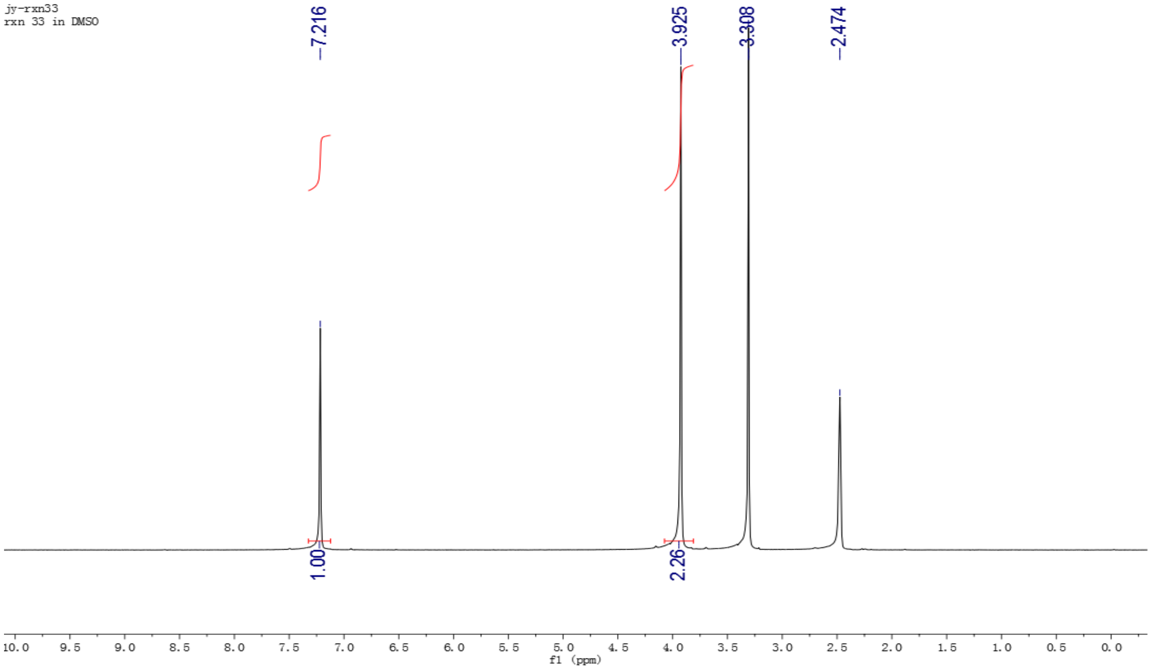

Figure A-4. 300 MHz ^{1}H NMR spectrum for benzo[1,2-*b*:4,5-*b*']difuran-2,6(3*H*,7*H*)-dione in DMSO-d_6. – Reproduced by permission of The Royal Society of Chemistry

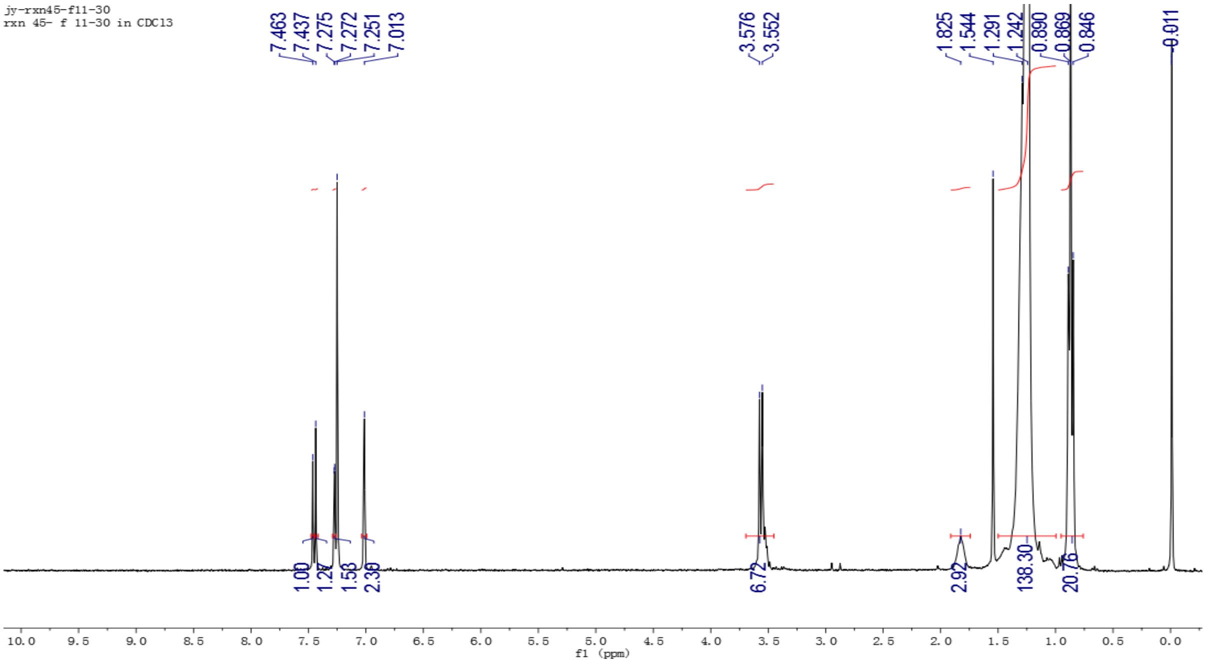

Figure A-5. 300 MHz ^{1}H NMR spectrum for 6-bromo-1-(2-decyltetradecyl)indoline-2,3-dione (**1**). – Reproduced by permission of The Royal Society of Chemistry

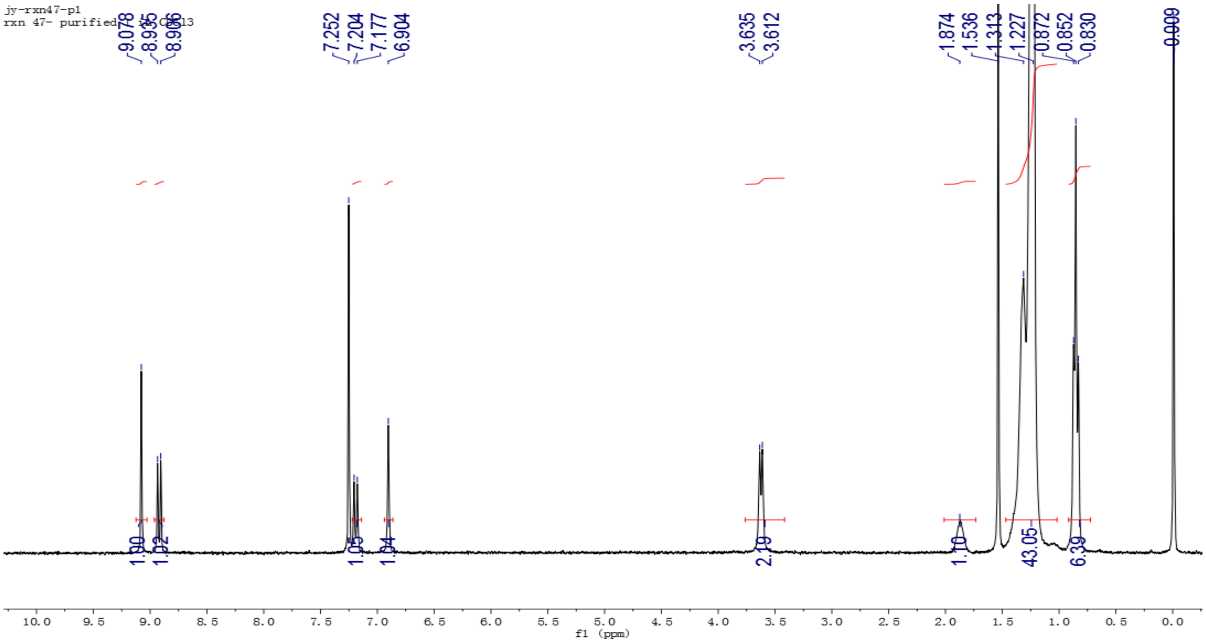

Figure A-6. 300 MHz ^1H NMR spectrum for (3*E*,7*E*)-3,7-bis(6-bromo-1-(2-decyltetradecyl)-2-oxoindolin-3-ylidene)benzo[1,2-*b*:4,5-*b*']difuran-2,6(3*H*,7*H*)-dione (**2**). – Reproduced by permission of The Royal Society of Chemistry

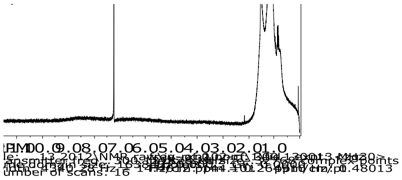

Figure A-7. 300 MHz ^1H NMR spectrum of **P6-IBDF-T** in $CDCl_3$. – Reproduced by permission of The Royal Society of Chemistry

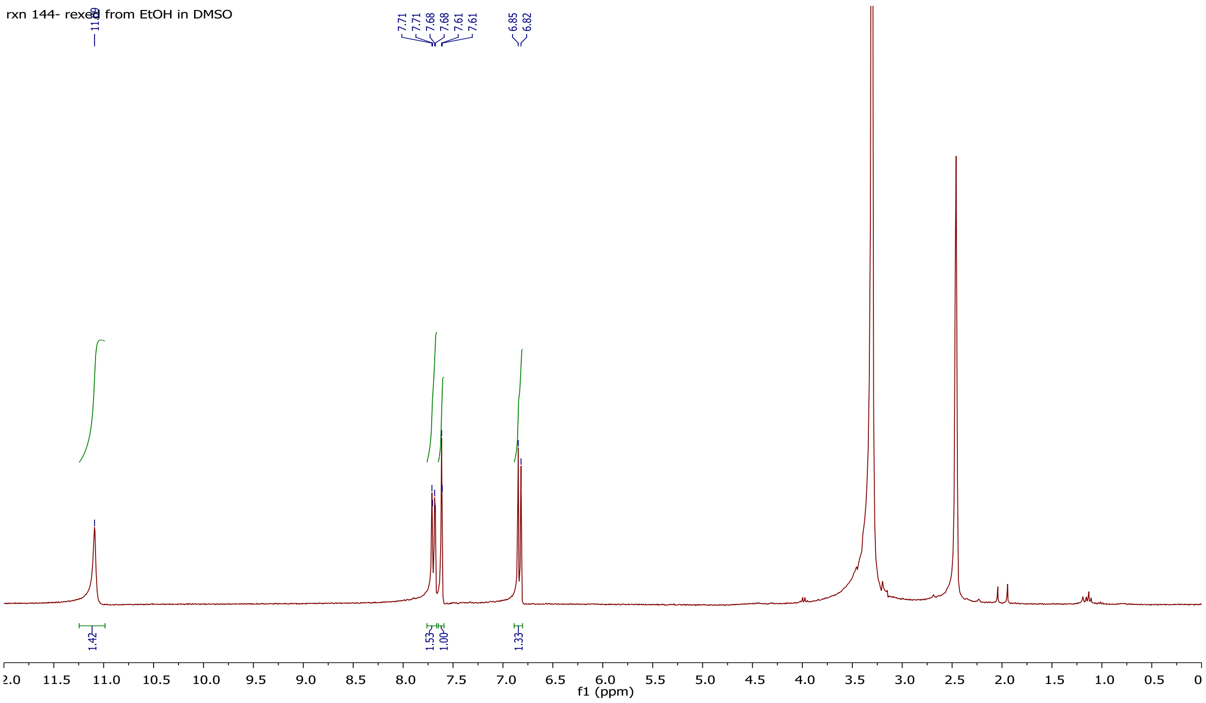

Figure A-8. 300 MHz ^{1}H NMR spectrum for 5-bromoindoline-2,3-dione (**3**) in $CDCl_3$**.**

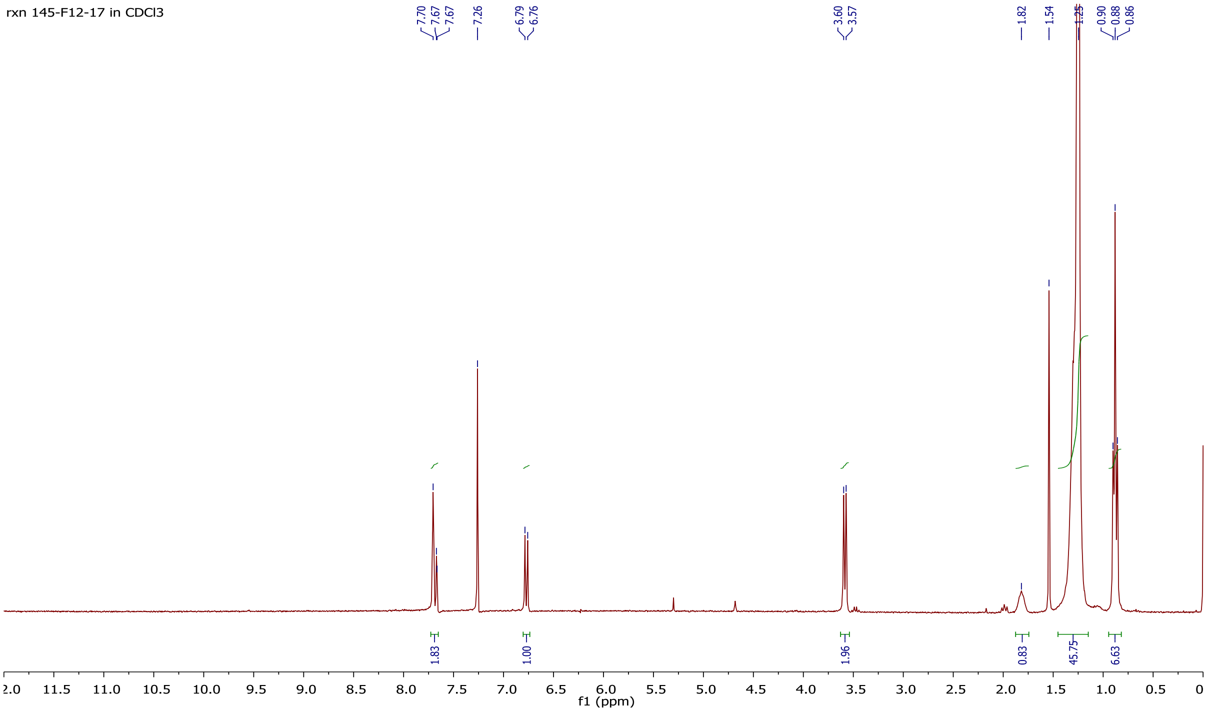

Figure A-9. 300 MHz ^{1}H NMR spectrum for 5-bromo-1-(2-decyltetradecyl)indoline-2,3-dione (**4**) in $CDCl_3$.

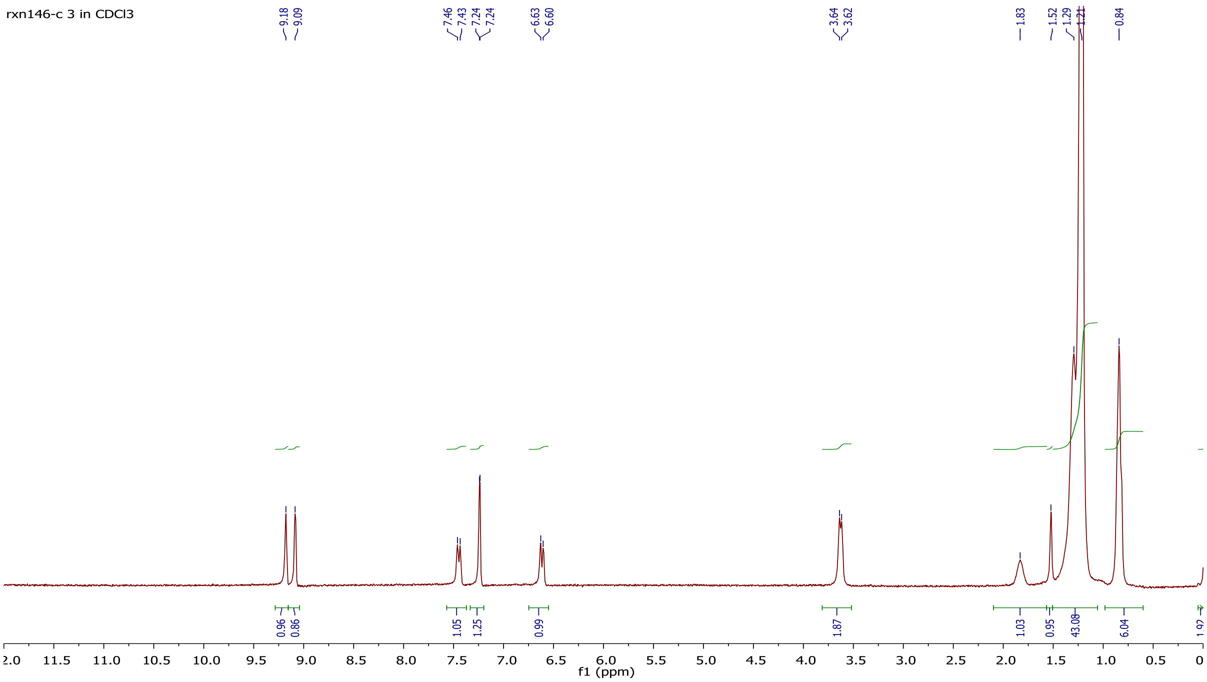

Figure A-10. 300 MHz ^{1}H NMR spectrum for (3E,7E)-3,7-bis(5-bromo-1-(2-decyltetradecyl)-2-oxoindolin-3-ylidene)benzo[1,2-b:4,5-b']difuran-2,6(3H,7H)-dione (**5**) in $CDCl_3$.

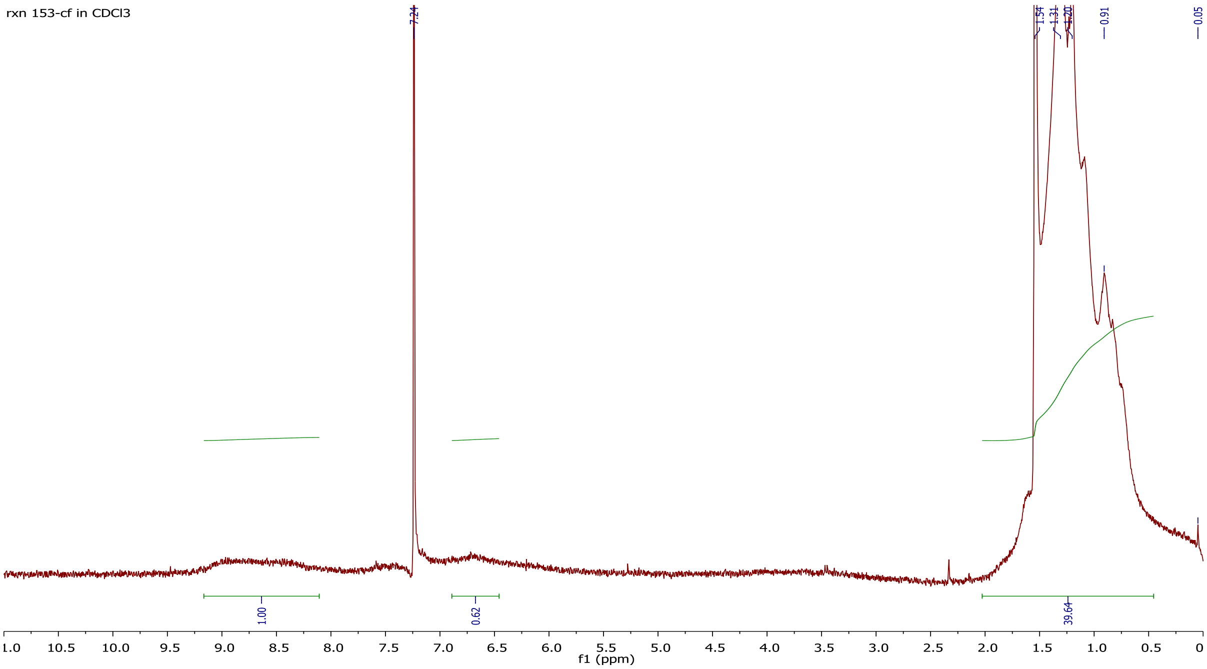

Figure A-11. 300 MHz ^{1}H NMR spectrum for **P5-IBDF-T** in $CDCl_3$.

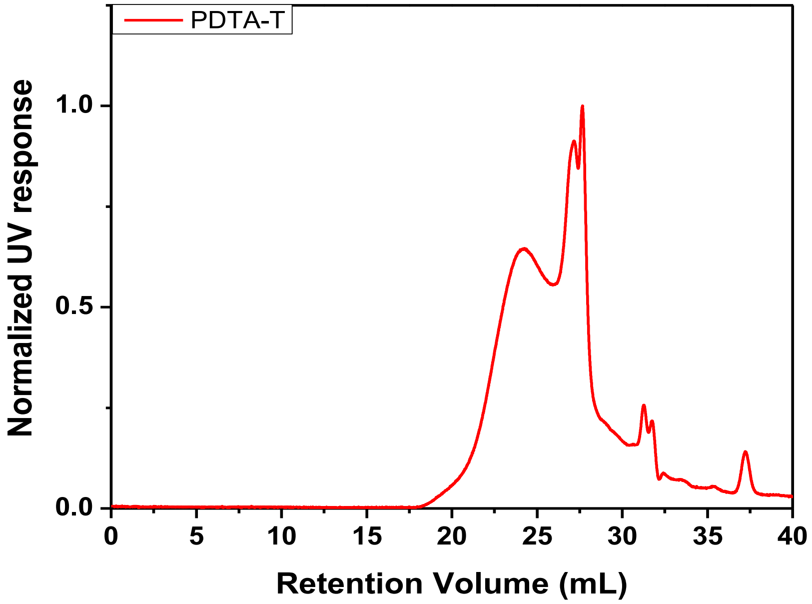

Figure A-12. GPC elution curve of **PDTA-T** using THF as eluent at a column temperature of 40 ℃.

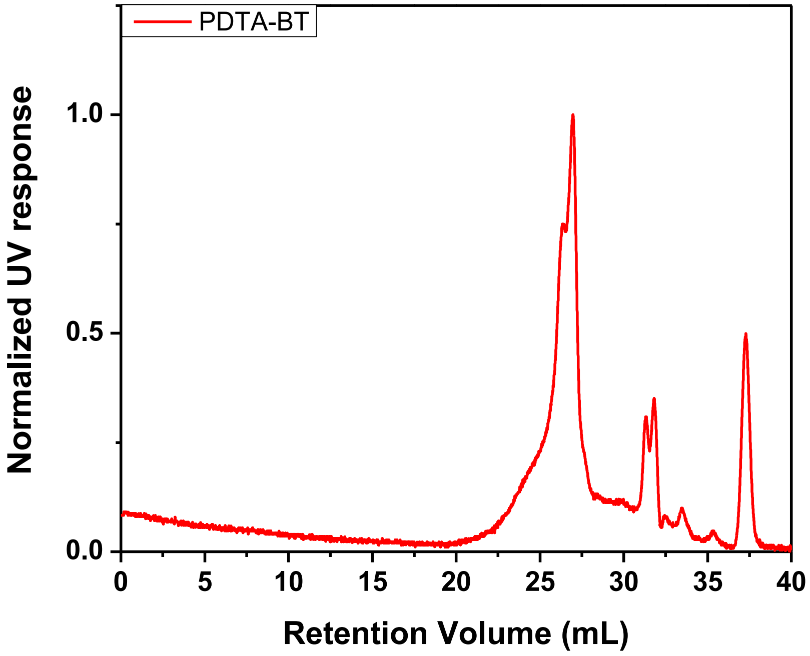

Figure A-13. GPC elution curve of **PDTA-BT** using THF as eluent at a column temperature of 40 ℃.

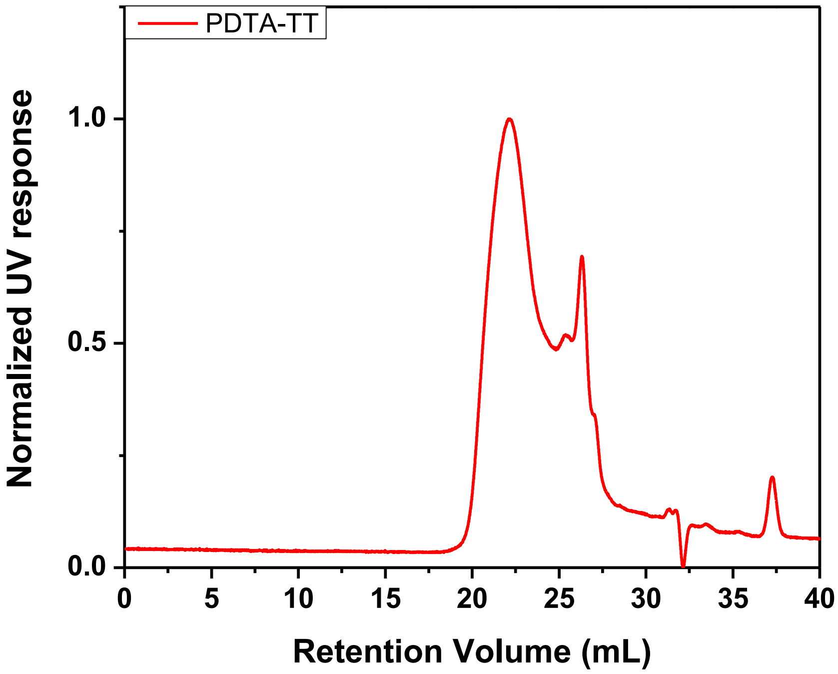

Figure A-14. GPC elution curve of **PDTA-TT** using THF as eluent at a column temperature of 40 ℃.

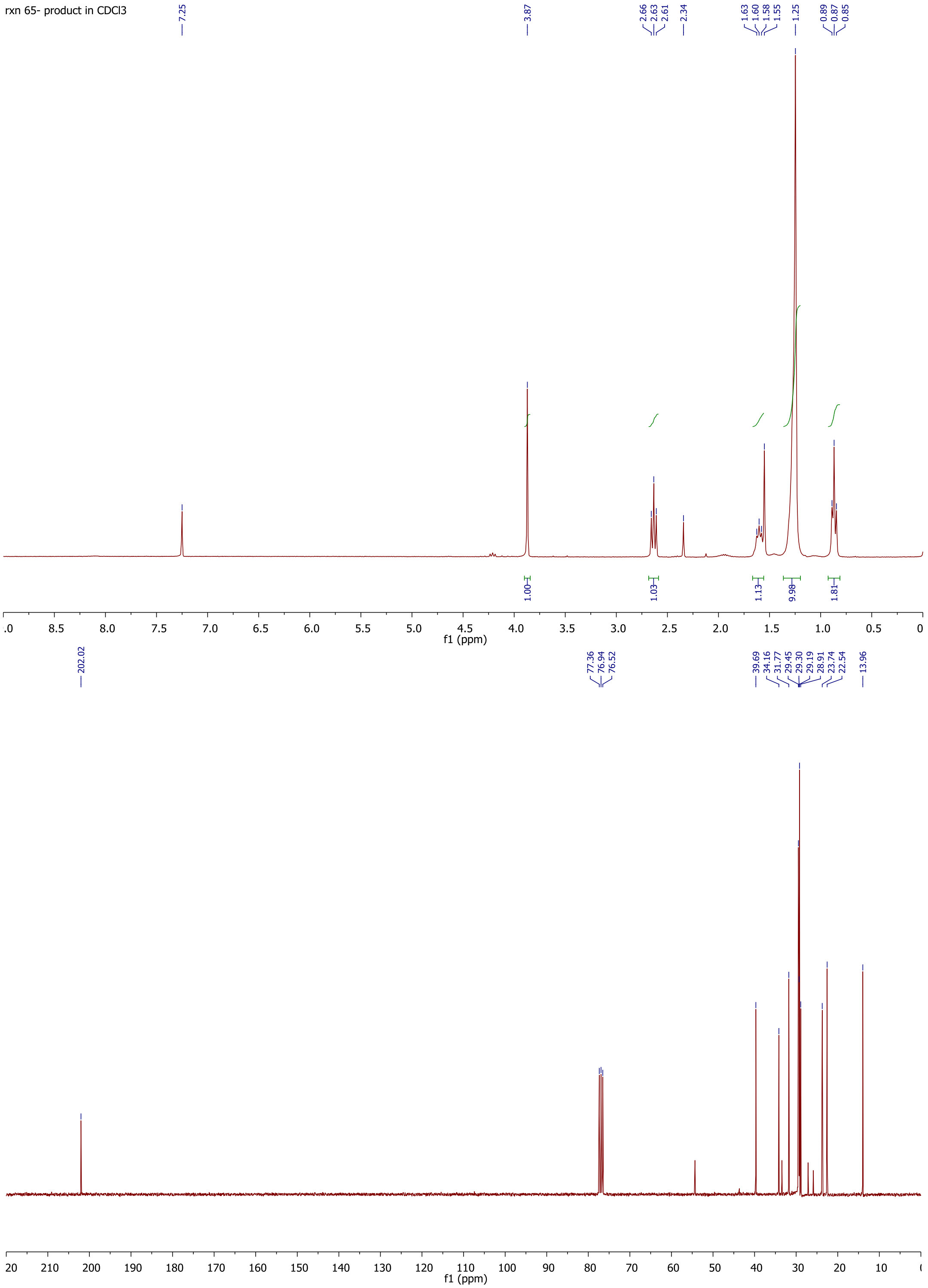

Figure A-15. (a) 300 MHz ^{1}H NMR spectrum and (b) 75 MHz ^{13}C NMR spectrum for 1-bromotridecan-2-one **(6a)** in $CDCl_3$**.**

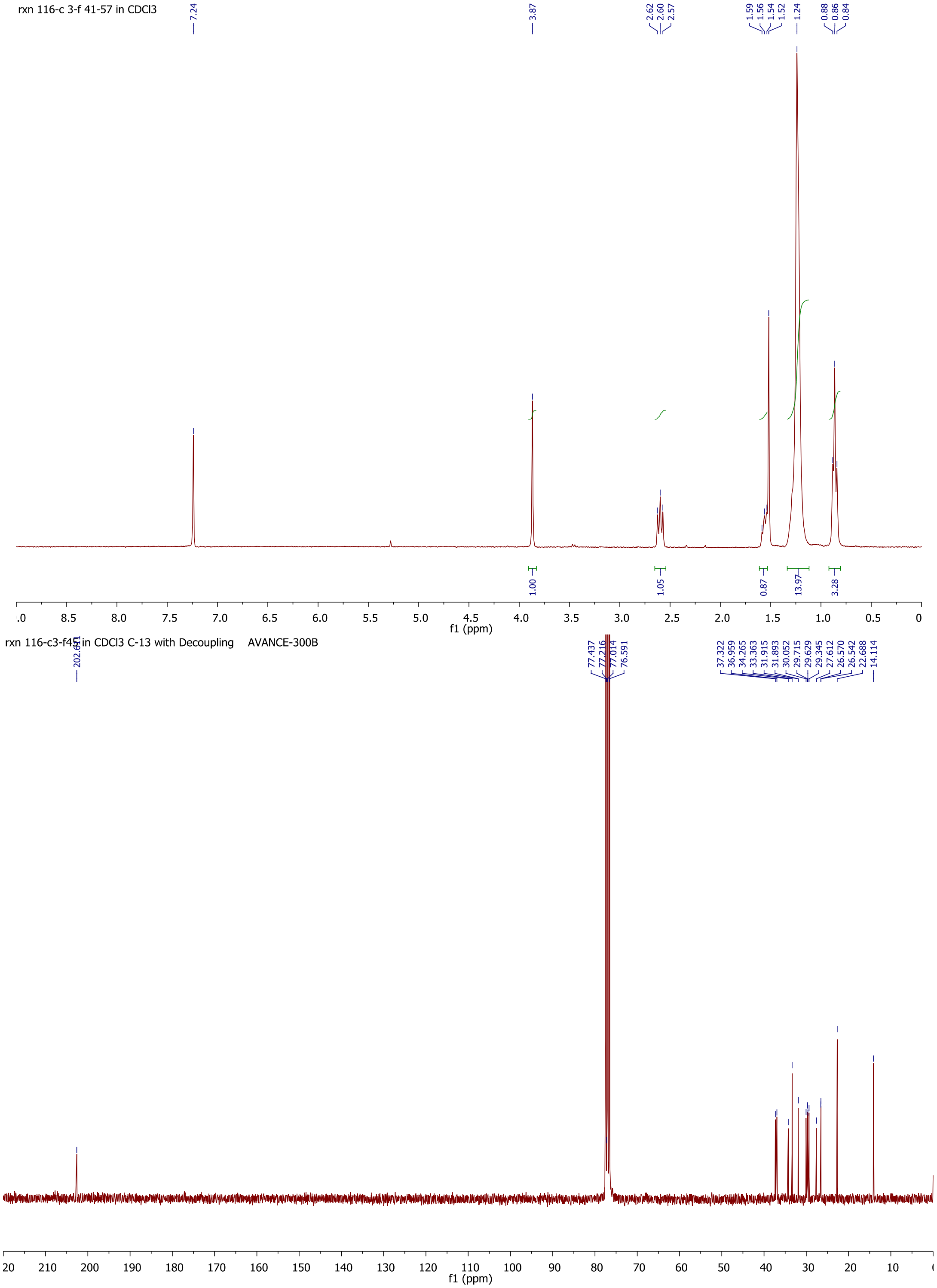

Figure A-16. (a) 300 MHz ^{1}H NMR spectrum and (b) 75 MHz ^{13}C NMR spectrum for 1-bromo-5-hexyltridecan-2-one **(6b)** in $CDCl_3$**.**

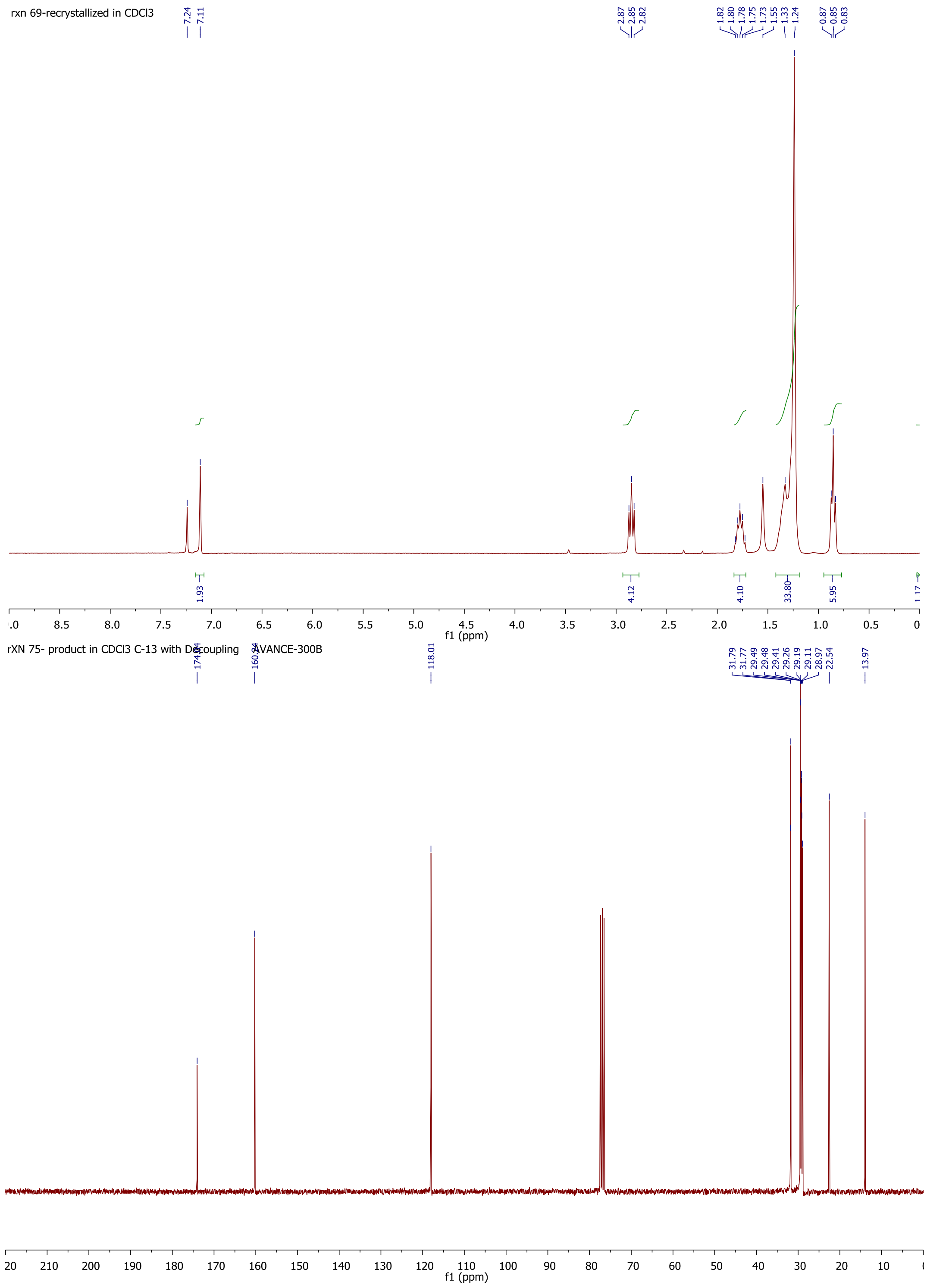

Figure A-17. (a) 300 MHz ^{1}H NMR spectrum and (b) 75 MHz ^{13}C NMR spectrum for 1,2-bis(4-undecylthiazol-2-yl)diazene **(7a)** in $CDCl_3$**.**

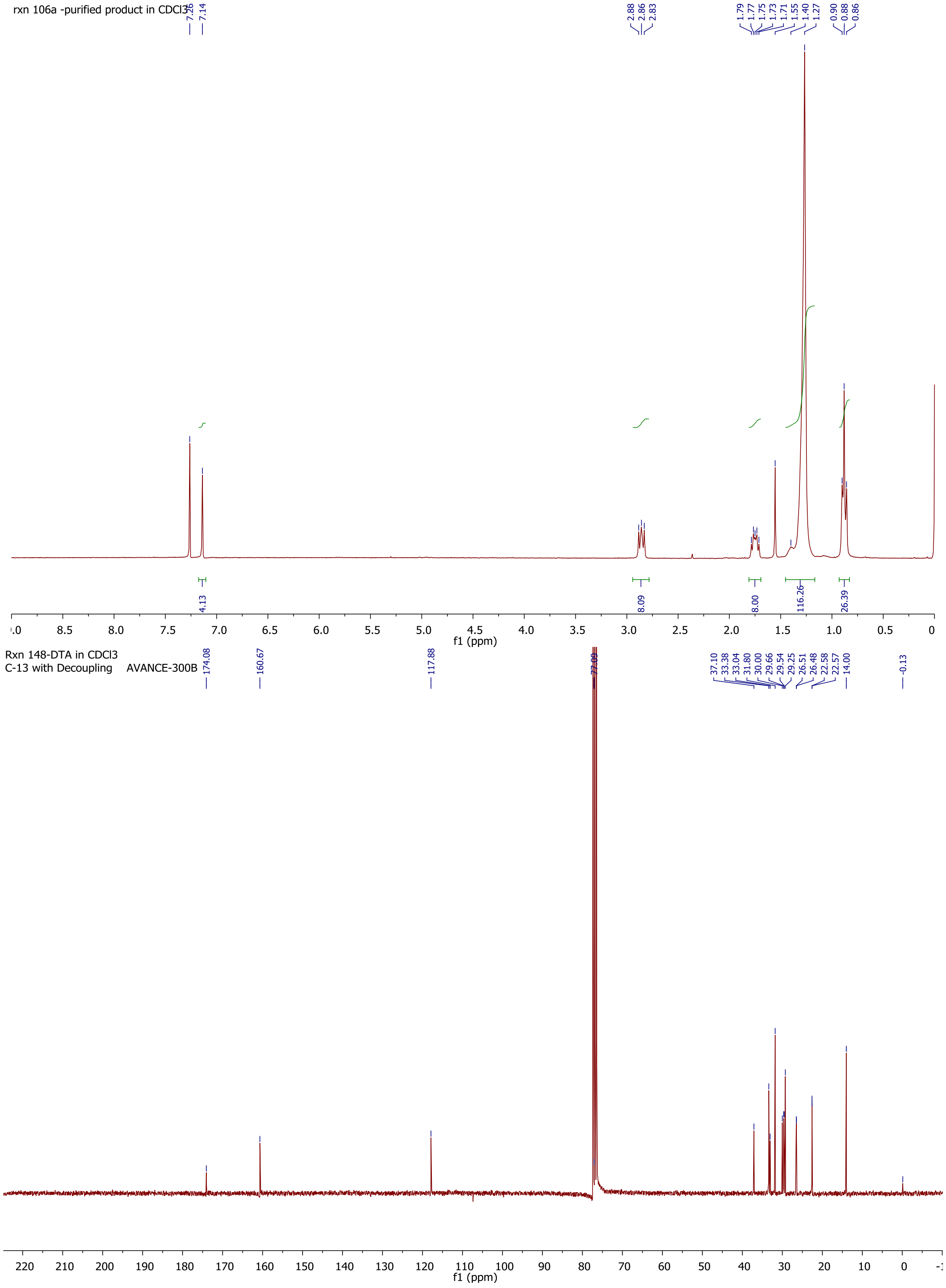

Figure A-18. (a) 300 MHz ^{1}H NMR spectrum and (b) 75 MHz ^{13}C NMR spectrum for 1,2-bis(4-(3-hexylundecyl)thiazol-2-yl)diazene **(7b)** in $CDCl_3$**.**

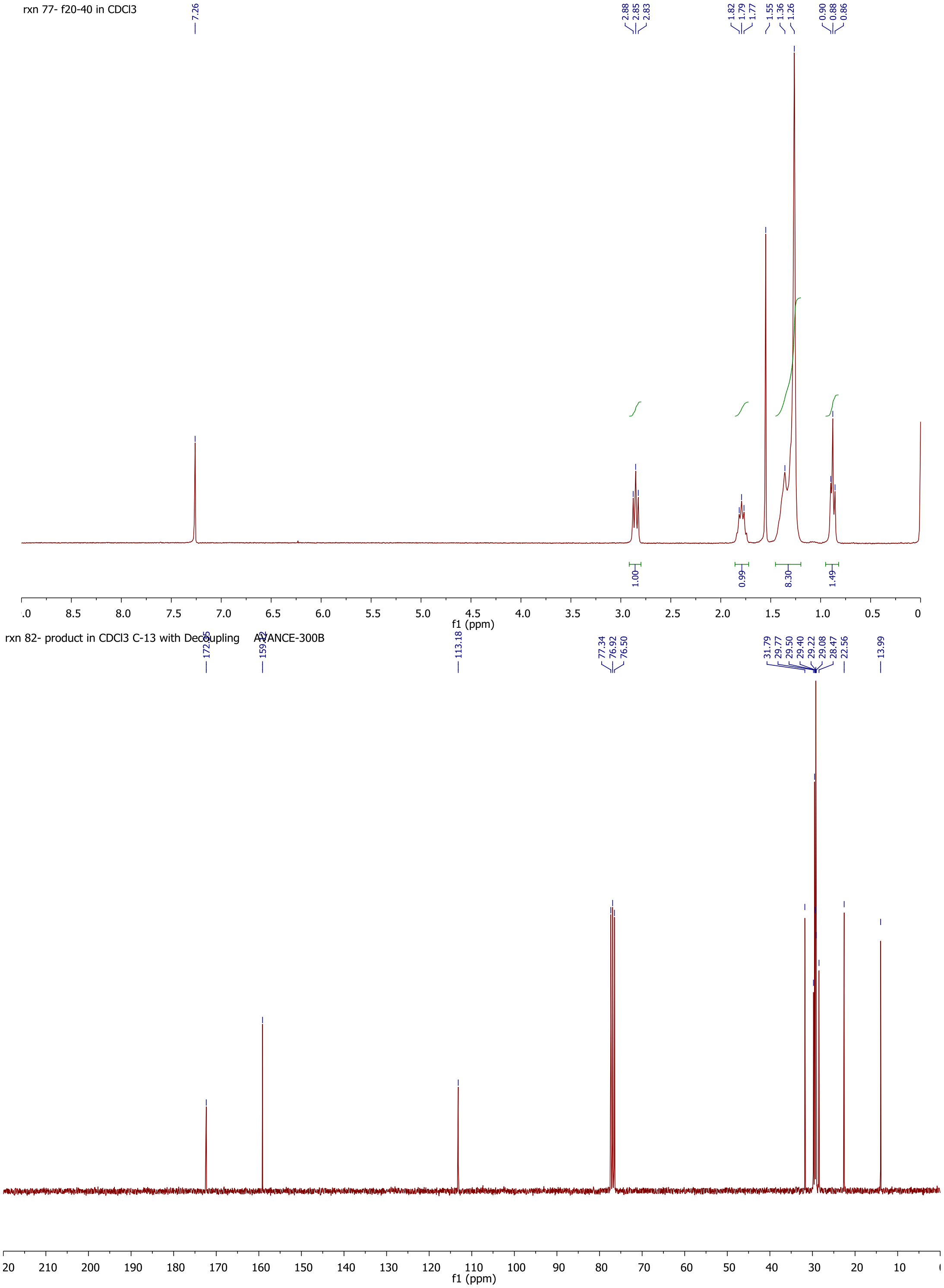

Figure A-19. (a) 300 MHz ^{1}H NMR spectrum and (b) 75 MHz ^{13}C NMR spectrum for 1,2-bis(5-bromo-4-undecylthiazol-2-yl)diazene **(8a)** in $CDCl_3$**.**

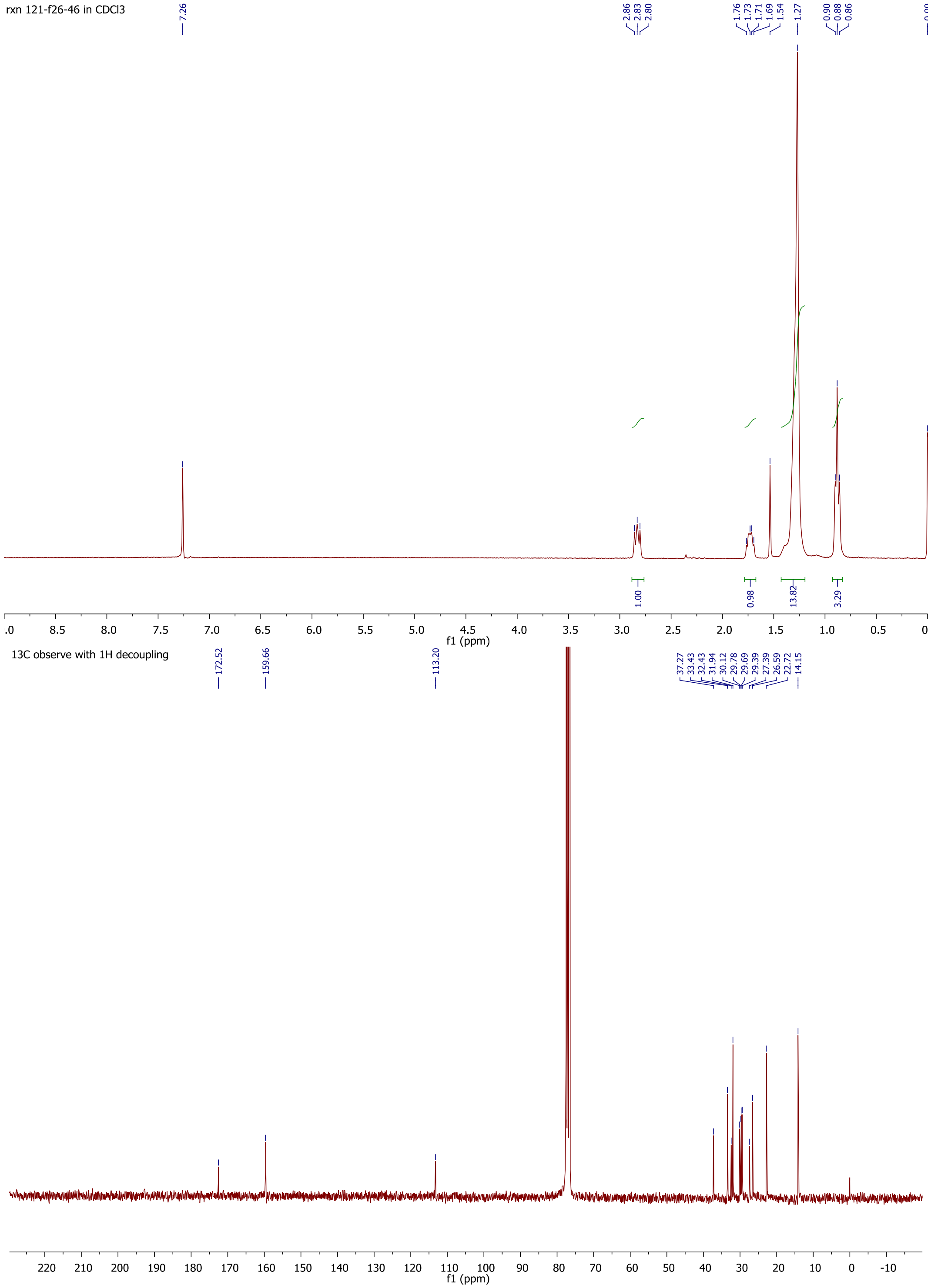

Figure A-20. (a) 300 MHz ^{1}H NMR spectrum and (b) 75 MHz ^{13}C NMR spectrum for 1,2-bis(5-bromo-4-(3-hexylundecyl)thiazol-2-yl)diazene **(8b)** in $CDCl_3$**.**

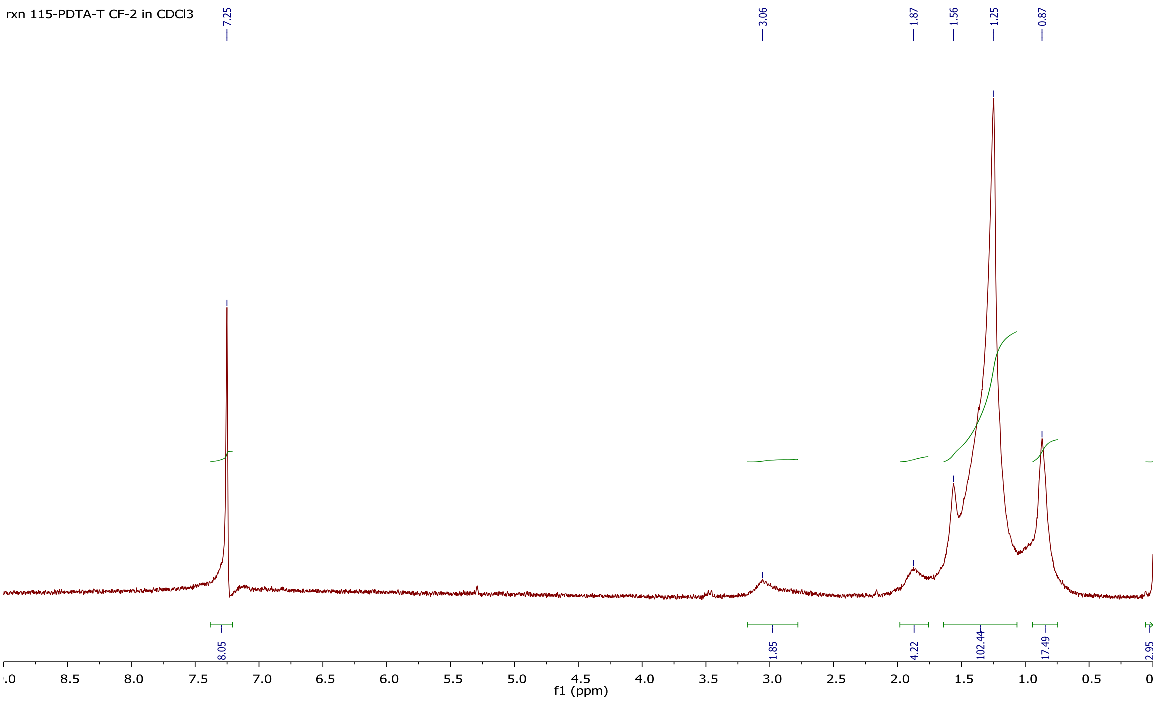

Figure A-21. 300 MHz ^{1}H NMR spectrum of **PDTA-T** in $CDCl_3$.

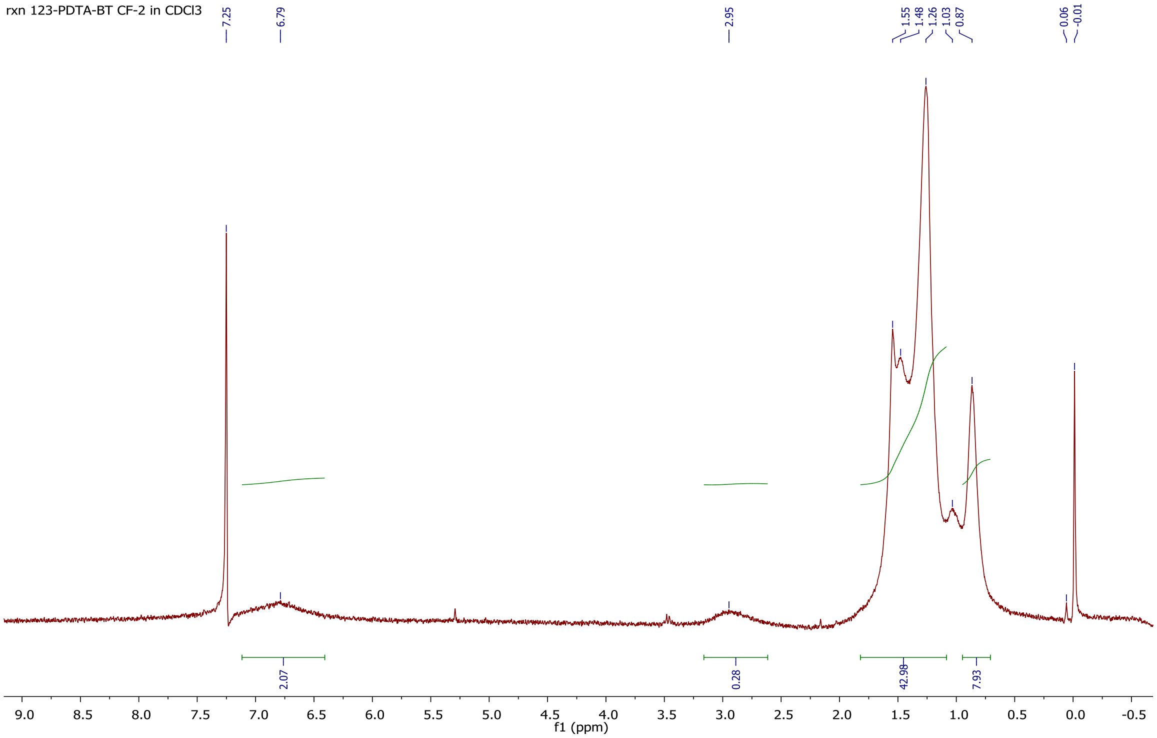

Figure A-22. 300 MHz ^{1}H NMR spectrum of **PDTA-BT** in $CDCl_3$.

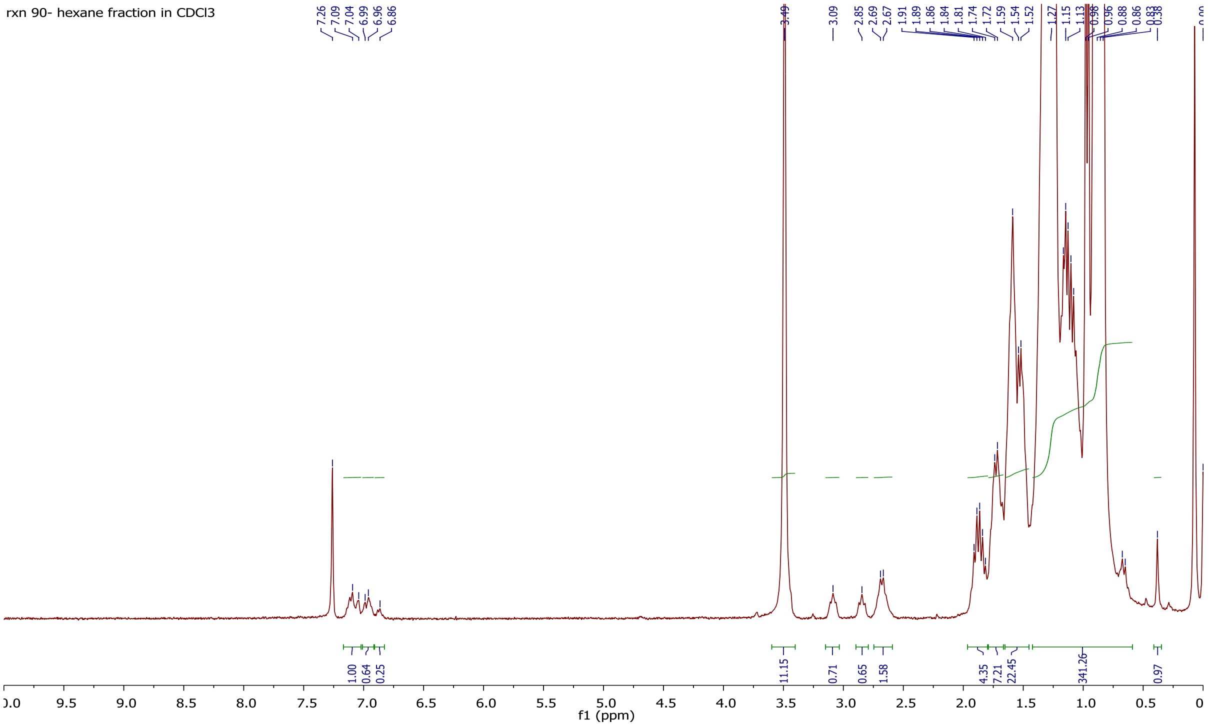

Figure A-23. 300 MHz ^{1}H NMR spectrum of **PDTA-BTV** in $CDCl_3$.

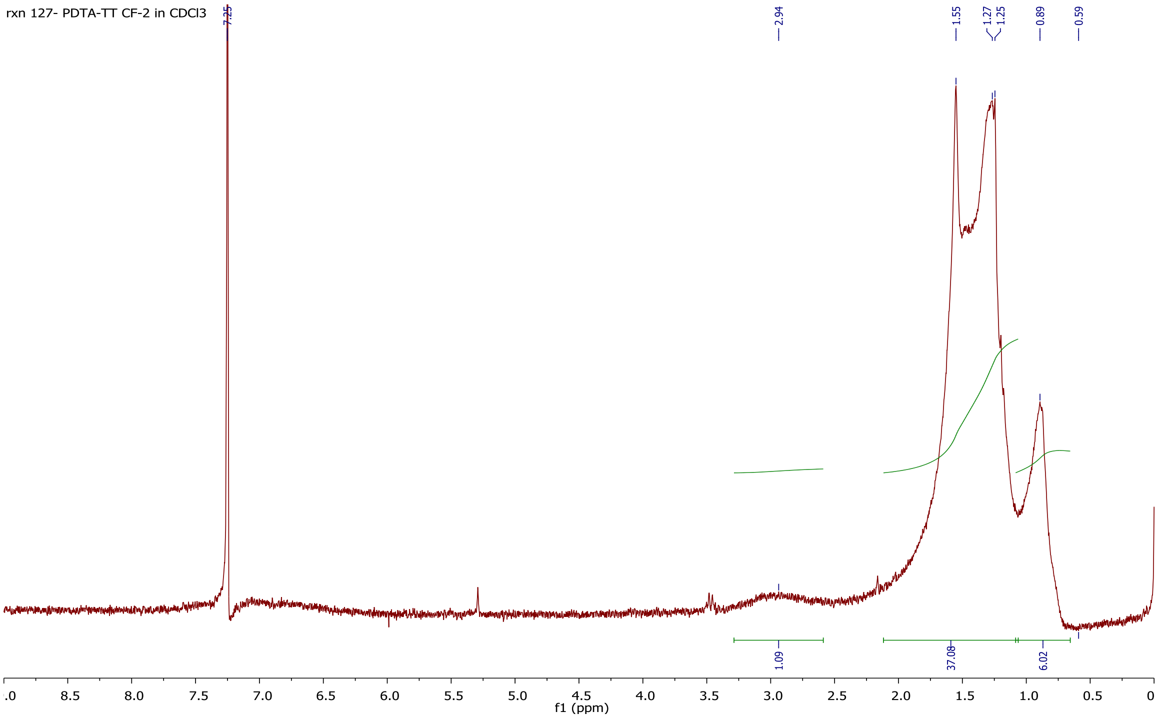

Figure A-24. 300 MHz ^{1}H NMR spectrum of **PDTA-TT** in $CDCl_3$.

Appendix B

Scientific Contributions

The following peer-reviewed publication is based on aspects of the work contained in this thesis:

- **Yan, Z.**; Sun, B.; and Li, Y. Novel stable (3E,7E)-3,7-bis(2-oxoindolin-3-ylidene)benzo[1,2-b:4,5-b']difuran-2,6(3H,7H)-dione based donor-acceptor polymer semiconductors for n-type organic thin film transistors, *Chemical communications (Cambridge, England)* **2013**, *49*, 3790–2.

Other peer-reviewed publications:

- Hong, W.; Guo, C.; Sun B.; **Yan, Z.**; Huang C.; Hu, Y.; Zheng, Y.; Facchetti A.; and Li, Y. Cyano-disubstituted dipyrrolopyrazinedione (CNPzDP) small molecules for solution processed n-channel organic thin-film transistors, *Journal of Materials Chemistry C*, **2013,** DOI: 10.1039/C3TC31274G.

Bibliography

(1) Forrest, S. R. *Nature* **2004**, *428*, 911–918.

(2) Lilienfeld, J. E. Method and apparatus for controlling electric currents. 1745175, 1930.

(3) Jang, J.; Han, S. H. *Current Applied Physics* **2006**, *6*, 17–21.

(4) Chandar Shekar, B.; Lee, J.; Rhee, S.-W. *Korean Journal of Chemical Engineering* **2004**, *21*, 267–285.

(5) Gelinck, G.; Heremans, P.; Nomoto, K.; Anthopoulos, T. D. *Advanced Materials* **2010**, *22*, 3778–98.

(6) Dimitrakopoulos, C. D.; Malenfant, P. R. L. *Advanced Materials* **2002**, *14*, 99–117.

(7) Tecklenburg, R.; Paasch, G.; Scheinert, S. *Advanced Materials for Optics and Electronics* **1998**, *8*, 285–294.

(8) Dimitrakopoulos, C. D.; Mascaro, D. J. *IBM Journal of Research and Development* **2001**, *45*, 11–27.

(9) Garnier, F. *Chemical Physics* **1998**, *227*, 253–262.

(10) Chiang, C. K.; Druy, M. A.; Gau, S. C.; Heeger, A. J.; Louis, E. J.; MacDiarmid, A. G.; Park, Y. W.; Shirakawa, H. *Journal of the American Chemical Society* **1978**, *100*, 1013–1015.

(11) Chiang, C.; Fincher, C.; Park, Y.; Heeger, A.; Shirakawa, H.; Louis, E.; Gau, S.; MacDiarmid, A. *Physical Review Letters* **1977**, *39*, 1098–1101.

(12) Shirakawa, H.; Louis, E. J.; MacDiarmid, A. G.; Chiang, C. K.; Heeger, A. J. *Journal of the Chemical Society, Chemical Communications* **1977**, 578.

(13) Zhang, H. W.; Song, Y. Q.; Tang, X. L.; Wang, L. G. *Materials Science Forum* **2011**, *687*, 222–227.

(14) Meisel, K. D.; Pasveer, W. F.; Cottaar, J.; Tanase, C.; Coehoorn, R.; Bobbert, P. a.; Blom, P. W. M.; de Leeuw, D. M.; Michels, M. a. J. *Physica Status Solidi (C)* **2006**, *3*, 267–270.

(15) Jaiswal, M.; Menon, R. *Polymer International* **2006**, *55*, 1371–1384.

(16) Athanasopoulos, S.; Kirkpatrick, J.; Mart ínez, D.; Frost, J. M.; Foden, C. M.; Walker, A. B.; Nelson, J. *Nano letters* **2007**, *7*, 1785–8.

(17) Br édas, J. L.; Calbert, J. P.; da Silva Filho, D. a; Cornil, J. *Proceedings of the National Academy of Sciences of the United States of America* **2002**, *99*, 5804–9.

(18) Li, Y.; Sonar, P.; Murphy, L.; Hong, W. *Energy & Environmental Science* **2013**, *6*, 1684.

(19) Ong, B. S.; Wu, Y.; Liu, P.; Gardner, S. *Journal of the American Chemical Society* **2004**, *126*, 3378–9.

(20) Takimiya, K.; Shinamura, S.; Osaka, I.; Miyazaki, E. *Advanced materials (Deerfield Beach, Fla.)* **2011**, *23*, 4347–70.

(21) Zhao, X.; Zhan, X. *Chemical Society Reviews* **2011**, *40*, 3728–43.

(22) Jones, B. a; Facchetti, A.; Wasielewski, M. R.; Marks, T. J. *Journal of the American Chemical Society* **2007**, *129*, 15259–78.

(23) Chen, H. Z.; Ling, M. M.; Mo, X.; Shi, M. M. *Chemistry of Materials* **2007**, *19*, 816–824.

(24) Li, Y.; Sun, B.; Sonar, P.; Singh, S. P. *Organic Electronics* **2012**, *13*, 1606–1613.

(25) Kanimozhi, C.; Yaacobi-Gross, N.; Chou, K. W.; Amassian, A.; Anthopoulos, T. D.; Patil, S. *Journal of the American Chemical Society* **2012**, *134*, 16532–16535.

(26) Bijleveld, J. C.; Zoombelt, A. P.; Mathijssen, S. G. J.; Wienk, M. M.; Turbiez, M.; de Leeuw, D. M.; Janssen, R. A. J. *Journal of the American Chemical Society* **2009**, *131*, 16616–7.

(27) Lee, J. S.; Son, S. K.; Song, S.; Kim, H.; Lee, D. R.; Kim, K.; Ko, M. J.; Choi, D. H.; Kim, B.; Cho, J. H. *Chemistry of Materials* **2012**, *24*, 1316–1323.

(28) Li, Y.; Sonar, P.; Singh, S. P.; Soh, M. S.; Meurs, M. van; Tan, J. *Journal of the American Chemical Society* **2011**, *133*, 2198–2204.

(29) Chen, H.; Guo, Y.; Yu, G.; Zhao, Y.; Zhang, J.; Gao, D.; Liu, H.; Liu, Y. *Advanced Materials* **2012**, *24*, 4618–4622.

(30) Li, Y.; Singh, S. P.; Sonar, P. *Advanced Materials* **2010**, *22*, 4862–4866.

(31) Li, J.; Zhao, Y.; Tan, H. S.; Guo, Y.; Di, C.-A.; Yu, G.; Liu, Y.; Lin, M.; Lim, S. H.; Zhou, Y.; Su, H.; Ong, B. S. *Scientific Reports* **2012**, *2*, 754.

(32) Li, Y.; Sonar, P.; Singh, S. P.; Zeng, W.; Soh, M. S. *Journal of Materials Chemistry* **2011**, *21*, 10829–10835.

(33) Li, Y.; Sonar, P.; Singh, S. P.; Ooi, Z. E.; Lek, E. S. H.; Loh, M. Q. Y. *Physical chemistry chemical physics : PCCP* **2012**, *14*, 7162–7169.

(34) Lin, H.-W.; Lee, W.-Y.; Chen, W.-C. *Journal of Materials Chemistry* **2012**, *22*, 2120.

(35) Ha, J. S.; Kim, K. H.; Choi, D. H. *Journal of the American Chemical Society* **2011**, *133*, 10364–10367.

(36) Shahid, M.; McCarthy-Ward, T.; Labram, J.; Rossbauer, S.; Domingo, E. B.; Watkins, S. E.; Stingelin, N.; Anthopoulos, T. D.; Heeney, M. *Chemical Science* **2012**, *3*, 181.

(37) Stalder, R.; Mei, J.; Reynolds, J. R. *Macromolecules* **2010**, *43*, 8348–8352.

(38) Lei, T.; Cao, Y.; Fan, Y.; Liu, C.-J.; Yuan, S.-C.; Pei, J. *Journal of the American Chemical Society* **2011**, *133*, 6099–101.

(39) Lei, T.; Cao, Y.; Zhou, X.; Peng, Y.; Bian, J.; Pei, J. *Chemistry of Materials* **2012**, *24*, 1762–1770.

(40) Lei, T.; Dou, J.-H.; Ma, Z.-J.; Yao, C.-H.; Liu, C.-J.; Wang, J.-Y.; Pei, J. *Journal of the American Chemical Society* **2012**, *134*, 20025–8.

(41) Lei, T.; Dou, J.-H.; Pei, J. *Advanced materials (Deerfield Beach, Fla.)* **2012**, *24*, 6457–61.

(42) Lei, T.; Dou, J.-H.; Ma, Z.-J.; Liu, C.-J.; Wang, J.-Y.; Pei, J. *Chemical Science* **2013**, *4*, 2447.

(43) Mei, J.; Kim, D. H.; Ayzner, A. L.; Toney, M. F.; Bao, Z. *Journal of the American Chemical Society* **2011**, *133*, 20130–3.

(44) Sonar, P.; Tan, H.-S.; Sun, S.; Lam, Y. M.; Dodabalapur, A. *Polymer Chemistry* **2013**, *4*, 1983.

(45) Lin, Y.; Fan, H.; Li, Y.; Zhan, X. *Advanced materials (Deerfield Beach, Fla.)* **2012**, *24*, 3087–106, 3081.

(46) Ando, S.; Murakami, R.; Nishida, J.; Tada, H.; Inoue, Y.; Tokito, S.; Yamashita, Y. *Journal of the American Chemical Society* **2005**, *127*, 14996–7.

(47) Paek, S.; Lee, J.; Lim, H. S.; Lim, J.; Lee, J. Y.; Lee, C. *Synthetic Metals* **2010**, *160*, 2273–2280.

(48) Liu, J.; Zhang, R.; Osaka, I.; Mishra, S.; Javier, A. E.; Smilgies, D.-M.; Kowalewski, T.; McCullough, R. D. *Advanced Functional Materials* **2009**, *19*, 3427–3434.

(49) Osaka, I.; Sauvé, G.; Zhang, R.; Kowalewski, T.; McCullough, R. D. *Advanced Materials* **2007**, *19*, 4160–4165.

(50) Osaka, I.; Zhang, R.; Sauvé, G.; Smilgies, D.-M.; Kowalewski, T.; McCullough, R. D. *Journal of the American Chemical Society* **2009**, *131*, 2521–9.

(51) Osaka, I.; Takimiya, K.; McCullough, R. D. *Advanced materials (Deerfield Beach, Fla.)* **2010**, *22*, 4993–7.

(52) Zhan, X.; Tan, Z.; Domercq, B.; An, Z.; Zhang, X.; Barlow, S.; Li, Y.; Zhu, D.; Kippelen, B.; Marder, S. R. *Journal of the American Chemical Society* **2007**, *129*, 7246–7.

(53) Yan, H.; Chen, Z.; Zheng, Y.; Newman, C.; Quinn, J. R.; Dötz, F.; Kastler, M.; Facchetti, A. *Nature* **2009**, *457*, 679–86.

(54) Hwang, Y.-J.; Ren, G.; Murari, N. M.; Jenekhe, S. a. *Macromolecules* **2012**, *45*, 9056–9062.

(55) Meng, Q.; Hu, W. *Physical Chemistry Chemical Physics* **2012**, *14*, 14152–14164.

(56) Bujard, P.; Hall-Goulle, V.; Hao, Z.; Nagasue, H.; De Keyzer, G. Pigmented vitreous material its precursor glass items coated therewith and method of its preparation. WO01/32577 A1, 2001.

(57) Nesvadba, P.; Jandke, J. Oxobenzofuranylide-dihydroindolone. US6503937 B1, 2003.

(58) Wood, J. H.; Cox, L.; Smith, L. I.; Searles, S.; Arnold, R. T. *Organic Syntheses, Collective* **1955**, *3*, 286.

(59) Wood, J.; Jr, C. C. *Journal of the American Chemical Society* **1944**, *66*, 1540–1542.

(60) Zhu, Y.; Champion, R. D.; Jenekhe, S. A. *Macromolecules* **2006**, *39*, 8712–8719.

(61) Bürgi, L.; Turbiez, M.; Pfeiffer, R.; Bienewald, F.; Kirner, H.-J.; Winnewisser, C. *Advanced Materials* **2008**, *20*, 2217–2224.

(62) Usta, H.; Facchetti, A.; Marks, T. *Journal of the American Chemical Society* **2008**, *130*, 8580–8581.

(63) Steckler, T. T.; Zhang, X.; Hwang, J.; Honeyager, R.; Ohira, S.; Zhang, X.-H.; Grant, A.; Ellinger, S.; Odom, S. a; Sweat, D.; Tanner, D. B.; Rinzler, A. G.; Barlow, S.; Brédas, J.-L.; Kippelen, B.; Marder, S. R.; Reynolds, J. R. *Journal of the American Chemical Society* **2009**, *131*, 2824–6.

(64) Jones, B. A.; Facchetti, A.; Wasielewski, M. R.; Marks, T. J. *Journal of the American Chemical Society* **2007**, *129*, 15259–78.

(65) Braun, S.; Salaneck, W. R.; Fahlman, M. *Advanced Materials* **2009**, *21*, 1450–1472.

(66) Chen, Z.; Lee, M. J.; Shahid Ashraf, R.; Gu, Y.; Albert-Seifried, S.; Meedom Nielsen, M.; Schroeder, B.; Anthopoulos, T. D.; Heeney, M.; McCulloch, I.; Sirringhaus, H. *Advanced materials (Deerfield Beach, Fla.)* **2012**, *24*, 647–52.

(67) Zhang, A.; Yu, M.; Lan, T.; Liu, Z.; Mao, Z. *Synthetic Communications* **2010**, *40*, 3125–3134.

(68) Srinivas, B.; Priya, V. R.; Babu, G. S.; Rao, J. V.; Malathy, P. S.; Manohar, K. R.; Prakash, B. C.; Srikanth, L. *Der Pharma Chemica* **2010**, *2*, 378–384.

(69) Zhong, M.; Li, L. INHIBITORS OF HCV NS5A. WO 2011/149856 A1, 2010.

(70) Sun, G. *Advances in Optics and Photonics* **2010**, *3*, 53.

(71) Munguía, J.; Bluet, J.-M.; Marty, O.; Bremond, G.; Mermoux, M.; Rouchon, D. *Applied Physics Letters* **2012**, *100*, 102107.

(72) Subramania, G.; Lee, Y.-J.; Fischer, A. J. *Advanced materials (Deerfield Beach, Fla.)* **2010**, *22*, 4180–5.

(73) Becke, A. *Physical Review A* **1988**, *38*, 3098–3100.

(74) Lee, C.; Yang, W.; Parr, R. G. *Physical Review B* **1988**, *37*, 785–789.

(75) Frisch, Æ.; Hratchian, H. P.; Dennington II, R. D.; Keith, T. A.; Millam, J.; Nielsen, A. B.; Holder, A. J.; Hiscocks, J. *GaussView 5 Reference*; Manual Ver.; Wallingford, CT, 2009.

(76) Frisch, Æ. *Gaussian 09W Reference*; Wallingford, CT, 2009.

(77) Frisch, M. J.; Trucks, G. W.; Schlegel, H. B.; Scuseria, G. E.; Robb, M. A.; Cheeseman, J. R.; Scalmani, G.; Barone, V.; Mennucci, B.; Petersson, G. A.; Nakatsuji, H.; Caricato, M.; Li, X.; Hratchian, H. P.; Izmaylov, A. F.; Bloino, J.; Zheng, G.; Sonnenberg, J. L.; Hada, M.; Ehara, M.; Toyota, K.; Fukuda, R.; Hasegawa, J.; Ishida, M.; Nakajima, T.; Honda, Y.; Kitao, O.; Nakai, H.; Vreven, T.; Montgomery, J. A. J.; Peralta, J. E.; Ogliaro, F.; Bearpark, M.; Heyd, J. J.; Brothers, E.; Kudin, K. N.; Staroverov, V. N.; Keith, T.; Kobayashi, R.; Normand, J.; Raghavachari, K.; Rendell, A.; Burant, J. C.; Iyengar, S. S.; Tomasi, J.; Cossi, M.; Rega, N.; Millam, J. M.; Klene, M.; Knox, J. E.; Cross, J. B.; Bakken, V.; Adamo, C.; Jaramillo, J.; Gomperts, R.; Stratmann, R. E.; Yazyev, O.; Austin, A. J.; Cammi, R.; Pomelli, C.; Ochterski, J. W.; Martin, R. L.; Morokuma, K.; Zakrzewski, V. G.; Voth, G. A.; Salvador, P.; Dannenberg, J. J.; Dapprich, S.; Daniels, A. D.; Farkas, O.; Foresman, J. B.; Ortiz, J. V.; Cioslowski, J.; Fox, D. J. Gaussian, Inc., Wallingford CT, **2010**.

(78) Kumada, M.; Tamao, K. *Advances in Organometallic Chemistry* **1968**, *6*, 19.

(79) Pommerehne, J.; Vestweber, H.; Guss, W.; Mahrt, R. F.; Bassler, H.; Porsch, M.; Daub, J. *Advacned Materials* **1995**, *7*, 551.

(80) Al-Ibrahim, M.; Roth, H. K.; Schroedner, M.; Konkin, A.; Zhokhavets, U.; Gobsch, G.; Scharff, P.; Sensfuss, S. *Organic Electronics* **2005**, *6*, 65.

(81) Nair, G. G.; Prasad, S. K.; Yelamaggad, C. V. *Journal of Applied Physics* **2000**, *87*, 2084.

(82) Tseng, C.-W.; Huang, D.-C.; Tao, Y.-T. *ACS Applied Materials & Interfaces* **2012**, *4*, 5483–5491.

(83) Hook, J. P. Van; Tobolsky, A. V. *Journal of the American Chemical Society* **1958**, *80*, 779–782.

(84) Wu, C.-H. S.; Hammond, G. S.; Wright, J. M. *Journal of the American Chemical Society* **1960**, *82*, 5386–5394.

(85) Lewis, F. M.; Matheson, M. S. *Journal of the American Chemical Society* **1949**, *71*, 747–748.

(86) Malkin, S.; Fischer, E. *The Journal of Physical Chemistry* **1962**, *66*, 2482.

(87) Ramirez, F.; Dershowitz, S. *The Journal of Organic Chemistry* **1957**, *22*, 41–45.

(88) Cooke, M. P. J. *The Journal of Organic Chemistry* **1973**, *38*, 4082–4084.

(89) Guo, X.; Fan, H.; Zhang, M.; Huang, Y.; Tan, S.; Li, Y. *Journal of Applied Polymer Science* **2012**, *124*, 847–854.

(90) Beyer, H.; Kreutzberger, A. *Chemische Berichte* **1952**, *85*, 333–337.

(91) Holt, P.; Smith, A. *Journal of the Chemical Society (Resumed)* **1965**, 5245–5248.

(92) Liu, G.; Pu, S.; Wang, X. *Tetrahedron* **2010**, *66*, 8862–8871.